Design of a Micro Milling Setup with an Active Magnetic Bearing Spindle

Proefschrift

ter verkrijging van de graad van doctor
aan de Technische Universiteit Delft,
op gezag van de Rector Magnificus prof. ir. K.C.A.M. Luyben,
voorzitter van het College voor Promoties,
in het openbaar te verdedigen op dinsdag 28 september 2010 om 12:30 uur
door

Maarten Hartger Kimman

werktuigkundig ingenieur
geboren te Leeuwarden

Dit proefschrift is goedgekeurd door de promotor:
Prof. ir. R.H. Munnig Schmidt

Copromotor: dr. ir. H.H. Langen

Samenstelling promotiecommissie:

Rector Magnificus, voorzitter
Prof. ir. R.H. Munnig Schmidt, Technische Universiteit Delft, promotor
Dr. ir. H.H. Langen, Technische Universiteit Delft, copromotor
Prof. dr. ir. H. Bleuler, Ecole Polytechnique Fédérale de Lausanne
Prof. dr. ir. G. Schitter, Technische Universität Wien
Prof. dr. ir. H. van Brussel, Katholieke Universiteit Leuven
Prof. dr. ir. M. Steinbuch, Technische Universiteit Eindhoven
Prof. dr. ir. D. Rixen, Technische Universiteit Delft

Reservelid:
Prof. dr. ir. J. van Eijk, Technische Universiteit Delft

This research was supported by MicroNed.

ISBN: 978-90-9025665-8

Printed in the Netherlands.

Contents

Chapter 1

Introduction

This thesis describes the design and realization of a machining center for manufacturing miniature components. There is a continuous demand for miniaturizing products in a broad spectrum of applications [1, 2]. Medical devices for example, greatly benefit from reduced dimensions. Another main driving force behind miniaturization is the demand for reduced masses. For instance, the mass of the Bosch ABS (anti-lock braking) system has been reduced from 6.2 kg in 1989 to 1.8 kg in 2001 [1]. When the part dimensions decrease, the demand for improved dimensional accuracy and surface quality increases. Figure 1.1 shows two examples of miniaturized components.

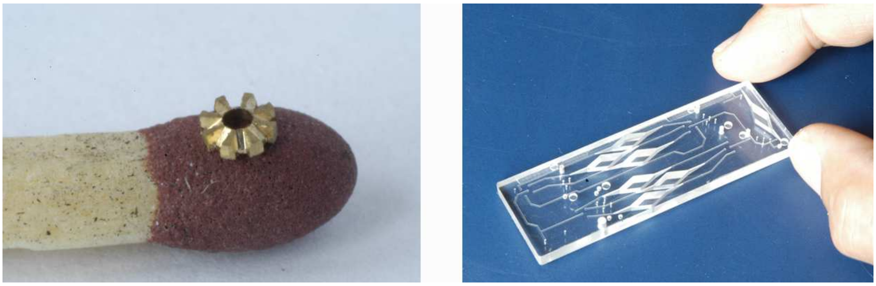

Figure 1.1: Examples of miniaturized components, manufactured at TNO science and industry. A miniaturized gear (left) and a lab on a chip (right). Photos courtesy of Philip Broos / Leiden, MicroMegazine

The left picture in Figure 1.1 shows a miniature gear wheel manufactured by micro milling. The right picture in Figure 1.1 shows an example of a Lab on a Chip (LOC). A lab on a chip combines several laboratory functions on a single chip. Miniaturizing laboratory functions reduces the use of reagents, power, and space. Currently, a LOC is typically manufactured using lithographic processes. Micro milling potentially enables fabricating LOCs from a broader range of materials, with reduced costs due to less machining time, a smaller footprint, and the absence of clean room processing.

The mould and die industry has a great interest in machining moulds for manufacturing small components by injection moulding. The moulds are typically manufactured from hardened steel and therefore need to be machined using conventional processes such as milling or electronic discharge machining. Micro milling enables the machining of moulds and dies from hardened tool steel with more and finer details.

1.1 Background

Lithography is the leading technology for manufacturing micro components like LOCs and other micro system technologies. Lithographic processes require using expensive masks and, thus, are best suited for the production of large batches. Micro machining using lithographic processes is limited to machining silicon-like materials in 2.5 dimensions. A 2.5D, or areal process, means the build up of successive two dimensional layers into the third dimension.

To structure metallic materials in three equally independent dimensions, technologies such as micro milling, Micro Electrical Discharge Machining (μEDM), Micro Electro Chemical Machining (μECM), and micro grinding are used. Micro milling is the mechanical removal of material using a sub-millimeter diameter cutting tool. With μEDM, material is removed by the discharge occurring between a tool electrode and a workpiece emerged in a dielectric. μECM is the controlled electrochemical dissolution of workpiece material in an electrolyte by applying short voltage pulses.

With ultra precision macro machining, shape accuracy levels better than 0.1 μm can currently be achieved [1]. However, for downscaling these macro machining processes to the micro scale properly, machine and process must be improved regarding material removing rate, machining speed, surface quality, feature size, and accuracy.

Concluding, there is a gap to be bridged between the manufacturing of micro systems with lithographic processes in silicon-like materials, and the ultra high precision macro machining with very high accuracy in metallic materials.

1.2 Micro Milling

Milling is the mechanical removal of material using a rotating cutting tool. A top view of this milling mechanism is shown in figure 1.2. As the cutting edge passes through the workpiece, material is removed.

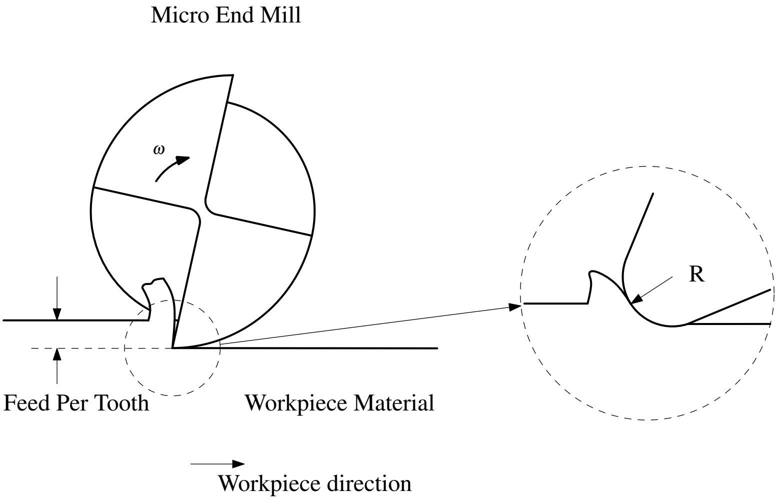

Figure 1.2: Top view of the end milling mechanism (left) and the minimum chip thickness effect as a result of scaling down the milling tool (right).

Micro milling can be defined as milling with tool diameters below 1 mm. Commercially available micro milling tools currently have diameters down to 0.05 mm. Figure 1.3 illustrates two micro milling tools, with diameters of 0.2 mm and 1 mm. A scanning electron microscope image of a 0.3 mm end mill is also shown.

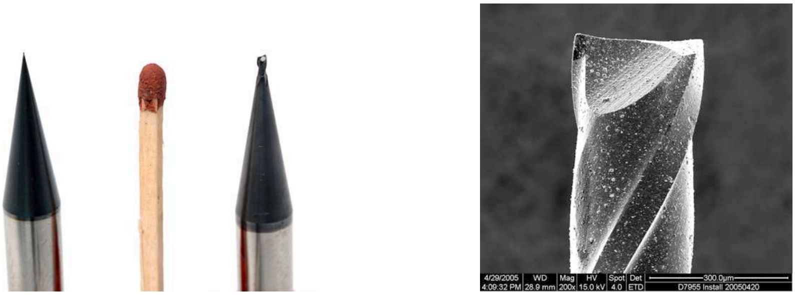

Figure 1.3: Micro milling tools; The figure on the left shows a 0.2 mm micro end mill and a 1 mm end mill, the SEM picture on the right shows the cutting edges of a 0.3 mm end mill.

The cutting conditions for micro milling are generally obtained by scaling down the process parameters used in the macro domain, which is a well understood process. However, this approach does not result in a satisfactory cutting quality during micro milling [3].

The minimum chip thickness effect is illustrated on the right in figure 1.2, and is an example of the difference between macro and micro cutting. A cutting edge which is considered sharp in the macro domain, has a large cutting edge radius when observed in the micro domain. A minimum chip load is therefore required due to the micro cutting tool geometry [4]. Thus, micro milling is actually performed with relatively blunt tools.

Micro cutting tools suffer from relatively large geometrical runout, typically 5 μm for a 100 μm tool [5]. This runout is of the same order of magnitude as the Feed Per Tooth (FPT), resulting in large fluctuating loads on the cutting tool. In addition to this dynamic effect, micro cutting tools are subjected to large tool bending deflections due to their small diameter.

For these reasons, a novel approach is needed to improve the quality of the micro machining process. This quality is defined by the geometrical accuracy, and the quality of the cut. Such an approach would include the downscaling of machinery, process combination, on machine toolmaking, vibration assisted machining, and improved process monitoring. These improvements to the micro milling quality will be discussed later in this chapter.

Micro milling requires a rotational speed far above the maximum rotational speed of conventional milling spindles [6, 2]. This speed is required to have sufficient cutting speed at the tool edge, which partly defines the quality of the cut [4, 7]. When reducing the diameter of the cutting tool, the rotational speed must also be increased to maintain productivity [3]. Commercially available micro milling tools have diameters down to 0.1 mm. Theoretically this requires a spindle rotational speed of 500.000 rpm, in order to achieve a typical macro milling cutting speed of 200 $m{\cdot}min^{-1}$. In conventional macro milling spindles, a very high rotational is difficult to achieve due to high rotor masses, large rotor diameters and the use of mechanical bearings.

The minimum chip thickness effect, in combination with the high rotational speed, requires high feed rates. Conventional spindle driven stages are not able to achieve the accelerations and speeds for micro milling. Therefore, a directly driven, fast workpiece positioning system is required.

This thesis describes the mechatronic design and realization of a micro milling setup, comprising a high speed spindle and a fast workpiece positioning system. This thesis focuses on designing a spindle capable of reaching the required high rotational speeds and tool tip positioning accuracy using Active Magnetic Bearing (AMB) technology.

1.3 Micromachining Technology

Two trends are visible in micro machining; micro machining with conventional ultra precision machines and micro machining with small ”micro factories”. Micro factories are micro machining stations on a small footprint and will be further discussed in Section 1.3.2.

A typical macro scale design philosophy is to construct a heavy and stiff machine, where the accuracy is determined by the manufacturing precision of the individual parts of the machine. When such a machine is used in a micro milling application, several problems may arise. First, the tool stiffness of a micro mill is very low due to its small diameter. The stiffness of a micro tool is on the order of 10 $kN{\cdot}m^{-1}$, which deteriorates the high stiffness design approach of the rest of the machine. Tool bending reduces the accuracy of the milled part [8].

In this section different aspects of micro machining tools are described. For each aspect, the contribution of this research to the state of the art is discussed.

1.3.1 Downscaling

When downscaling machinery, some parameters scale beneficially with decreasing size while others scale unfavorably [9]. Thermal deformations, for example, decrease with decreasing machine tool size [10]. Flexural resonance frequencies increase as the machinery is reduced in size. The vibration amplitudes are lowered with decreasing size due to the difference in scaling between inertial forces and elasticity [10, 11].

In this research, the lowest spindle resonance frequency should be placed considerably higher than the cutting frequency which is one or two times the rotational speed. By not exciting the spindle resonances with the cutting frequencies, the cutting process quality is increased. The higher flexural resonance frequencies, and the lower moving masses enable higher control bandwidths, resulting in an increased virtual stiffness.

With the lower masses however, the sensitivity to disturbances from the process increases. As mentioned, these disturbances have a frequency component of one or two times the rotational frequency, this is well above the closed loop bandwidth of the system. The trade off between a higher control bandwidth and the increased sensitivity to the high frequent disturbances will be investigated. By reducing the size of the spindle, the bandwidth of the cutting force estimation can be increased [12].

The low moving mass will enable fast open loop interventions. Such an intervention could be the retraction of the tool in case of a short-circuit during μEDM, or in case of a sudden increase in cutting force during micro milling. A cutting force increase can potentially lead to tool breakage. By using Active Magnetic Bearings, the spindle is actively controlled in 5 DOF. In this research project we investigate the use of the axial magnetic bearing to swiftly retract a machining tool out of the workpiece.

Machine downscaling is furthermore required to reach a very high rotational speed, as this is limited by the combination of rotor outer diameter and the tensile strength of its material.

1.3.2 Micro Factory

The concept of a micro factory was first introduced in 1990 by the Mechanical Engineering Laboratories (MEL) in Japan [13]. Their motivation to realize a desktop micro factory was based on the fact that conventional machining tools were inappropriate for producing miniature components. By reducing the machinery size, space and energy can be saved. The main challenge in micro machining using small machinery is to achieve high accuracy and high surface qualities, mainly raised by the reduced stiffness and mass of smaller machines.

Several micro factories are described in literature. Often, the miniaturized machine tools are referred to as Meso-scale Machine Tools (MMT). The design of miniature machine tools used in a micro factory are described by Kussul et al. [10]. Kussul stated that machinery must be downsized accordingly to produce miniaturized parts. The described design approach is the downsizing of conventional machinery. In the research of Kussul, typical accuracies of 20 μm are achieved. In this thesis, the target part accuracy is sub micrometer.

Axinte et al. [14] describe the design and analysis of a 4 axis machine tool. The machine tool is equipped with a commercially available 200.000 rpm. air turbine spindle for micro grinding or a commercially available 50.000 rpm. brushless dc spindle with ceramic bearings.

Okazaki et al. [15] describe the machining of thin ribs using a desktop NC milling machine. The spindle consists of a miniature, 200.000 rpm. AC motor.

Honegger et al. [6, 16] describe the development of an automated micro factory. Their micro factory consists of two machine tools, a metrology station, and part handling. They aim at sub micron accuracy. In stead of the standard electrical drive, this machine tool is equipped with an air bearing spindle that is turbine driven, capable of speeds up to 160.000 rpm.

Other micro factories, specifically focused on the miniaturization of machinery have been reported by Verettas et al. [17], Vogler et al. [9], and Okazaki et al. [18].

Takeuchi et al. [19] describe the design of an ultra precision milling machine using only contactless servo systems. This research is focused on achieving a high accuracy instead of downsizing the machinery. The spindle as well as the linear guides and the rotational axis are aerostatically supported. The development of a commercially available 5-Axis high precision machine is described by Sriyotha et al. [20].

The work in this thesis is part of a larger research project where we envision a desktop-sized micro factory. The micro factory features a workpiece positioning stage, a miniature spindle (this work), a haptic assembly line, and a workpiece inspection platform. In this thesis, this larger project will be referred to as the μfac project.

1.3.3 Process Combination

Each of the processes mentioned in Section 1.1 has its inherent limitations [2]. For example, runout is unavoidable in micro milling due to tool geometry and high rotational speeds, and the material removal rates in μEDM and μECM are very low. By combining the different processes, we can benefit from their individual qualities. The positioning accuracy in μEDM and μECM is high due to the absence of process forces and low rotational speeds [21]. The surface finish is generally higher in micro milling. The surface roughness of μEDM can be improved by μECM.

Fleischer et al. [22] describe the potential of combining micro milling, μEDM and micro laser ablation for the manufacturing of micro molds.

In the μ*fac* project, we consider three types of micro machining, namely, micro milling, μEDM and μECM. A general process flow for manufacturing a small component is as follows. A relatively coarse first machining step with a high material removal rate using micro milling is performed. Then, a highly accurate μEDM step is performed and finished by μECM to improve the surface quality.

With the combination of these processes, high accuracy parts can be made with a reasonable throughput. In the μ*fac* project, the merits of using the same spindle for micro milling, μEDM, and μECM are investigated. By performing the machining steps on a single machining station, no accuracy will be lost by re-mounting the workpiece. A miniature spindle is thus required for micro milling, as well as for μEDM and μECM.

1.3.4 On Machine Toolmaking

The accuracy can be further increased when making EDM tools on the machine. Asad et al. [23] describe the fabrication of EDM tools on the machine. When the EDM tool is manufactured on the machine, no accuracy is lost in re-clamping the EDM tool. The machine described in this research is commercially available from MikroTools. The MikroTools-DT110 [24] is a three axis machining center which combines multiple machining processes, such as milling and EDM on a single station. The milling spindle has a maximum rotational speed of 140.000 rpm.

Kurita et al. [25] describe the development of a machine tool which combines micro milling, μEDM, and μECM. An electrode is machined by micro milling. Subsequently, this electrode is used for μEDM, and the surface finish is improved using μECM.

In the *μfac* project we aim at performing a first machining process with micro milling. Subsequently we will machine the rotating milling tool down to a μEDM tool by WEDG (Wire Electro Discharge Grinding). A final machining step will be performed with the machined μEDM tool in the same spindle. By machining the electrode on the rotating spindle, runout is eliminated.

1.3.5 Vibration Assisted Machining

Moriwaki [26] showed that introducing an elliptical vibration (167 Hz) into the micro milling process improves the machining precision. In the EDM and ECM processes, using an additional vibration of the machining spindle improves the flow of dielectricum and the machining conditions.

This research focuses on developing an Active Magnetic Bearings Spindle. The active nature of the bearings, and the relatively large gap between the bearings and the spindle allow for the desired vibrations to be introduced into the machining processes.

1.3.6 Process Monitoring

In the *μfac* project, we investigate whether more control of the cutting process will improve the quality of micro machined parts. When the milling process is properly monitored, the cutting conditions can be changed to improve the cut quality or to avoid tool breakage. When a macro milling spindle is used for micro milling, tool breakage is often not observed by the operator. Tool breakage can be detected when the cutting forces are observed. When an increase in cutting forces can be detected, tool breakage can even be avoided by changing the feed rate or by fast retraction of the tool.

Typical techniques for monitoring the cutting conditions in the macro milling domain are acoustical measurements and force measurements. Current state of the art force sensors have a maximum bandwidth of 1 kHz and thus, do not have the bandwidth to monitor the cutting forces in the micro milling process at the desired rotational speed [3], due to the low amplitude [2], and high frequency of the cutting forces. In industry, there is a strong need for process monitoring technologies that are more integrated in the machine tool structure [27].

In the μ*fac* project, we aim to develop a new method for monitoring the forces during micro milling by using information from the spindle bearing signals. By using active bearings in the milling spindle, information is available on the position of the rotor and the forces in the bearings. Research on the estimation from the cutting forces using the position and current information from the bearings is carried out by Blom [28].

1.3.7 State of the Art Micro Machine Tools

Micro milling is often performed using commercially available precision machine tools. In order to achieve the high rotational speeds required for micro milling, rather conventional ultra precision machines are equipped with high speed spindles. These high speed spindles are commercially available with spindle speeds ranging from 40.000 up to 200.000 rpm.

Examples of these micro machining stations are: the Makino HYPER2J [29], the Kern Micro [30], the KUGLER Microgantry nano3/5X [31], the Atometric G4-Ultra [32], the Microlution 363-S [33], and the Brunel µltra Mill [34].

One common thing between all thee machining centers is they are equipped with passive spindle bearings, rather than active spindle bearings.

1.4 Problem Statement

This thesis focuses on addressing these issues by designing and realizing an actively controlled magnetic bearing spindle. Briefly summarizing; AMBs allow for high rotational speeds and high accuracy. At low angular speeds, an arbitrary rotational axis can be chosen together with additional motion patterns for vibration assisted machining. Finally, AMB signals can be used for process monitoring and control. In an Active Magnetic Bearing, a control loop determines the position of the rotor in the bearing. The position of the rotor is measured using a contact less displacement sensor, and an electromagnetic actuator is used to position the rotor.

This leads to the problem statement for this thesis:

> Design, build, and investigate Active Magnetic Bearings applied in a high speed micro milling center

Several related issues are addressed in this thesis to answer this research question.

- The design and realization of a miniature milling spindle with active magnetic bearings.
  In order to investigate the use of AMBs in a miniature milling center, a prototype miniature AMB spindle has been designed and realized. The miniature AMB spindle is a typical mechatronic system. The design and realization of a mechatronic system is an iterative process which starts with an assessment of the system requirements. Subsequently, the disturbances acting on the system are identified, followed by the mechanical design of the plant, and the design of the controller. Modeling of both is required to investigate whether the requirements are met or whether the design needs to be changed. Finally, the performance of the system is experimentally investigated.

- The investigation into high speed rotation.
  A main demand on a micro milling spindle is a very high rotational speed. A study in high speed rotation with AMBs will be required for the realization of the milling spindle. A rotor dynamic analysis is performed to investigate the influence of the gyroscopic effects on the accuracy and stability of the fast rotating spindle. In the design of the electromagnetic actuators, the issues regarding rotating losses are addressed. The challenge of increasing the rotational speed as well as the flexible spindle resonance frequencies while maintaining a stable rotating AMB system has been addressed.

- The realization of a three axis miniature machining center.
  In order to investigate the performance of the miniature AMB spindle, it is integrated into a 3 axis miniature machining center. A mechatronic design approach is followed for the realization of a downsized machining center for micro milling, integrating the miniature milling spindle. A preliminary machining test has been performed, showing the use of the miniature AMB spindle during micro milling. Several issues have been addressed in order to perform milling with the designed spindle, such as the design of a high speed tool holder.

This thesis will also provide design guidelines for hybrid reluctance actuators, in an application where high accuracy and high speed are required.

1.5 Thesis Outline

In the next chapter, the basics of Active Magnetic Bearing technology will be described. This chapter will describe the analytical derivation of the forces in a simple AMB and the state of the art in AMB spindle technology, focusing on spindles for milling, spindles with high rotational speed, and spindles for accurate rotation.

Chapter 3 covers the design of a miniature AMB spindle prototype. The design of the rotor and bearings is described, as well as the controller design. The realization of the spindle is described as well as the experimental results. The validity of the models used for the actuator design, as well as the rotor dynamic modelling are experimentally verified.

When the speed of milling spindles is increased, the mounting of the tool holder poses a challenge due to the high centrifugal stresses causing release of the tool. In Chapter 4 a solution to this problem is presented by the design and realization of a novel tool holder system.

The applicability of the miniature AMB spindle prototype has been investigated by integrating it into a milling system. Chapter 5 describes the realization of a three axis, vertical micro milling center, featuring the miniature AMB spindle prototype, an xy-positioning stage, and a z-stage. In this chapter, a preliminary milling experiment is discussed.

The design and realization of the prototype presented in Chapter 3, as well as a literature survey shows the importance of avoiding flexible spindle resonances in micro milling. The flexible resonance frequencies can be increased by reducing rotor length. In Chapter 6, the consequence of reducing length on the rotor dynamic behavior is investigated. Chapter 6 presents a novel AMB spindle design to support a very short rotor, comprising the recommendations from the first miniature AMB spindle prototype described in Chapter 3.

The position measurement of a fast rotating shaft is challenging. Chapter 7 describes the investigation into different position measurement technologies in AMB systems, with the goal to find a suitable position sensor for the short spindle design presented in Chapter 6.

In Chapter 8, the work presented in this thesis is discussed as well as the recommendations that can be done based on this thesis work.

Chapter 2

Magnetic Bearing Spindles

In this thesis we investigate the application of active magnetic bearings in a miniature milling center as a part of the μ*fac* project described in Chapter 1. In this chapter, the working principle of an AMB system is described. The use of AMBs in rotating systems and in precision systems is described. In Section 2.1, the key components of a typical AMB system are described. The classical configuration of an AMB in a rotating application is described as well as several alternative configurations. The analytical derivation of the force in an electromagnetic actuator is given in Section 2.2. In Section 2.4 an overview of state of the art AMBs is given.

2.1 Magnetic Bearings

Active Magnetic Bearings have often been applied in rotating machinery such as turbo molecular pumps, flywheels, and milling and grinding spindles. They are mainly applied because of their lack of mechanical contact. This frictionless operation reduces wear in the bearings, maintenance, and energy consumption. With AMBs very high positioning accuracies can potentially be achieved [35]. More recently, AMBs have found their way in linear applications in high precision machinery [36]. The μ*fac* project research objectives include the use of active magnetic bearings to have more control on the milling process, to achieve high positioning accuracy, and to be able to have more freedom over the position of the shaft in the bearings.

This section describes the fundamentals of Active Magnetic Bearings technology. Figure 2.1 illustrates the basic operating principle of an Active Magnetic Bearing, and its key components. An electromagnetic actuator acting on a ferromagnetic body has a negative stiffness, and is therefore an unstable system. In a system with negative stiffness, the force increases in the direction of the displacement. There-

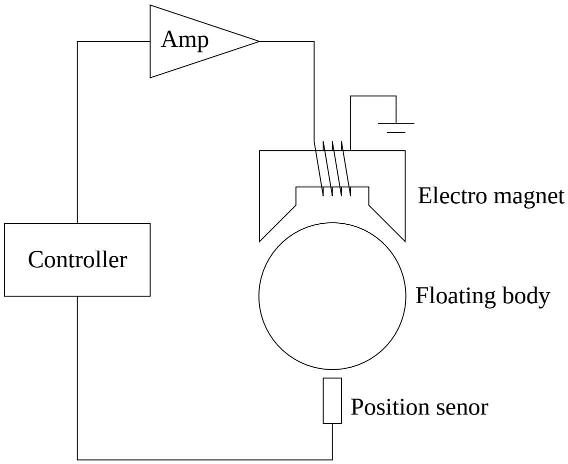

Figure 2.1: Fundamental Active Magnetic Bearing and its basic components, floating body, position sensor, controller, amplifier, and electro magnet.

fore, a control loop is required to stabilize the system and position the body. A typical AMB system therefore typically consists of a contactless sensor which measures the position of a floating body, a position controller, and an amplifier driving the current to the electromagnet acting on the floating body. In our case, the floating body is the high speed rotor. The integration of these technologies into one system make AMBs typical mechatronic systems.

2.2 Reluctance Type Actuator

Commonly, reluctance type actuators are used in AMB systems. Reluctance type actuators can achieve relatively high force densities, compared to for example Lorentz force actuators. In this section, the force between the electromagnet and a ferromagnetic target is derived. Figure 2.2 illustrates the actuator and the actuated body. In our application, the actuated body is the spindle with micro cutting tool, which is levitated by ten reluctance actuators and controller in five Degrees Of Freedom (DOF).

To analytically derive the force in a reluctance type actuator, several assumptions need to be made. These assumptions, and their consequences on the calculated force are described below.

- There is no leakage flux, so called stray field. When leakage flux is present, the flux density in the airgap is lower than expected, resulting in a lower actuator force.

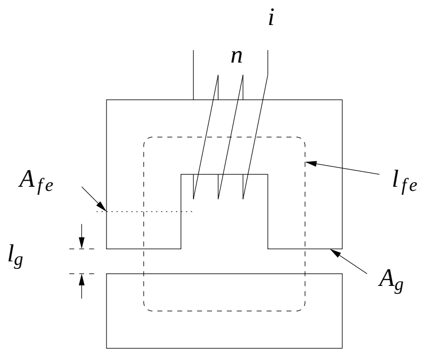

Figure 2.2: Reluctance type actuator

- The field in the airgaps is homogeneous and does not blossom out at the pole edges. When the field is not entirely concentrated in the airgap, this results in a lower actuator force.
- The permeability of iron is infinitely large. The permeability of air and magnet material is several orders of magnitude smaller than the permeability of iron. The permeability of iron does however contribute to the total reluctance of the circuit, resulting in a lower flux density in the airgap than analytically predicted.
- There is no hysteresis. Hysteresis is present in the iron of a reluctance type actuator, thus the force depends on the force history in the actuator.
- there is no saturation, which is only valid when the flux densities are low. When saturation does occur, the force is non-linear with respect to the applied current, and will eventually saturate.

The force in a magnetic actuator can be derived from the magnetic energy stored in the airgap. By taking the partial derivative of this energy with respect to the airgap length, the magnetic actuating force can be derived.

The field energy (W) in the airgap is given by equation 2.1,

$$W = \frac{1}{2} B_g H_g A_g 2 l_g, \tag{2.1}$$

where B_g is the flux density in the airgap, H_g is the magnetic field intensity, A_g is the pole shoe surface and l_g is the length of the airgap (see Figure 2.2). For the determination of the magnetic field energy in the airgap, the magnetic flux density (B) in the airgap is determined. The flux density in the airgap is determined using the second and the fourth Maxwell's equations. The two equations are given in Equation 2.2, the second Maxwell equation states that the flux in the magnetic circuit is conserved. The simplified, fourth Maxwell equation is also called Ampère's circuital law where we integrate the magnetic field strength H, over the flux path:

$$\oint BdA = 0 \qquad \text{and} \qquad \oint Hds = ni, \tag{2.2}$$

where B is the magnetic flux density and A is the cross section area, H is the magnetic field intensity and ni is the total current, windings n and current i. In this derivation we assume that the surface area in the actuator and the airgap is constant.

The resulting force from the derivative, $\partial W(\partial l_g)^{-1}$, in one reluctance type actuator is given by:

$$f = \frac{1}{4}\mu_0 n^2 A_g \frac{i^2}{l_g^2}, \tag{2.3}$$

where μ_0 is the relative permeability of air. From Equation 2.3 we can conclude that the force from one magnetic actuator is highly non linear and depends on the square of the coil current, i. The force in the actuator is inversely dependent on the gap length, l_g squared.

2.2.1 Differential Driving Mode

The actuator described in the previous section can only provide an attractive force, therefore a second actuator is needed to provide a force in the opposite direction. This actuation method is referred to as the differential driving mode [37]. The differential driving mode actuation in a rotating bearing application in two directions is illustrated in Figure 2.3. This configuration of the AMBs is relatively easy to manufacture, due to its constant cross section and the absence of permanent magnets.

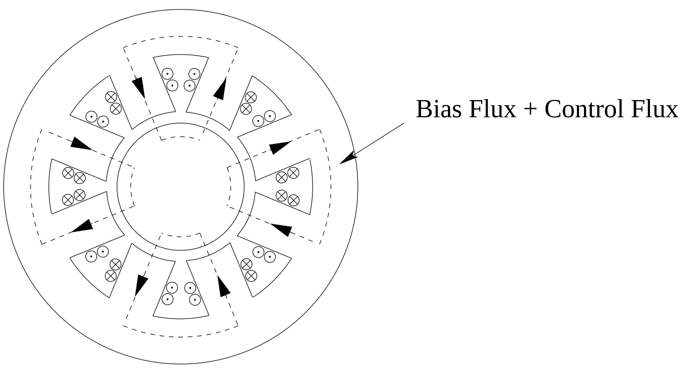

Figure 2.3: Typical application of reluctance type actuators, configured in differential driving mode for two degrees of freedom, in a rotating AMB system.

The force from the actuator on the body is highly non linear dependent on the current and the gap, as shown in Section 2.2. Due to the quadratic nature of the force current dependency, the force slew rate of the actuator is very low when no current is applied to the coil. The force-slew rate is described by Molenaar [38], and is the rate at which the force in an AMB can be applied. The force slew rate furthermore depends on the amplifier voltage.

When a bias field is applied to both the actuators, the force slew rate, and thus the dynamic performance of the bearing is improved. The bias field linearizes the force position and force current dependency in the actuator. In the example shown in Figure 2.3 the bias field is generated with a bias current.

The derivation of the force in the actuators in differential driving mode with a bias current is shown in Equation 2.4, showing the increased linearity of the actuator.

$$f = \frac{1}{4}\mu_0 n^2 A_g \frac{(i_o + i_x)^2}{(l_g - x)^2} - \frac{1}{4}\mu_0 n^2 A_g \frac{(i_o - i_x)^2}{(l_g + x)^2}, \tag{2.4}$$

We can see that several higher order terms vanish from this equation, making the force current, and the force position dependency of the actuator more linear. When we linearize the remaining part of the equation in the operating point (i_x=0 and x = 0) with respect to the position and the current we get the expression for the force in the reluctance actuator:

$$f = k_x x + k_i i, \tag{2.5}$$

where k_x is is the force position dependency of the bearing, also called the negative stiffness, and where k_i is the force current dependency of the AMB. When we derive k_x and k_i, they are given by:

$$k_x = \frac{\mu_0 n^2 A_g i_0^2}{l_g^3} \qquad k_i = \frac{\mu_0 n^2 A_g i_0}{l_g^2}. \tag{2.6}$$

2.3 AMB Configurations

The bias field of the actuator described in Section 2.2.1 is generated by applying a bias current to the bearing coils. The bias field can also be created using permanent magnets. The use of permanent magnets reduces the power consumption, and thus the heat generation in the bearings. Permanent magnets can be integrated in a series configuration and a parallel configuration. In the series configuration, the permanent magnet is in the path of the control flux lines, reducing the efficiency of the actuator. The coil has to drive the flux through the permanent magnet which has a low permeability. In the parallel configuration, the control flux lines have a different path than the bias flux lines. This type of hybrid bearings is referred to as non-coplanar AMBs.

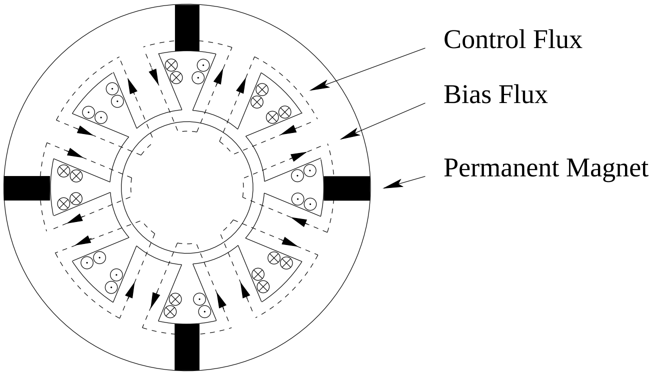

Figure 2.4: Heteropolar AMB system to support a rotating shaft where the bias flux is provided by permanent magnets.

Figure 2.4 illustrates the integration of permanent magnets to provide the bias flux. This is an example of a parallel configuration of bias flux and control flux, where the bias flux is generated by permanent magnets. A drawback of this configuration is the difficult manufacturability, and the integration of the permanent magnets is expensive due to the difficulty to achieve strict tolerances by sintering.

The AMBs illustrated in Figures 2.4 and 2.3 are both heteropolar AMBs. In heteropolar AMBs the bias flux lines run perpendicular to the rotor axis.

2.3.1 Homopolar AMBs

In our application, where we aim at extremely high rotational speed, it is important to consider the losses in the magnetic actuators. The main losses in AMB systems can be divided into three types, and are described below.

- Ohmic losses
  Ohmic losses are losses in the bearing windings due to the resistance of these windings. These losses can be reduced by the use of permanent magnets, and thus reducing the required current.

- Hysteresis losses
  Hysteresis losses occur when the rotor or stator material has to be remagnetized. The magnetization of a ferromagnetic target is described by the BH curve. A typical BH curve is illustrated in Figure 2.5. The surface under the BH curve of the material is proportional to the dissipated energy, since the

product BH is equal to the energy density. The rotating rotor is magnetized as it passes an AMB stator. When the rotor is magnetized, and then remagnetized, the small loop in Figure 2.5 is traveled. The exact location of this small loop depends on the bias and the history. As the hysteresis loop is traveled, the enclosed surface in the loop is a measure of the energy loss.

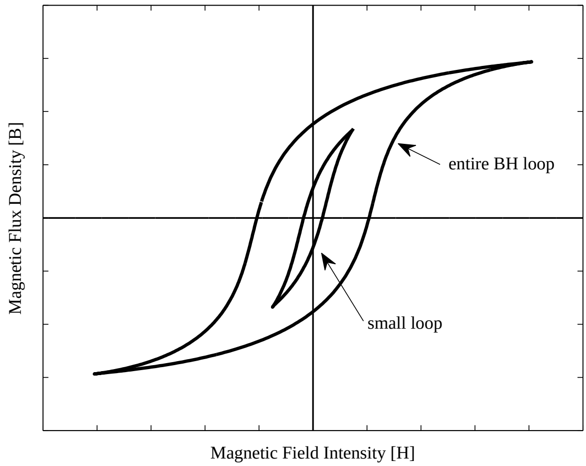

Figure 2.5: BH curve, showing the entire hysteresis loop, as wel as a small loop which could be followed when remagnetizing a rotor with the bias flux.

In a heteropolar AMB, as illustrated in Figure 2.3, this small loop will be traveled four times during each revolution. At very high rotational speed, this results in large rotating losses. These losses can partly be avoided by choosing a suitable magnetic bearing configuration.

- Eddy current losses
  Eddy current losses are ohmic losses occurring in the rotor or stator each time an current is induced due to a changing magnetic field. These losses can occur by a change in flux density when the AMB is actuated, in this case the eddy currents introduce a phase lag into the actuator, reducing the achievable bandwidth. Eddy currents can also occur when the bias flux density in the rotor is changed due to the rotation of the rotor. In this case the ohmic losses in the rotor cause it to heat up. Furthermore, the eddy currents drag the rotation of the rotor. Eddy currents are generally reduced by the use of laminations in the stator and rotor material or by the use of oxidized or compound materials.

As explained, the heteropolar bearing configuration causes the rotor to be remagnetized several times in each revolution. The remagnetization results in hysteresis losses and eddy current losses in the rotor. In our application, where we aim at very high rotational speeds, it is important to avoid changing fields in the rotor.

This can be achieved by using a configuration where the bias flux lines run parallel to the rotor axis. This type of bearings is referred to as homopolar AMBs. A particular kind of homopolar bearing configuration, where the bias field is created with permanent magnets in a parallel flux configuration, is illustrated in Figure 2.6. This type of bearings has been described by Lee et al. [39]. This bearing is also a 2 DOF actuator. A disadvantage of this actuator is that it consists of two layers, which requires more rotor length. By increasing the bearing length, and thus the shaft length, the resonances of the shaft are shifted to lower frequencies.

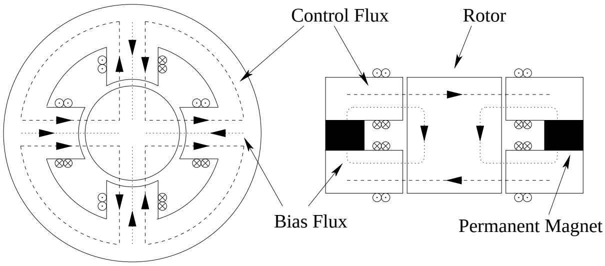

Figure 2.6: Permanent magnet biased, homopolar, reluctance type actuator.

2.4 State of the art Active Magnetic Bearing Spindles

Active magnetic bearings are applied in many rotating applications. In this section some of those AMB systems are described. Especially the spindles designed for milling, for high rotational speeds, and for high accuracies will be taken as examples.

The first AMB spindle for application in milling was built by the company S2M in cooperation with Arnold [40] in 1985. S2M, currently part of the SKF group, is still one of the worlds largest suppliers of magnetic bearings. One of their products is a 30.000 rpm 70 KW aluminum macro milling spindle. Auchet describes the use of bearing signals for cutting force estimation using an S2M spindle in [41]. Siegwart presented a digitally controlled AMB milling spindle in 1989 [40]. This spindle has a maximum rotational speed of 40.000 rpm and a cutting power of 35 kW.

As mentioned in Chapter 1, the monitoring and control of the cutting process using the information from the bearing signals is investigated within the μ*fac* project. The preliminary research on this topic has been carried out on a commercially available AMB spindle from EAAT [42]. This spindle is equipped with analog decentralized PID controllers. In a decentralized controller, the gap between the bearing and the rotor in the bearing is locally controlled in each actuator. This spindle has a maximum theoretical operating speed of 120.000 rpm. In practice, the speed is limited to 80.000 rpm by the flexible resonances of the spindle including the cutting tool. Cutting operations at high rotating speeds are heavily influenced by the relatively low flexural resonances of the spindle, having a deteriorating effect on the quality of the cut and on the estimation of the cutting process. The mass of the spindle in this application is 1.2 Kg. This spindle is provided with homopolar AMBs with a linearizing bias current.

A spindle for high rotational speeds has been developed by Larsonneur et.al. [43] in 1990. The work from Larsonneur describes the mechanical limitations in the design of a rotor for high speed rotation. The spindle described is equipped with digital decentralized controllers, the passing of the first two flexural critical speeds is described. The spindle has a maximum theoretical speed of 100.000 rpm, however the rotational speed is in practice limited to 64.000 rpm due to a combination of amplifier saturation and unbalance.

The design of a spindle for 120.000 rpm. has been described by Betschon [44]. Betschon presents the principles for the design of active magnetic bearings. The design of a homopolar radial bearing, as well as a homopolar combined radial-axial bearing system with permanent magnets for bias is described. The combined radial-axial bearings enables reduction of the rotor length. In his research a maximum rotational speed of 90.000 rpm has been realized.

An example of the application of Active Magnetic Bearings for high accuracy applications is given by Jabben [35]. Jabben describes the design of a magnetically levitated platform for optical disk mastering.

2.5 Conclusions

In this chapter, the basics of Active Magnetic Bearing technology have been presented. Furthermore, the application of AMBs in rotating systems in different configurations has been shown. Current technology in rotating active magnetic bearings, with regard to high speed rotation, high speed milling and high accuracy has been treated. In the next chapter, the design of a miniature active magnetic bearing spindle for micro milling is presented.

Chapter 3

A Miniature AMB Milling Spindle

This chapter describes the design and realization of a miniature milling spindle with Active Magnetic Bearings (AMBs). Permanent magnet biased, reluctance type actuators position the rotor in five Degrees Of Freedom (DOF), leaving the rotation unconstrained. A rotordynamic model has been developed for the design of the controller, and enabled simulation of the spindle's performance under the influence of cutting forces. A Center of Gravity (COG) decoupled controller, including a negative stiffness compensation scheme, has been implemented. The spindle designed with these controllers has been tested successfully at rotational speeds up to 150.000 rpm.

3.1 Introduction

As described in Chapter 1, micro milling requires rotational speeds far above the maximum attained by conventional milling spindles, in order to have sufficient cutting speed at the tool edge and to be efficient [3, 4, 7]. In such systems, the rotational speed is limited by high rotor masses, large rotor diameters and the use of mechanical bearings.

The aim of this research is to improve these aspects by designing a spindle with Active Magnetic Bearings (AMBs) specifically aimed at micro milling applications. A rotor suspended by AMBs can achieve very high rotational speeds, due to the absence of mechanical contact. Furthermore, AMBs can be used to achieve a very high positioning accuracy. With AMBs an arbitrary rotational axis of rotation can be chosen, or vibrations to improve micromachining process conditions can be introduced using the magnetic actuators. Another distinguishing advantage compared to passive bearings, is that by using AMBs in the milling spindle, information is available on the position of the rotor and the forces in the bearings. Research on the estimation from the cutting forces using the position and current information from the bearings is carried out by Blom [28] as a part of the μ*fac* project.

In this chapter, first the spindle specifications and the disturbances on the system are identified. Secondly, the design the spindle is presented. In Section 3.5, modelling of the spindle supported by AMBs is presented to see whether the design meets the specifications and to enable the design of stabilizing controller for the unstable plant. Finally, the spindle has been realized and levitated. The simulation results are compared to the experimental results, and the performance of the spindle is discussed.

3.2 Spindle Specifications

In this section the requirements for the miniature milling spindle are described. Furthermore, disturbances acting on the spindle during the milling process are identified.

- Rotational speed of 150.000 rpm.

Current state of the art AMB milling spindles have a maximum rotational speed of 120.000 rpm. [43, 42]. The target spindle speed for this research is 150.000 rpm.

- Tooltip position error of 1.5 μm at 150.000 rpm.

In this research, the target total three-dimensional part uncertainty is 0.1 μm after two or more machining steps and processes. A high material removal rate, compared with micro Electrical Discharge Machining (μEDM) and micro Electro Chemical Machining (μECM) can be achieved with micro milling at high rotational speeds. Due to spindle runout, tool bending and geometrical errors in tool shape fabrication, the achievable shape uncertainty is limited. The final machining steps are performed using micro Electrical Discharge Machining (μEDM) and/or micro Electro Chemical Machining (μECM) at much lower rotational speeds, in order to reach the final shape uncertainty of 0.1 μm. The goal is to integrate several machining steps into one micro machining center, thus being able to perform all the required machining steps in one span. The spindle will therefore be modular, enabling its use for other processes. This thesis focuses on micro milling applications, and has a total error budget of 1.5 μm (1 σ) on the tooltip position. This budget is determined by the maximum allowable cutting depth variation on the tool tip to avoid early tool breakage. This error budget is mainly consumed by the rotor unbalance and eccentricities in tool holder, and tool geometry.

3.2.1 Disturbances

The identification of disturbances is essential in the design of a mechatronic system. Depending on the source and magnitude, unwanted disturbances can cause chatter, tool breakage, and part accuracy errors. The disturbances can be distinguished into the following contributions.

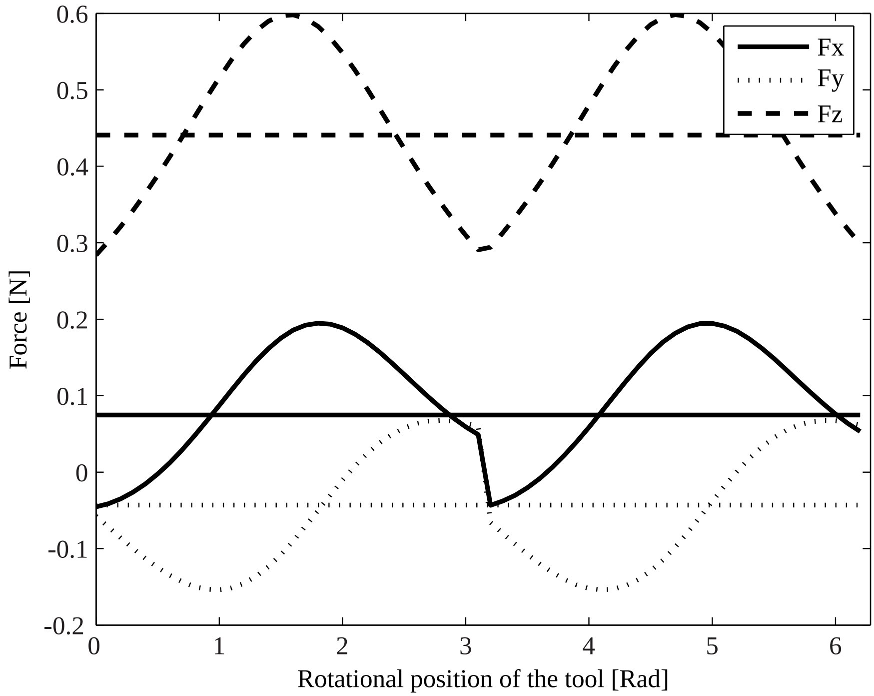

Figure 3.1: Simulated cutting forces, and their mean values, during slot milling in hard steel with a tool diameter of 0.2 mm, feed rate: 5 μm per tooth, cutting depth: 5 μm. In this simulation, z is the spindle axis and y is the feed direction.

- Cutting forces.

There are several force models for determining effects on the end mill during micro milling. In this research, a cutting force model by Dow et al. [8] was used to predict the forces acting on the tooltip during micro milling. This cutting force model has been successfully applied and verified in a tool bending compensation scheme. The modeled cutting force is a function of work piece material properties, cutting conditions, and the tool geometry. The results of this simulation are shown in figure 3.1.

Cutting forces acting on the tooltip were modeled for slot milling with a 0.2 mm tool in tool steel, with a HRC of 55. From Figure 3.1 the simulated cutting forces clearly exhibit static and dynamic parts. The mean value of the cutting force is also illustrated in Figure 3.1. The static cutting forces in x-,y-, and z-directions are: 0.08 N, -0.05 N and 0.5 N, respectively. The dynamic component has a frequency of twice the rotational speed, because the tool has two cutting edges. The amplitude of the dynamic part of the cutting force is 0.3 N. These levels for the cutting forces typical for micro milling, and have also been described in literature [9, 2].

- Stage accelerations

During stage acceleration, i.e. when cornering during milling, the static portion of the cutting force builds up. The spindle must be able to deal with this disturbance. The target acceleration for this system is where the stage reaches the optimal cutting velocity within 3 spindle revolutions. This sets the requirements on the workpiece stages with a 25 mm·s^{-1} velocity, assuming a rotational speed of 150.000 rpm. and 5 μm Feed Per Tooth (FPT). The acceleration requirement on the stage is thus 21 m·s^{-2}. The response of the spindle under the influence of the cutting force disturbances is discussed further in section 3.5.2.

- Rotor unbalance

When the rotor rotates with a frequency below the closed loop bandwidth of the system, so called sub-critical, the bearings try to force the rotor to rotate around its geometrical axis [45]. The unbalance force, f_{u1} is given by

$$f_{u1} = m\varepsilon\omega^2, \tag{3.1}$$

where ε is the distance between the rotor's inertia axis and geometrical axis, m the spindle mass, and ω the spindle rotational speed. When the rotor rotates with a rotational speed higher than the closed loop bandwidth of the bearings, so called super-critical, the rotor rotates around its inertia axis. The bearings are not able to compensate for the unbalance force. In this case, the bearing force f_{u2} is

$$f_{u2} = K\varepsilon, \tag{3.2}$$

where K is the positive bearing stiffness. From this, the spindle runout will remain due to rotor eccentricity.

- Magnetic Unbalance

The permanent magnets from the synchronous motor are not perfectly centered in the stator of the motor. Therefore, an attractive force exists between the motor stator and the permanent magnets on the rotor, synchronous with the rotational speed.

More disturbances act on the system, such as stage reaction forces, floor and frame vibrations, acoustic noise, AD and DA noise, electrical noise, turbulence, and thermal noise, which have to be considered. For this thesis, the focus is on the disturbances from the process and the effect of high rotational speeds on the performance of the system.

For an initial estimation of the influence of disturbances on the system we consider the AMB an ideal mass spring system. In this case we may write it as a Linear Time Invariant (LTI) system. The plant can then be written as G(s) and the controller can be written as C(s). Figure 3.2 schemetically shows the cutting force on the tooltip, f_c, as a disturbance input to the plant G(s), the rotor, tool, and AMB assembly.

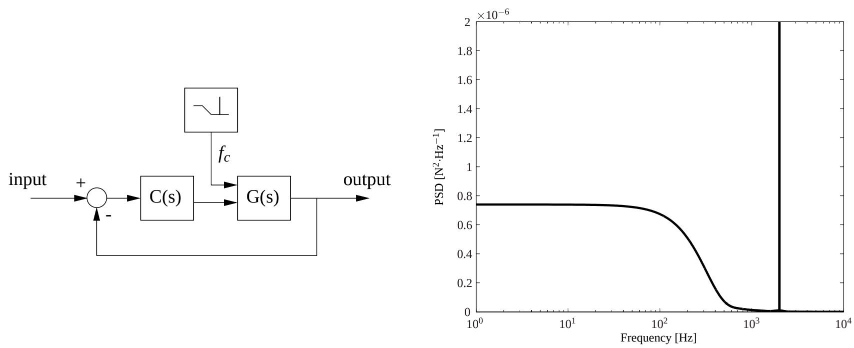

Figure 3.2: Schematic view of the controller (C), the plant (G) and the point where the cutting force disturbance enters the system (left) and Power Spectral Density (PSD) of the force disturbance on the rotor (right).

The right part of Figure 3.2 shows the Power Spectral Density (PSD) of the cutting force disturbance. In this PSD we recognize the two main disturbances as mentioned earlier, a low and a high frequency component. The low frequent part of the PSD is determined by the setpoint of the xy-stage and the magnitude of the static part of the cutting forces, in this case 0.5 N, see Figure 3.1. For this PSD, the stage is accelerated to the desired cutting speed with the parameters as mentioned earlier in this section. The stage is positioned using a third order setpoint generator. The high frequency component is visible as a high peak at the rotational frequency, in this case 2 kHz.

In this section, a first indication of the required bandwidth is made. This indication is required in the design of the AMB spindle, as the aimed bandwidth determines the requirements on the flexible resonances of the system, and the allowable phase lag introduced into the controller loop by for example sensors, filters, and the plant itself. For the estimation of the required bandwidth, the system is approximated as a mass-spring system, thus for example integral action in the controller is neglected.

The area under the PSD in figure 3.2 results in an RMS value of 0.014 N for the low frequency component of the cutting force disturbances, f_c. If the controller has to compensate for these cutting forces, with an allowable error ε, the spring must have a stiffness k_s of $f_c \cdot \varepsilon^{-1}$. When assuming a spindle mass of 0.18 kg, and requiring a maximum contribution to the error by the cutting forces of ε = 0.1 μm, an estimation of the required bandwidth can be made:

$$f_{bw} = \frac{1}{2\pi}\sqrt{\frac{k_s}{m}} = \frac{1}{2\pi}\sqrt{\frac{1.4 \cdot 10^5}{0.18}} = 140 \text{ Hz}. \tag{3.3}$$

In this research, we define the bandwidth as the frequency where the open loop transfer function, C(s)·G(s), crosses the 0-dB line.

As an example, we model an AMB system as a 1 DoF mass spring system with a negative stiffness, as described in Section 2.2.1. A mass of 0.18 kg is assumed and a negative stiffness of $1 \cdot 10^4$ N/m. A PID controller is used to stabilize the system. The PID controller has the following structure:

$$C(s) = K_p \cdot \frac{\tau_i s + 1}{\tau_i s} \cdot \frac{\tau_d s + 1}{\frac{\tau_d}{N} s + 1}, \tag{3.4}$$

with $\tau_i = 2\pi f_i$ and $\tau_d = 2\pi f_d$. In this example, the following controller settings have been used: $K_p = 16 \cdot 10^3$, f_d = 50 Hz, f_i = 20 Hz, and N = 4. The system in this example is tuned such, that it has an open loop 0-dB crossing of 140 Hz.

Figure 3.3 shows the Frequency Response Function (FRF) from a cutting force disturbance to the output of the system. The high frequency part of this transfer function can be approximated by the transfer function of a moving mass $(ms^2)^{-1}$. The FRF of the moving mass is illustrated in figure 3.3 with a dotted line. Jabben [35] shows that the PSD of the output of the system can be determined by multiplying the PSD of the input (see figure 3.2) with the corresponding transfer function (see Figure 3.3) squared. From this PSD the Cumulative Amplitude Spectrum (CAS) has been determined, shown in figure 3.3. The final value of the CAS shows that the cutting force disturbance causes in this case an RMS error of 0.16 μm on the output.

We can conclude that the spindle response to the dynamic part of the cutting forces is entirely determined by the mass of the spindle. At 2.5 kHz, the gain reduction is $0.18 \cdot (2 \cdot \pi \cdot 2500)^2 = 4 \cdot 10^7$. With a 0.1 N amplitude for the cutting force at 2.5 kHz, the resulting displacement is thus in the order of 2 nm, which is well within the specifications. Considering the dynamic part of the cutting forces, the mass can be considerably lower than 0.18 kg, and still perform within the specifications.

For reduction of the low frequent disturbances a bandwidth of at least 150 Hz is specified.

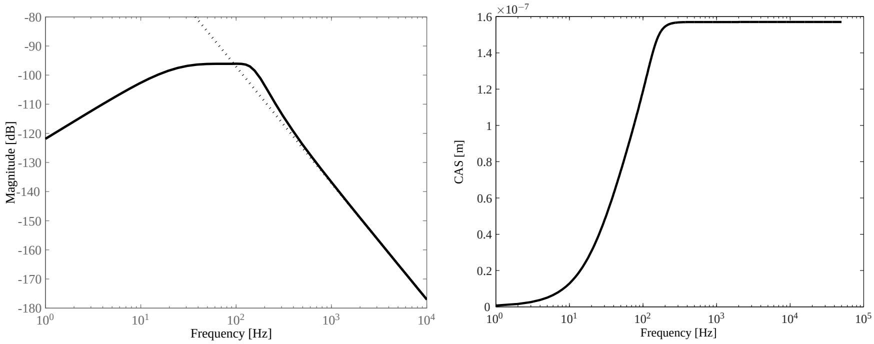

Figure 3.3: Frequency response function from a force disturbance on the spindle to the output (left) and Cumulative Amplitude Spectrum (CAS) of the output under the influence of a cutting force disturbance (right)

3.3 Design of the AMB Spindle

This section describes the design of the miniature AMB spindle.

3.3.1 Concept

In this AMB spindle concept we make use of a classical spindle bearing configuration. Two radial bearings and an axial bearing suspend the rotor in five Degrees Of Freedom (DOF). This leaves one degree of freedom unconstrained, the rotation of the rotor around its longitudinal axis. A commercially available permanent magnet (PM) synchronous motor drives the spindle around this axis.

3.3.2 Rotor

The target bandwidth of the AMB actuators is 150-200 Hz. With this goal, the aim is to keep the first flexible resonance of the spindle at least one order of magnitude higher than the bandwidth of the actuators. Furthermore, it is preferable to avoid the flexible resonances of the rotor during spin up. Thus the first resonance mode of the spindle is designed to be above 3 kHz, leaving some margin for attaching tool and toolholder which will again decrease the resonance frequency.

Magnetic bearing rotors are often laminated by press fitting a stack of laminations on a solid core to reduce eddy current losses. In our application, a solid, thus non-laminated rotor is used. A laminated rotor is not applicable, because loss of contact between the rotor and the laminations can occur at high rotational speed due to high centrifugal stresses [43]. The material properties of the rotor are listed in table 3.1. This rotor material has a higher resistivity, reducing the eddy current losses. This will be discussed further in section 3.3.4.

Table 3.1: Rotor Material Properties, Sandvik 1802

Density	$7.7 \cdot 10^3$	kg·m^{-3}
Yield strength	280	MPa
Poisson's ratio	0.3	-
Resistivity	600	nΩm
Saturation flux density	1.45	T

A thrust disk is an integral part of the rotor, and it is used in the axial bearing. The thrust disk is the part of the rotor with the largest outside diameter. Therefore, its strength determines the maximum rotational speed of the rotor. The maximum rotational speed, ω_{max} in rad·s^{-1} is determined using equation 3.5 [43]:

$$\omega_{max} = r^{-1}\sqrt{\frac{8\sigma_0}{(v+3)\rho}}, \tag{3.5}$$

where r is the radius, σ_0 is the yield strength, v is the Poisson's ratio and ρ is the density of the rotor material. The maximum theoretical rotational speed of the rotor as specified in table 3.2, without plastic deformation, is 190.000 rpm. It should be noted that a safety factor should be applied to this theoretical maximum speed to account for i.e. inhomogeneities in the rotor material. Table 3.2 lists the physical dimensions of the rotor.

Table 3.2: Rotor dimensions

Length	$130 \cdot 10^{-3}$	m
Diameter	$12 \cdot 10^{-3}$	m
Diameter thrust disk	$30 \cdot 10^{-3}$	m
Thickness thrust disk	$3 \cdot 10^{-3}$	m
Rotor weight	$1.8 \cdot 10^{-1}$	kg

A frequency analysis on the solid rotor with Finite Element Modeling (FEM), was used to determine the natural frequencies of the rotor at zero rotational speed. The modes corresponding to the rigid body resonances, as well as the first flexible natural frequency, are illustrated in figure 3.4. Section 3.6.1 describes the design of the controller, and thus the closed loop bearing stiffness, in detail. The simulation showed that the first bending mode of the rotor has a frequency of 3.4 kHz at zero rotational speed.

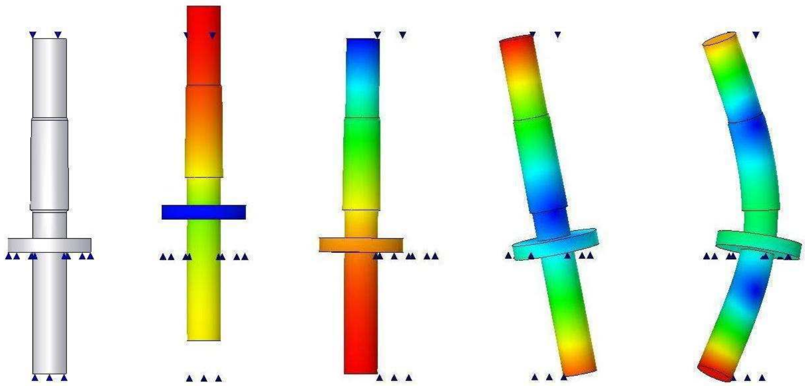

Figure 3.4: From left to right, the spindle at rest, three rigid body mode shapes, and the first flexible mode shape

3.3.3 Axial Bearing

In this section, the design of the axial bearing is described. The axial bearing consists of two magnetic actuators on each side of a thrust disk, as shown in Figure 3.5. The magnetic actuators in this setup are reluctance type actuators which consist of a circular u-shaped core with a tangentially wound coil. The core is, like the rotor, manufactured from Sandvik 1802 steel in order to reduce eddy current effects.

The force in the two reluctance actuators in differential driving mode has been derived in Chapter 2. The linearized expression for the force on the rotor in axial direction is given by:

$$F_z = K_{iz} i_z + K_z z, \tag{3.6}$$

where K_{iz} is the force current dependency and K_z is the force displacement dependency. z is the axial rotor displacement and i_z ia the axial control current. K_z is often referred to as the negative stiffness of the bearing. The bearing control current, i_z is added to the bias current i_0 of one actuator and subtracted from the bias current in

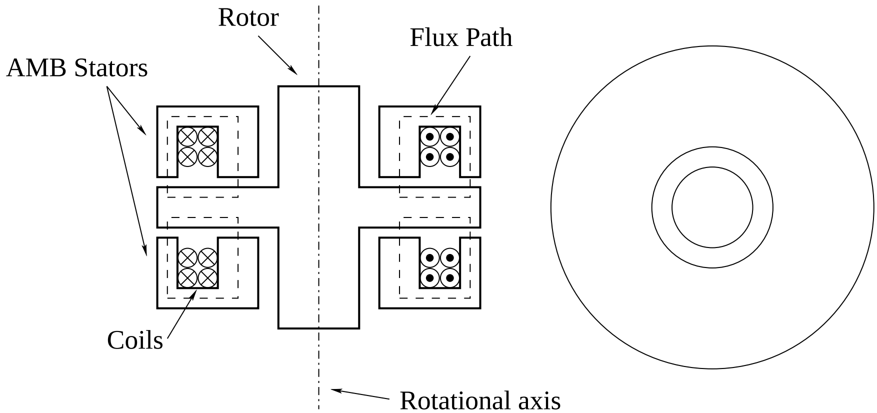

Figure 3.5: Axial bearing principle

the opposing actuator, and z is the vertical displacement of the rotor. K_{iz} and K_z are defined as:

$$K_{iz} = \frac{\mu_0 n_a^2 A_{ga} i_0}{l_{ga}^2} \quad K_z = \frac{\mu_0 n_a^2 A_{ga} i_0^2}{l_{ga}^3}, \tag{3.7}$$

where μ_0 is the magnetic permeability of air, n_a is the number of windings, A_{ga} is the pole shoe surface. Table 3.3 lists the properties of the axial bearing, these have been obtained after an iterative design and verification using FEM.

Table 3.3: Axial Bearing Properties

Pole shoe surface	A_{ga}	$1.2 \cdot 10^{-4}$	m^2
Airgap length	l_{ga}	$0.3 \cdot 10^{-3}$	m
Number of windings	n_a	80	-
Bias current	i_0	2	A
Negative stiffness	K_z	$7 \cdot 10^4$	$\mathrm{N{\cdot}m^{-1}}$
Force current dependency	K_{iz}	10	$\mathrm{N{\cdot}A^{-1}}$

3.3.4 Radial Bearings

In the radial bearings, we apply the homo-polar bearing concept, as discussed in section 2.3. The use of this configuration reduces the hysteresis losses, as well as the eddy current losses. The reduction of the losses by using a homopolar bearing concept is highly important, since the rotor is not laminated, see Section 3.3.2. The use of a rotor material with a relatively high resistivity, shown in Table 3.1, further reduces the eddy current effect.

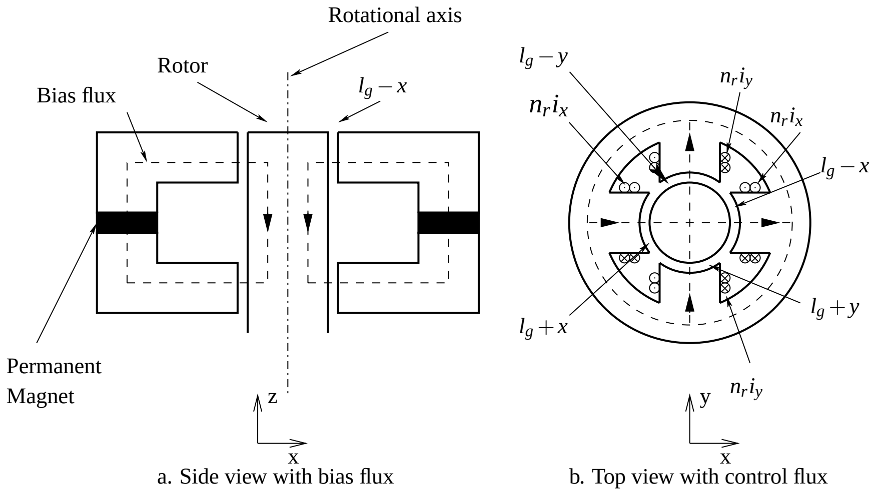

Figure 3.6: Radial bearing principle, where l_{gr} is the gap length in the radial bearing, x and y are the displacements of the rotor in x and y direction. n is the number of windings and i_x and i_y are the applied control currents in x and y direction

In the homo polar radial bearing configuration, one radial bearing consists of two four-pole stators, separated by permanent magnets. This configuration allows the placement of the AMB position sensors vertically between the two poles of one reluctance type actuator. This configuration allows for the sensor and actuator to be co-located.

A second benefit of the homopolar bearing configuration is that the two stators in one radial bearing can be used as two separate actuators. By adding two amplifiers and two controllers we can create a 4 DOF actuator from a single bearing, leaving the axial direction and the rotation unconstrained. The 4 DOF radial bearings enable future research of over actuation of the rotor shaft to suppress flexible resonances.

The determination of the force in permanent magnet biased actuators is somewhat more elaborate than for current biased actuators. For the force analysis in the radial bearings, we determine the flux in the airgap caused by the permanent magnets and the flux generated by the control coils separately. The control flux can be added to the bias flux because of the superposition principle. Again, the assumptions listed in Section 2.2 are made, in a later stage, the validity of these assumptions will be verified using Finite Element Analysis (FEM).

Equation 3.8 illustrates the application of Equation 2.2 to the right bias flux path in figure 3.6a, where s is the flux path and x is the displacement of the rotor in x-direction.

$$\oint H ds = l_{fe} H_{fe} + H_m l_m + H_{gr} 2(l_{gr} - x) = 0 \tag{3.8}$$

Where H_m is the field intensity in the permanent magnet and l_m is the length of the permanent magnet. $H_m l_m$ is also called the magnetomotive force from the permanent magnet. H_{gr} is the field intensity in the radial bearing airgap and l_{gr} is the length of the radial airgap. The law of flux conservation in Equation 2.2, also holds for this magnetic circuit, resulting in:

$$\oint B dA = 0 \quad \Leftrightarrow \quad B_{grm} A_{gr} = B_m A_m \tag{3.9}$$

Where B_{grm} is the flux density in the radial airgap caused by the permanent magnet and A_{gr} is cross sectional area of the radial bearing airgap. B_m is the flux density in the magnet, and A_m the magnet surface area. We consider the situation where the rotor is in equilibrium position, where $x = 0$. The combination of the two Maxwell equations in 2.2, together with the fact that $B_{gr} = \mu_0 H_{gr}$ leads to the "load line" of the permanent magnet in this specific circuit [46]. Figure 3.7 illustrates the load line for this magnetic circuit. The load line of a magnetic bearing circuit enables the determination of the flux density levels in the magnetic circuit, and thus the flux density in the airgap. The energy product(BH) at the intersection is a measure for the energy density that a permanent magnet can deliver to this particular magnetic circuit. The load line for this specific circuit is given by:

$$\frac{B_m}{H_m} = -\mu_0 \frac{A_{gr} l_m}{A_m 2 l_{gr}} \tag{3.10}$$

The point where the load line, equation 3.10, intersects with the demagnetization curve of the permanent magnet, is the operating point of the magnet, illustrated in Figure 3.7. From this operating point, the bias flux density in the airgap, caused by the permanent magnets(B_{grm}) can be determined, as shown in equation 3.11.

$$B_{grm} = \frac{\mu_0 l_m H_c A_m B_r}{2 A_m l_{gr} B_r + \mu_0 A_{gr} l_m H_c} \tag{3.11}$$

B_r and H_c are the remanence flux density from the permanent magnet and its coercive force. Similarly Ampère's circuital law, in Equation 2.2, applies to the magnetic circuit in radial bearings caused by the coils. Each radial bearing consists of two stators. The magnetic circuit in the radial bearing stator consist of several magnetic loops. Figure 3.8 illustrates this magnetic circuit from the bearing principle illustrated in Figure 3.6. Equation 3.12 shows the circuit equations for three

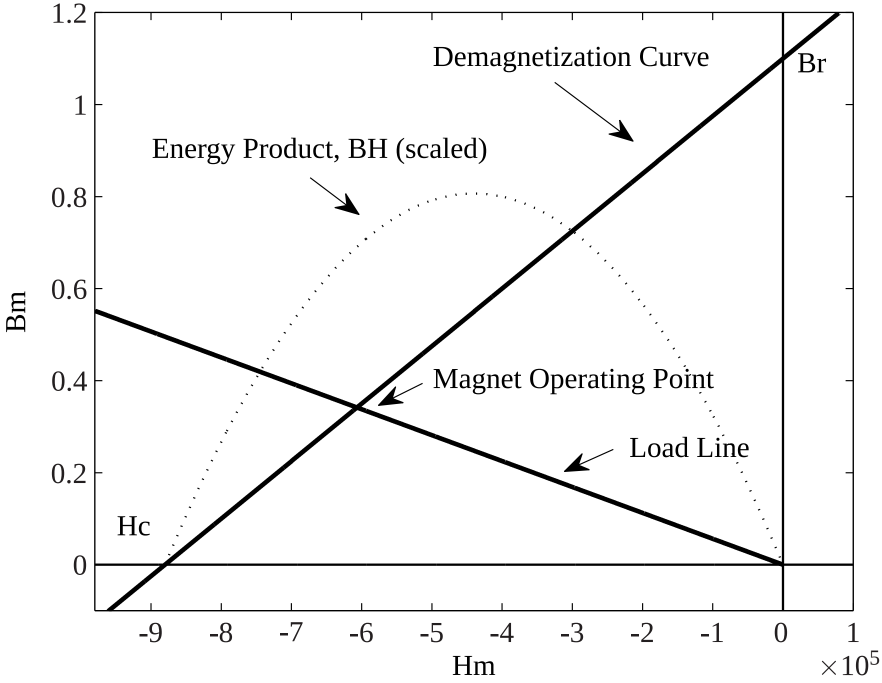

Figure 3.7: Plot of the demagnetization curve of the permanent magnet and the load line of the permanent magnet in this circuit, illustrating the magnet operating point.

of the loops shown in Figure 3.8. In equations 3.12 and 3.13 the subscript from H_g indicates the number of the corresponding airgap, as illustrated in figure 3.6.

$$\begin{array}{ll} \text{loop 1:} & H_{g1}(l_{gr}-y)-H_{g2}(l_{gr}-x)=n_r i_y - n_r i_x \\ \text{loop 2:} & H_{g2}(l_{gr}-x)+H_{g3}(l_{gr}+y)=n_r i_x + n_r i_y \\ \text{loop 3:} & H_{g3}(l_{gr}+y)-H_{g4}(l_{gr}+x)=n_r i_y - n_r i_x \end{array} \tag{3.12}$$

We apply the law of flux conservation to the magnetic circuit caused by the coils. See equation 3.13.

$$\begin{aligned} \oint BdA &= 0 \\ -B_{g1}A_{g1}-B_{g2}A_{g2}+B_{g3}A_{g3}+B_{g4}A_{g4} &= 0 \end{aligned} \tag{3.13}$$

Solving this set of equations, equations 3.12 and 3.13, results in the expression for the flux density in the radial airgaps, caused by the control coils (B_{grc}). The flux density in the right airgap, for actuation in x direction, thus with y and i_y equal to zero, is given in Equation 3.14.

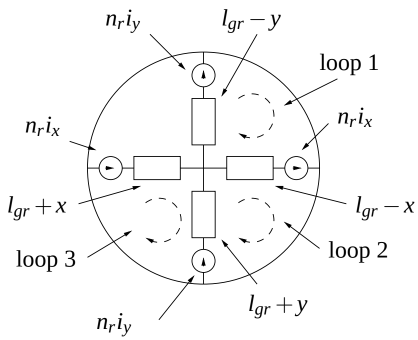

Figure 3.8: One half of a radial bearing stator illustrating the magnetic loops when considering the control flux.

$$B_{grc} = \mu_0 \frac{n_r i_x (2 l_{gr} + x)}{2 l_{gr}^2 - x^2} \tag{3.14}$$

The total flux density in the airgap is the sum of the flux caused by the permanent magnets and the flux caused by the coils. The total flux density in the right airgap (B_{gr}), with the rotor in equilibrium position is thus given by:

$$B_{gr} = \mu_0 \frac{n_r i_x (2 l_{gr} + x)}{2 l_{gr}^2 - x^2} + \frac{\mu_0 l_m H_c A_m B_r}{2 A_m l_{gr} B_r + \mu_0 A_{gr} l_m H_c}. \tag{3.15}$$

The derivation of the force in a reluctance actuator using virtual work from the flux density level in the airgap has been described in Section 2.2, Equation 2.1. Similarly, the force in the permanent magnet biased actuator is derived. Consider the force in x-direction (F_x), with a rotor displacement x and a current applied on the coils on the x-axis (i_x). Derivation of equation 3.15 for both airgaps, results in the force in x-direction,

$$F_x = \frac{B_{gr_{right}}^2 A_{gr}}{\mu_0} - \frac{B_{gr_{left}}^2 A_{gr}}{\mu_0}. \tag{3.16}$$

The net force in one direction in the radial bearing is given by

$$\begin{aligned} F_x \quad = \quad & \left(\frac{\mu_0 l_m H_c A_m B_r}{2 A_m B_r (l_{gr} - x) + \mu_0 A_{gr} l_m H_c} + \frac{\mu_0 n_r i_x (2 l_{gr} + x)}{2 l_{gr}^2 - x^2} \right)^2 \frac{A_{gr}}{\mu_0} - \\ & \left(\frac{\mu_0 l_m H_c A_m B_r}{2 A_m B_r (l_{gr} + x) + \mu_0 A_g l_m H_c} - \frac{\mu_0 n_r i_x (2 l_{gr} - x)}{2 l_{gr}^2 - x^2} \right)^2 \frac{A_{gr}}{\mu_0}, \end{aligned} \tag{3.17}$$

where H_c represents the coercive force from the magnet, B_r is its remanence flux density, A_m is the magnet surface area, l_m the magnet thickness, and A_{gr} the pole shoe surface. Equation 3.17 illustrates the force current and force gap relationship is less linear in case of a non-coplanar AMB with permanent magnets than in the case of a coplanar AMB with a bias current. This has been addressed by Lee et al. [47]. The linearization from Equation 3.6, as used for the axial bearing, does not simply apply here. However, under the assumption of small variations in the gap, the linearization of the force of the AMB with respect to current and gap is valid.

The linearized bearing force is given by

$$F_x = K_{ix} i_x + K_x x, \tag{3.18}$$

where the force position dependency, K_x, also called the negative stiffness, is given by

$$K_x = 8 \frac{l_m^2 H_c^2 A_m^3 B_r^3 A_{gr} \mu_0}{(2 A_m l_{gr} B_r + \mu_0 A_{gr} l_m H_c)^3}, \tag{3.19}$$

and where the force current dependency is given by

$$K_i = 4 \frac{\mu_0 l_m H_c A_m B_r A_{gr} n_r}{2 A_m l_{gr}^2 B_r + \mu_0 A_{gr} l_m l_{gr} H_c}. \tag{3.20}$$

3.3.5 Bearing Dimensioning

The previous section shows the dependency of the bias flux and the negative stiffness on the bearing geometry. While dimensioning the bearings, we aim to create a negative stiffness which is of the same order of magnitude or, at most one order lower, as the desired positive, or controlled stiffness. The estimate of the desired positive stiffness is given in section 3.2. The considerations which have been made to determine the optimal bias flux level are described below.

- Avoid saturation of parts of the flux path.
- No reversing of the magnetic field in the airgap.
- Operating in the linear range of the BH curve of the rotor and stator material. In this application, the rotor material has the lowest saturation flux density (1.4 T). The BH curve is almost linear up to 1 T.
- The force slew rate increases with increasing bias flux level.

Taking this into consideration, we aim to set the flux density in the airgap at 0.5 T. The initial dimensions have been chosen using the analytical model described above, the final dimensioning is done using the Finite Element Method (FEM) model described in the next section. With the above considerations, the radial Active Magnetic Bearings, including the permanent magnets can be dimensioned in an iterative fashion. Table 3.4 lists the radial bearing dimensions and properties.

Table 3.4: Radial Bearing Properties

Pole shoe surface area	A_{gr}	$3.9 \cdot 10^{-5}$	m^2
Airgap length	l_{gr}	$0.4 \cdot 10^{-3}$	m
Number of windings	n_r	30	-
Magnet area	A_m	$1 \cdot 10^{-4}$	m^2
Magnet length	l_m	$1 \cdot 10^{-3}$	m
Magnet Remanence	B_r	1.1	T
Magnet coercive force	H_c	$880 \cdot 10^3$	$A{\cdot}m^{-1}$
Force current dependency	K_i	4	$N{\cdot}A^{-1}$
Negative stiffness	K_x	$4 \cdot 10^4$	$N{\cdot}m^{-1}$

3.3.6 Finite Element Method Modeling

This section describes the verification of the flux density levels in the radial magnetic actuators using Finite Element Method (FEM) Modeling. The FEM modeling indicates whether the assumptions made in section 3.3.3 are valid. The FEM analysis has been performed using ANSYS simulation software.

Figure 3.9 shows the simulated flux density levels in a radial bearing unit with maximum actuation. Figure 3.9 shows that the assumption that no blossoming is present has been valid. The average bias flux density created by the permanent magnets in the airgap modeled using FEM was 0.55 T. The average flux density in the airgap when a current of 4 A is applied to one set of coils without permanent magnets was 0.35 T. The flux density in the airgaps with the rotor in equilibrium position when a current of 4 A is applied to one set of coils, results in flux density levels in the two upper airgaps of respectively 0.86 T and 0.21 T, as expected from the superposition principle. Figure 3.9 shows that the stator leg is close to saturation when the maximum current is applied. The FEM results generally show flux density levels considerably below what could be expected from the analytical model, likely to be caused by neglecting saturation, leakage flux, and hysteresis.

3.3.7 Position Sensors

Eddy current sensors measure the gap length variations in the AMBs. Three sensing principles have been considered for measuring the gaps, eddy current, capacitive, and optical reflective. The eddy current sensors were selected because they do not require target grounding, contrary to capacitive sensors.

In this application, a relatively large stand off between the sensor tip and the target is required. At low speeds, the rotor will spin around its geometrical axis.

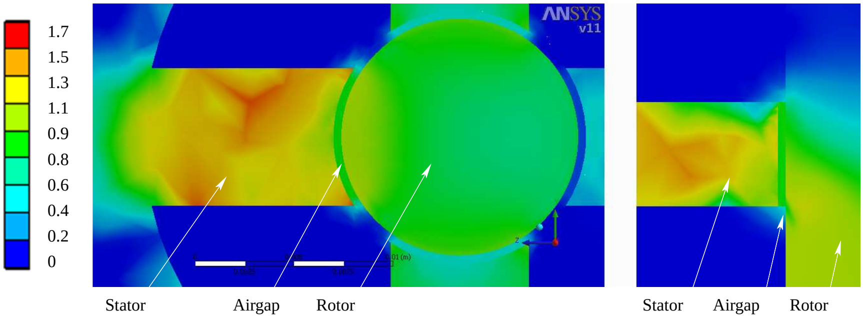

Figure 3.9: FEM simulation of the radial bearing unit

With increasing rotational speed, the unbalance force, and thus the runout increases. When the rotational speed equals a spindle resonance, rigid in this case, the response is amplified. When the operating speed further increases, the runout keeps a constant value, equal to the eccentricity in the rotor. Thus a certain displacement of the rotor while spinning up has to be allowed. Capacitive sensors of the small size suitable for our application, generally require a very small stand off from the target in order to achieve a high resolution, eddy current sensors and optical reflective sensors have a larger sensor stand off.

Furthermore, eddy current sensors are not sensitive to reflectivity changes on the rotor surface, contrary to optical sensors. The drawbacks from using eddy current sensors in this application are that they are sensitive to inhomogeneities in the ferro-magnetic rotor material. The eddy current sensors used in the miniature AMB milling spindle have a static resolution of 25 nm. The position measurement of the rotor in the magnetic bearings discussed in more detail in Chapter 7.

3.3.8 Rotational Speed Measurement

The measurement of the rotational speed is required for the implementation of a controller accounting for the changing dynamics due to the changing rotational speed. The implementation of this controller will be described in Chapter 6. Commercially available optical rotational encoders lack the bandwidth to measure the rotational speed of a spindle with very high rotational speeds. Integration of hall sensors into the spindle drive is not possible. Due to the limited dimensions and the high power of the drive, a reliable measurement cannot be performed. Therefore an angular speed measurement sensor is developed. The principle of the rotational speed measurement sensor is illustrated in Figure 3.10.

This sensor consists of a reflective opto switch and black and white segments on the spindle. The output from the opto switch is connected to two low pass,

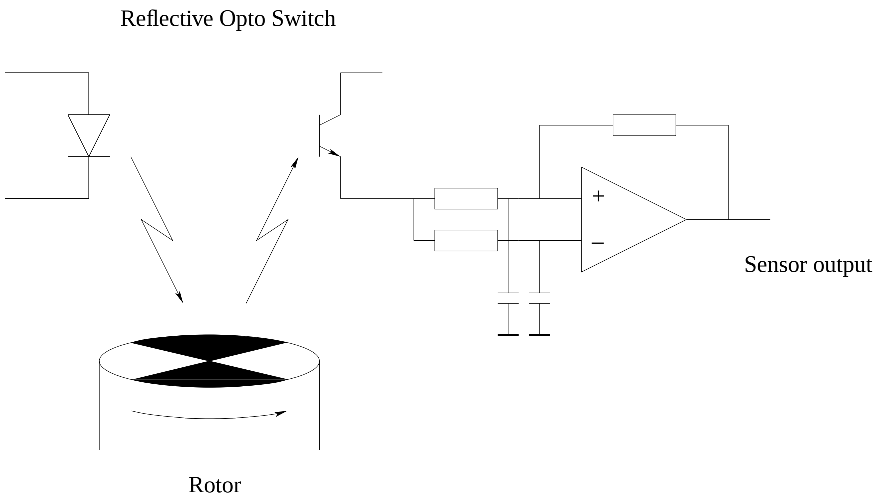

Figure 3.10: Measurement principle for the rotational speed

RC filters, both connected to the inputs of an operational amplifier. One low pass filter creates an average value, reducing the influence of ambient light. The second filter filters out the high frequency disturbances, and its output is compared to the average value from the first low pass filter. The operational amplifier is configured as a comparator, resulting in a square wave output, synchronous with twice the rotational speed.

3.3.9 Spindle Drive

A commercially available permanent magnet synchronous motor drives the spindle. The motor has been obtained from E+A in Switzerland, type mSpW 4/1.5-2-a1 Enca. The motor is a two pole, three phase drive with a slotted stator. The theoretical maximum speed of this drive is rated at 250.000 rpm. A sensorless drive has been used due to the compactness of the motor and the high rotational speed. A reliable measurement of the rotor position using hall sensors is impossible due to the compact geometry. An optical encoder could also not be used due to diameter limitations and the high rotational speed. The inverter used to drive the motor has been obtained from Sieb und Meyer, Germany, type FC-80.

3.3.10 System Overview

Figure 3.11 shows a section view of the AMB spindle. Figure 3.11 shows the rotor with on the top and bottom ends the two radial bearings consisting of the stators, permanent magnets, and the eddy current sensors. Backup bearings have been integrated in the radial and axial bearings to support the rotor when the bearings are switched off, and to catch the rotor in case of a bearing failure. The backup bearings are ceramic plain bearings. The figure also shows the axial bearing, its backup bearing, and the axial bearing sensor on the top end of the spindle. The permanent magnet synchronous motor is positioned above the axial bearing.

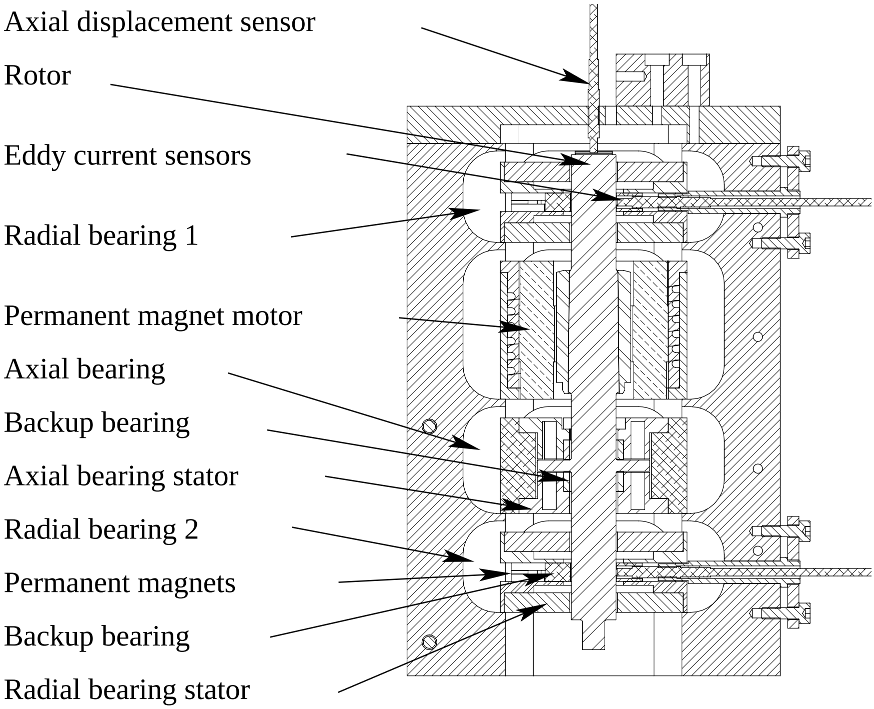

Figure 3.11: Section view of the miniature AMB spindle setup.

3.4 Realization

This section describes the fabrication of the miniature AMB spindle. Figure 3.12 shows a picture of the manufactured spindle.

The sections of the miniature spindle, the two radial bearings, the axial bearing and the electric drive, have been manufactured as cylindrical elements. The cylindrical elements have been placed in a v-groove base, to ensure an accurate and repeatable alignment of the individual spindle sections. The modular setup enables the simple replacement of the spindle sections.

Figure 3.12: Realized micro milling spindle

The rotor has been grinded from Sandvik 1802 stainless steel as described in section 3.3.4. The steel is annealed ensuring optimal magnetic properties. The annealing process is a trade off between magnetic and mechanical properties when higher rotational speeds are required. The annealing process reduces the yield strength while improving the magnetic properties of the rotor material.

A steel sleeve with the motor magnets was press-fitted onto the ground rotor. The permanent magnets are protected with a fiber sleeve. During the press-fit, the fiber sleeve is pre-tensioned. This pre-tension will retain the motor magnets at high rotational speeds.

One radial bearing stator, as described in section 3.3.4, consists of two stacks of 0.16 mm laminated sheets, manufactured by wire EDM. The stacks of laminations are then press-fit in a stainless steel housing. The two housings are joined by hand-matched permanent magnet blocks of $1\times5\times5$ mm^3. These magnets provide the bias flux. The coils consist of 30 windings per leg.

The position sensors are mounted in the force frame, the v-groove base. The position sensors provide an analogue output signal which is conditioned for the dSPACE inputs. The controller hardware is a dSPACE 1103 system, which operates at a 20 kHz sampling frequency. Using this controller and assuming one sample delay in the controller, the resulting phase lag is 7° at 400 Hz. An inverse Chebychev, low pass, anti-aliasing filter, designed with a cut off frequency of 10 kHz is applied. The anti-aliasing filter also causes a 7° phase lag at 400 Hz. Linear current source amplifiers drive the bearing coils. More information about the current source amplifiers can be found in [36].

As described in section 3.2.1, rotor balancing is crucial for the spindle performance as it operates supercritical. The rotor is dynamically balanced after press-fitting the motor magnets. The remaining unbalance in the rotor was 0.025 g·mm. This corresponds to a difference between the geometrical axis and the inertia axis of 0.15 μm.

3.5 Analysis and Simulation

This model enables the design of five Single Input Single Output (SISO) PID controllers to stabilize the system, also referred to as a decentralized controller. The model simulates the tooltip error of the system under the influence of the cutting forces from an existing cutting force model [8]. Furthermore, this model shows at which rotational speed the system becomes unstable when it is controlled by decentralized controllers. The model helps in the design of a Multiple Input Multiple Output (MIMO), centralized, control scheme. Early work on the modelling of horizontal shaft magnetic bearings has been described by Matsumara et al. [48], and later work on this subject is done by Balini et al. [49, 50] within the μ*fac* project.

3.5.1 Equations of Motion

Newton's laws require the inertial accelerations of the rotor body and are therefore best expressed in a coordinate system attached to the rotor body. The first coordinate system, defined as $\mathscr{F}_b$, coincides with the rotor's center of mass with the z-axis along the rotational axis of the rotor. The second coordinate system, $\mathscr{F}_i$, is the frame connected to the fixed world, and thus the stator of the AMB. The two reference frames, $\mathscr{F}_i$ and $\mathscr{F}_b$, differ in their orientation. Reference frame $\mathscr{F}_i$ can be expressed in $\mathscr{F}_b$ by three successive Euler rotations about each axis. There are 12 possible orders of these rotations, choosing a suitable order of rotations simplifies the system equations. In this analysis we transform $\mathscr{F}_i$ into $\mathscr{F}_b$ with a $\theta_x - \theta_y - \theta_z$ rotation order, also called a 1-2-3 system, or a tranformation using yaw, pitch, and roll angles.

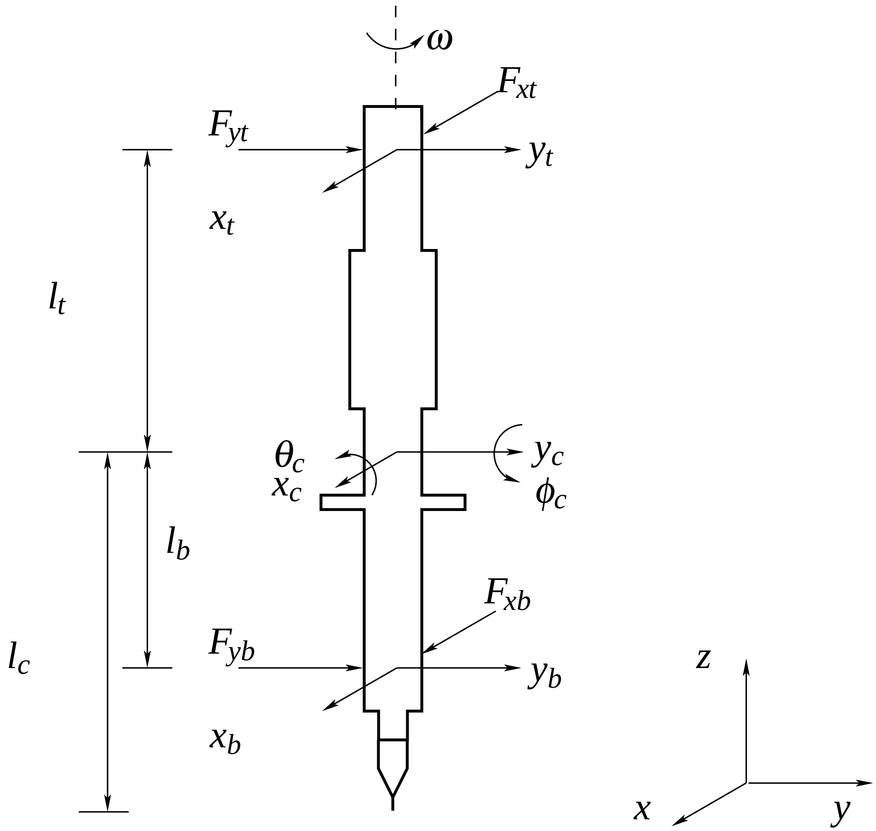

Figure 3.13: Schematic drawing of the rotor.

Equation 3.21 shows the law of conservation of linear momentum with respect to reference frame $\mathscr{F}_b$, attached to the rotor body,

$$\begin{aligned} \mathbf{F} &= \boldsymbol{m}\mathbf{a}_B \\ &= \boldsymbol{m}\left(\tfrac{d}{dt}\mathbf{v}_B + \boldsymbol{\omega}_B \times \mathbf{v}_B\right), \end{aligned} \tag{3.21}$$

where $\boldsymbol{m}$ is the rotor mass, $\mathbf{a}_B$ is the acceleration of the rotor with respect to frame $\mathscr{F}_b$ and $\mathbf{v}_B$ is the velocity of the rotor with respect to frame $\mathscr{F}_b$. In the same way, the law of conservation of angular momentum applies to the rotor. $\boldsymbol{\omega}_B$ is the angular velocity of $\mathscr{F}_b$, and thus the rotor, expressed in $\mathscr{F}_b$.

$$\mathbf{M} = \boldsymbol{I}_B \tfrac{d}{dt}\boldsymbol{\omega}_{\boldsymbol{B}} + \boldsymbol{\omega}_{\boldsymbol{B}} \times \boldsymbol{I}_B \boldsymbol{\omega}_{\boldsymbol{B}}, \tag{3.22}$$

where $\boldsymbol{I}_B$, is the inertia of the rotor. However, the equations of motion of the rotor with respect to the inertial reference frame $\mathscr{F}_i$ are of interest. We assume that the roll and pitch angles of the rotor, θ_c and ϕ_c are small. In this case, the orientation of the rotor, and thus $\mathscr{F}_b$, in the inertia frame $\mathscr{F}_i$ can be written as the vector $[\theta_c \quad \phi_c \quad \psi_c]^T$. Because θ_c and ϕ_c are small, $\cos\phi_c = 1$ and $\sin\theta_c = 0$, we can write the transformation matrix from $\mathscr{F}_i$ to $\mathscr{F}_b$ as:

$$\boldsymbol{T}_{BI} = \begin{bmatrix} \cos\psi_c & \sin\psi_c & 0 \\ -\sin\psi_c & \cos\psi_c & 0 \\ 0 & 0 & 1 \end{bmatrix}, \tag{3.23}$$

note that $\omega = \dot{\psi}_c$. Equation 3.24 shows the result of the transformation of the equations of motion in the body frame into the equations of motion in the inertia frame. We define the state vector as $\mathbf{z} = [x_c \quad \theta \quad y_c \quad \phi]^T$. The states are illustrated in Figure 3.13.

$$\mathbf{M}\ddot{\mathbf{z}} + \omega\mathbf{G}\dot{\mathbf{z}} = \mathbf{F_{bb}} \tag{3.24}$$

with

$$\begin{aligned} \mathbf{M} &= \begin{bmatrix} m & 0 & 0 & 0 \\ 0 & I_x & 0 & 0 \\ 0 & 0 & m & 0 \\ 0 & 0 & 0 & I_x \end{bmatrix} = \begin{bmatrix} \mathbf{M_1} & \mathbf{0} \\ \mathbf{0} & \mathbf{M2} \end{bmatrix} \\ \mathbf{G} &= \begin{bmatrix} 0 & 0 & 0 & 0 \\ 0 & 0 & 0 & -I_z \\ 0 & 0 & 0 & 0 \\ 0 & I_z & 0 & 0 \end{bmatrix} = \begin{bmatrix} \mathbf{0} & \mathbf{G_1} \\ \mathbf{G_2} & \mathbf{0} \end{bmatrix}, \end{aligned} \tag{3.25}$$

where $\mathbf{F}$ are the forces acting on the rotor. F_{xt}, F_{yt}, F_{xb} and F_{yb} are the forces acting on the rotor from the top and bottom AMB respectively. Using the linearized forces from the magnetic actuators, the forces from the AMBs are

$$\mathbf{F_{bi}} = \begin{bmatrix} F_{xt} & F_{yt} & F_{xb} & F_{yb} \end{bmatrix}^T = \mathbf{K_i}\mathbf{i} + \mathbf{K_g}\mathbf{x}. \tag{3.26}$$

Equation 3.26 contains the forces derived in section 3.3.4 and Equation 3.18, written for the four radial actuators in the inertia frame. $\mathbf{i}$ is a vector with the actuator control currents and $\mathbf{x}$ contains the displacements of the rotor in the airgaps. The force current dependency, $\mathbf{K_i}$, and the negative stiffness matrix $\mathbf{K_g}$ are diagonal matrices described by:

$$\begin{aligned}
\mathbf{K_i} &= \begin{bmatrix} K_i & 0 & 0 & 0 \\ 0 & K_i & 0 & 0 \\ 0 & 0 & K_i & 0 \\ 0 & 0 & 0 & K_i \end{bmatrix} = \begin{bmatrix} \mathbf{K_{i1}} & \mathbf{0} \\ \mathbf{0} & \mathbf{K_{i2}} \end{bmatrix} \\
\mathbf{K_g} &= \begin{bmatrix} K_g & 0 & 0 & 0 \\ 0 & K_g & 0 & 0 \\ 0 & 0 & K_g & 0 \\ 0 & 0 & 0 & K_g \end{bmatrix} = \begin{bmatrix} \mathbf{K_{g1}} & \mathbf{0} \\ \mathbf{0} & \mathbf{K_{g2}} \end{bmatrix}.
\end{aligned} \tag{3.27}$$

Now, we have the equations of motion described COG coordinates of the rotor, and the bearing forces as a function of rotor displacements in the bearings. Matrix **C**, which contains the distances from the bearings to the COG, transforms the translation and rotation of the Center Of Gravity (COG) of the rotor to the variation in the gaps in the AMBs, thus $\mathbf{x} = \mathbf{Cz}$. Naturally, $\mathbf{C}^T$ transforms the forces from the AMBs back into to forces and moments acting in the COG of the rotor, $\mathbf{F_{bb}} = \mathbf{C}^T\mathbf{F_{bi}}$. **C** is given by:

$$\mathbf{C} = \begin{bmatrix} 1 & l_t & 0 & 0 \\ 1 & -l_b & 0 & 0 \\ 0 & 0 & 1 & -l_t \\ 0 & 0 & 1 & l_b \end{bmatrix} = \begin{bmatrix} \mathbf{C_1} & \mathbf{0} \\ \mathbf{0} & \mathbf{C_2} \end{bmatrix}. \tag{3.28}$$

To write the system in state space form, we define the state vector, containing the gaps and their derivatives as:

$$\mathbf{x_1} = \begin{bmatrix} x_t \\ x_b \\ \dot{x}_t \\ \dot{x}_b \end{bmatrix} \qquad \mathbf{x_2} = \begin{bmatrix} y_t \\ y_b \\ \dot{y}_t \\ \dot{y}_b \end{bmatrix}. \tag{3.29}$$

The complete state space system of the plant can be described as

$$\begin{aligned}
\begin{bmatrix} \dot{\mathbf{x}}_\mathbf{1} \\ \dot{\mathbf{x}}_\mathbf{2} \end{bmatrix} &= \begin{bmatrix} \mathbf{A_1} & \omega\mathbf{A_{12}} \\ \omega\mathbf{A_{21}} & \mathbf{A_2} \end{bmatrix} \begin{bmatrix} \mathbf{x_1} \\ \mathbf{x_2} \end{bmatrix} + \begin{bmatrix} \mathbf{B_1} & \mathbf{0} \\ \mathbf{0} & \mathbf{B_2} \end{bmatrix} \begin{bmatrix} \mathbf{i_1} \\ \mathbf{i_2} \end{bmatrix} \\
\begin{bmatrix} \mathbf{y_1} \\ \mathbf{y_2} \end{bmatrix} &= \left[\begin{array}{cc|cc} \mathbf{I} & \mathbf{0} & \mathbf{0} & \mathbf{0} \\ \mathbf{0} & \mathbf{0} & \mathbf{I} & \mathbf{0} \end{array}\right] \begin{bmatrix} \mathbf{x_1} \\ \mathbf{x_2} \end{bmatrix},
\end{aligned} \tag{3.30}$$

where

$$\begin{aligned}
\mathbf{A_1} &= \begin{bmatrix} \mathbf{0} & \mathbf{I} \\ (\mathbf{M_1 C_1}^{-1})^{-1}(\mathbf{C_1}^T \mathbf{K_{g1}}) & \mathbf{0} \end{bmatrix} \\
\mathbf{A_2} &= \begin{bmatrix} \mathbf{0} & \mathbf{I} \\ (\mathbf{M_2 C_2}^{-1})^{-1}(\mathbf{C_2}^T \mathbf{K_{g2}}) & \mathbf{0} \end{bmatrix} \\
\mathbf{A_{12}} &= \begin{bmatrix} \mathbf{0} & \mathbf{0} \\ \mathbf{0} & -(\mathbf{M_1 C_1}^{-1})^{-1}\mathbf{G_{12} C_2}^{-1} \end{bmatrix} \\
\mathbf{A_{21}} &= \begin{bmatrix} \mathbf{0} & \mathbf{0} \\ \mathbf{0} & -(\mathbf{M_2 C_2}^{-1})^{-1}\mathbf{G_{21} C_1}^{-1} \end{bmatrix} \\
\mathbf{B_1} &= \begin{bmatrix} \mathbf{0} \\ (\mathbf{M_1 C_1}^{-1})^{-1}(\mathbf{C_1}^T \mathbf{K_{i1}}) \end{bmatrix} \\
\mathbf{B_2} &= \begin{bmatrix} \mathbf{0} \\ (\mathbf{M_2 C_2}^{-1})^{-1}(\mathbf{C_2}^T \mathbf{K_{i2}}) \end{bmatrix},
\end{aligned} \tag{3.31}$$

with $\mathbf{i}$ as input currents and $\mathbf{y}$, the variation of the gaps as outputs. This notation is allowed when $\mathbf{C_1}$, $\mathbf{C_2}$, $\mathbf{M_1 C_1^{-1}}$, and $\mathbf{M_2 C_2^{-1}}$ are invertable. This is the case since they are full rank, l_t will never equal $-l_b$. The state space system of the plant can in a short form be written as:

$$\begin{aligned}
\dot{\mathbf{x}}_\mathbf{p} &= \mathbf{A_p}(\omega)\cdot \mathbf{x_p} + \mathbf{B_p}\cdot \mathbf{u} \\
\mathbf{y} &= \mathbf{C_p}\cdot \mathbf{x_p} + \mathbf{D_p}\cdot \mathbf{u}
\end{aligned}, \tag{3.32}$$

with $\mathbf{D_p} = 0$ and where $\mathbf{x_p}$ represents the states of the plant, $\mathbf{u}$ the input to the plant, and $\mathbf{y}$ the output. The PID controllers have the structure as described in Section 3.2.1, we can also write them in state space form:

$$\begin{aligned}
\dot{\mathbf{x}}_\mathbf{c} &= \mathbf{A_c}\cdot \mathbf{x_c} + \mathbf{B_c}\cdot (\mathbf{r}-\mathbf{y}) \\
\mathbf{u} &= \mathbf{C_c}\cdot \mathbf{x_c} + \mathbf{D_c}\cdot (\mathbf{r}-\mathbf{y})
\end{aligned}, \tag{3.33}$$

where $\mathbf{x_c}$ contains the controller states and $\mathbf{r}$ is the reference. This is a diagonal system with the PID controllers on the diagonal. Combining the systems and closing the loop gives us the state space matrices for the closed loop system:

$$\begin{aligned}
\dot{\mathbf{x}} &= \begin{bmatrix} \mathbf{A_p}(\omega) - \mathbf{B_p D_c C_p} & \mathbf{B_p C_c} \\ -\mathbf{B_c C_p} & \mathbf{A_c} \end{bmatrix} \cdot \mathbf{x} + \begin{bmatrix} \mathbf{B_p D_c} \\ \mathbf{B_c} \end{bmatrix} \cdot \mathbf{r} \\
\mathbf{y} &= \begin{bmatrix} \mathbf{C_p} \\ \mathbf{0} \end{bmatrix} \cdot \mathbf{x}
\end{aligned} \tag{3.34}$$

Other systems such as anti aliasing filters, sampling delays, and digital filtering have been added in the same way.

3.5.2 Simulation Results

In this section, we simulate the response of the spindle under the influence of the cutting forces. The cutting forces consist of a static part and a dynamic part. The cutting forces on the tooltip are simulated during slot milling with a 0.2 mm diameter tool in hardened steel. The rotational speed is set at 150.000 rpm. The simulations in this section are performed with the controller as implemented in the actual system, the controller parameters are listed in Table 3.5. More information on the controller design is given in Section 3.6.3.

Table 3.5: Controller settings

Tilting mode			Translational mode		
Kp	$30 \cdot 10^3$	[-]	Kp	60	[-]
f_i	20	Hz	f_i	10	Hz
f_d	100	Hz	f_d	170	Hz
N	15	[-]	N	15	[-]

First, the response of the tooltip to the static part of the cutting force has been simulated. The static part of the cutting force builds up when the workpiece accelerates to cutting velocity, i.e. when cornering during milling. This assumes the stage accelerates to 25 mm·s^{-1} in 0.0012 s, which corresponds to three spindle revolutions when milling at 150.000 rpm. The magnitude of the static part of the cutting force 0.1 N was simulated. Figure 3.14 shows the response of the tooltip in x- and y-directions when the static part of the cutting force was applied only in x-direction.

Figure 3.14 shows that the maximum response of the tooltip was 3.6 µm. Figure 3.14 also shows a response of the tooltip in the y-direction, which is a result of the gyroscopic coupling in the fast rotating spindle. In this simulation, the stage had a constant acceleration and the tooltip response will improve with a less aggressive acceleration profile.

Second, we simulated the tooltip response to the dynamic portion of the cutting force in the x-direction. The dynamic part of the cutting force was simulated with a sinusoidal cutting force of 0.3 N and an excitation of twice the rotational speed, 5 kHz, see section 3.2.

Figure 3.15 shows that the maximum response of the tooltip is in the order of 0.1 µm. Therefore it can be concluded that the spindle design performs within specifications when considering the dynamic part of the cutting forces. Section 3.6.2 and 3.6.3 describe the implementation of a more advanced, centralized controller on the realized system, also showing the increase in performance.

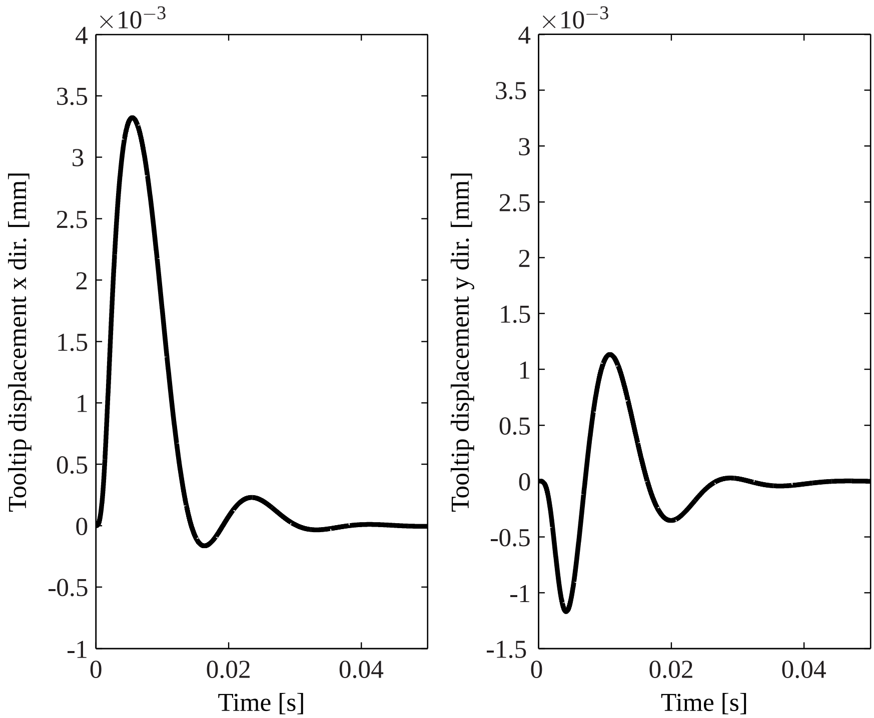

Figure 3.14: Tooltip response in x and y direction when the static part of the cutting force(0.1 N) is applied in x-direction. The workpiece accelerates with 21 $m{\cdot}s^{-1}$ and we simulate full slot milling in hard steel with a tool diameter of 0.2 mm at a rotational speed of 150.000 rpm.

3.6 Experimental Results

In this section the design of the spindle controller is presented. The measured frequency responses are compared with the simulated responses of the system using the model discussed in the previous sections.

3.6.1 Controller

The AMB open loop transfer function has been simulated using the model described in section 3.5. Initially a decentralized PD controller has been designed using this modeled open loop transfer function. The model uses a linearized expression of the non-linear plant. The PD controllers stabilize the open loop inherently unstable plant, enabling system identification to properly tune the system. In the decentralized controller, the rotor position in a bearing is the input, and the current to that

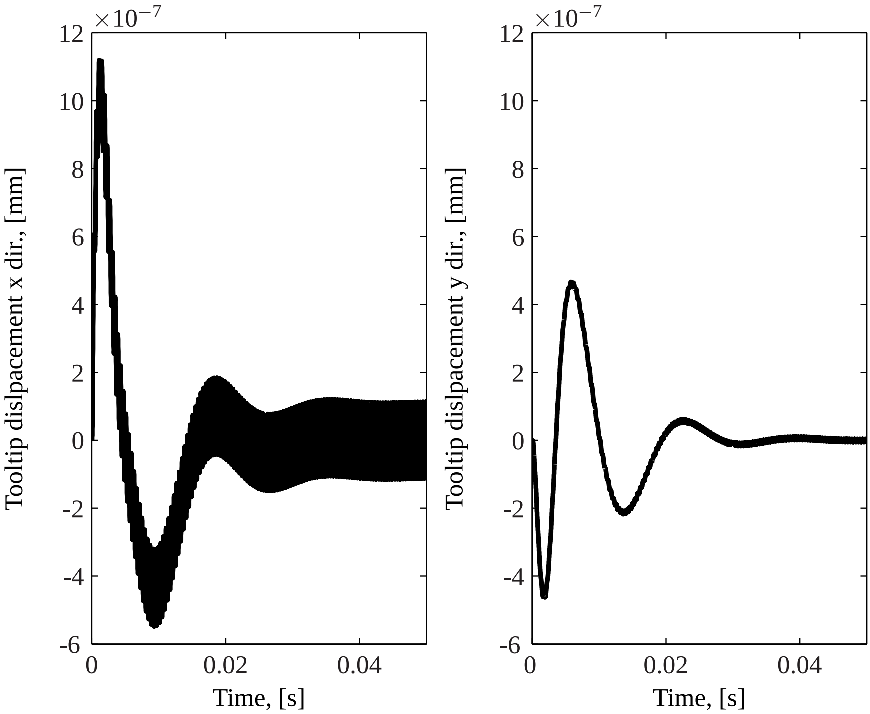

Figure 3.15: Tooltip response in x and y direction when the dynamic part of the cutting force(amplitude: 0.3 N) is applied in x-direction. We simulate full slot milling in tool steel with a tool diameter of 0.2 mm at a rotational speed of 150.000 rpm.

same bearing is the output of the controller. Figure 3.19a illustrates this control principle.

To investigate the quality of the model, and the performance of the radial bearing actuators, the frequency response function (FRF) of the plant has been measured. Many of the frequency response function measurements in this thesis have been performed in close co-operation with Blom [28]. The open loop plant is unstable, therefore the FRFs have been measured in closed loop. The plant FRFs have been estimated using a Joint Input-Output estimator (JIO) [51]. In the JIO estimator, plant G is estimated using

$$\hat{G} = \mathbf{Y} \cdot \mathbf{R}^H \left[\mathbf{U} \cdot \mathbf{R}^H\right]^{-1}, \tag{3.35}$$

where $\mathbf{Y}$ is the Discrete Fourier Transform (DFT) of the output signal, and $\mathbf{U}$ and $\mathbf{R}$ are the DFTs of the input and reference signals respectively. H stands for the

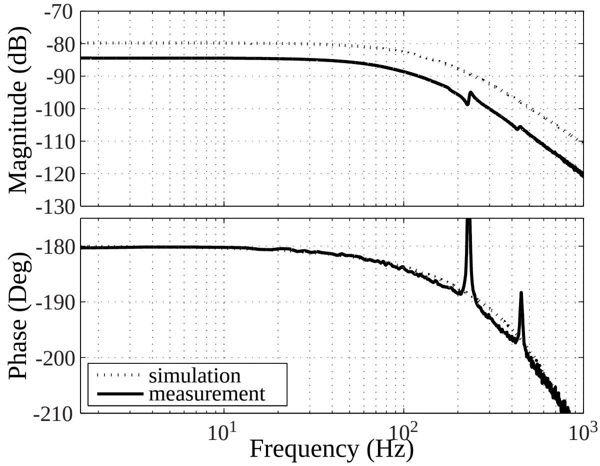

Figure 3.16: Frequency response of the plant at 0 rpm, rotor displacement over input current (y/u), simulated as wel as measured.

complex conjugate transpose. This method has been chosen because it is less sensitive to distortion of the FRF due to low Signal to Noise Ratios (SNRs) compared to for example an H_1 estimator. More detailed information about the closed loop system identification of non linear AMB systems can be found in [28].

The measured response is illustrated in figure 3.16. The phase lag due to the use of a digital controller is assumed to be one sample, and is included in the simulated response, as well as the anti-aliasing filter. The anti-aliasing filter is a third order, inverse chebychev analog filter. We are interested in the additional phase lag in the actuator because a non-laminated rotor is applied. Figure 3.16 shows an additional phase lag of 7° to the simulated response at 500 Hz. The total phase lag at 500 Hz in the plant is 22°. The additional phase lag can only be partly explained by the eddy current effect, the lags introduced by the eddy-current sensors and the current amplifiers have also not been included in the model.

Figure 3.16 shows a difference of 4 dB in the simulated and measured gain of the plant. The negative stiffness has been predicted quite accurately. The resonance peaks are caused by the dynamics of the spindle suspension. This measurement has been performed with the spindle attached to the vertical stage described in Chapter 5. These peaks were not present when the transfer is measured with the spindle attached directly to a granite block.

Figure 3.17 shows the frequency response of the plant over a wider frequency range. Figure 3.17 clearly shows the first flexible resonance of the spindle shaft at

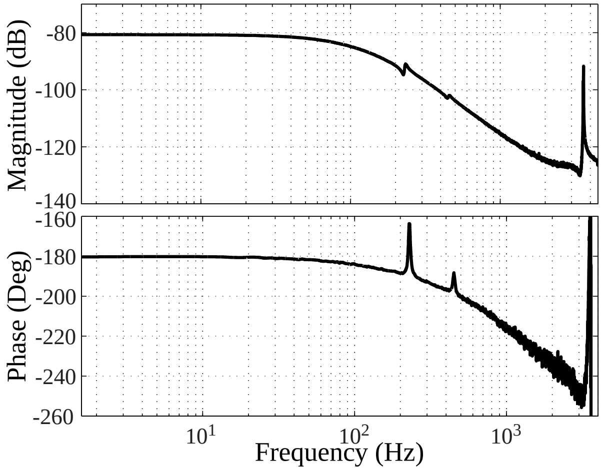

Figure 3.17: Frequency response of the plant at 0 rpm, rotor displacement over input current (y/u), showing the first bending mode of the rotor at 3400 Hz.

3.4 kHz. This was modeled with FEM in Section 3.3.2.

3.6.2 Modal Controller

Figure 3.18 shows the measured gain plots of the MIMO plant, radial bearings only. This figure shows the cross coupling between the magnetic bearing actuators. On the diagonal, the plant responses as shown in Figures 3.16 and 3.17 can be recognized. According to the theoretical model, only a coupling between the top and bottom actuators in the same plane can be expected, thus between top x and bottom x, and between top y and bottom y. This coupling is visible in figure 3.18. An additional coupling between the x and y direction in one bearing is present, this is magnetic cross talk. This cross talk can for example caused by the fact that the rotor is not exactly centered in the bearing center, as assumed in Section 3.3.4. The remaining off-diagonal terms are minimal.

In the decentralized control scheme, the MIMO plant is controlled using SISO controllers. Reasonable results have been achieved with the decentralized controller. However when using a decentralized controller, the individual modes and their resonances can not be influenced.

Therefore, a centralized controller has been developed. The four degrees of freedom in the radial bearings are transformed into statically decoupled DOFs, also referred to as a modal controller [52] or as COG decoupled controller. The trans-

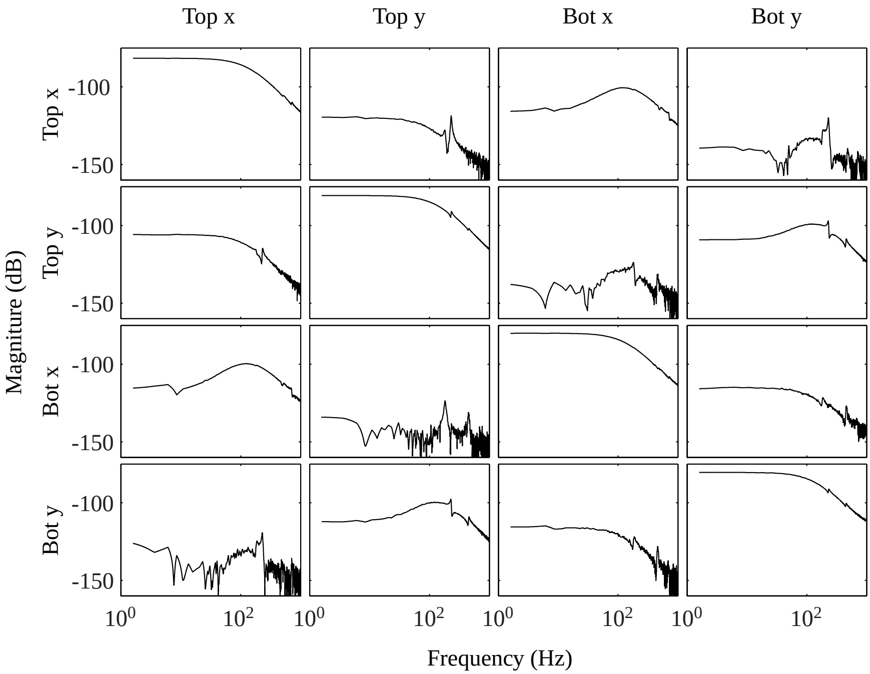

Figure 3.18: Frequency response gain plots of the MIMO plant at 0 rpm, radial bearings only. Rotor displacements over input currents $(\mathbf{y}/\mathbf{u})$

formation matrix $\mathbf{C}^{-1}$ transforms the displacements in the top and bottom bearing into a translation and a rotation around the Center of Gravity (COG) of the rotor, see section 3.5. PID controllers control the translation and rotation of the COG. $(\mathbf{C}^T)^{-1}$ transforms the required force in the COG and the required moment around the COG back to forces in the top and bottom bearing. The working principle of the static decoupling is illustrated in Figure 3.19b. Static decoupling simplifies the controller design and allows control of the rigid modes of the rotor.

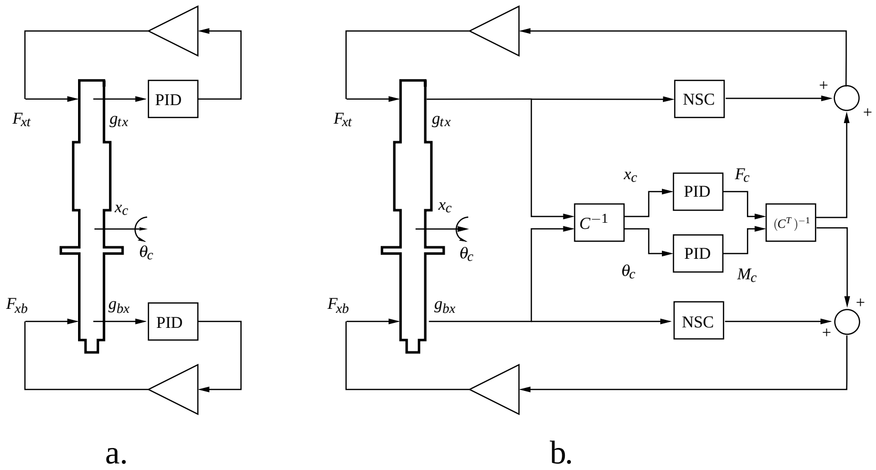

Figure 3.19: Two control schemes, the decentralized controller, figure a. and the modal controller including the negative stiffness compensation (NSC), figure b.

3.6.3 Negative Stiffness Compensation

The tranformation of bearing coordinates to COG coordinates does not entirely decouple the system. The negative stiffness in the bearings couples the COG motions when the COG is not exactly positioned between the two bearings. Therefore a Negative Stiffness Compensation (NSC) has been implemented to entirely decouple the system. The NSC consists of a local proportional feedback loop, illustrated in Figure 3.19. The proportional gain of this loop is chosen identical to the negative stiffness of the bearings. The negative stiffness of the bearings has been determined from the plant transfer function, see Figure 3.16. Since this proportional term is a linear approximation of the negative stiffness, the negative stiffness compensation is only effective for small displacements. With the negative stiffness of the rotor compensated, the COG controllers of the rotor can be designed.

The static decoupling, and the negative stiffness compensation have been implemented on the AMB system. The PID controllers are structured as described in Section 3.2.1, equation 3.4. The initial controller settings have been designed using Ziegler-Nichols tuning rules. Subsequently they have been iteratively improved, while observing the spindle positioning error, and ensuring stability over the entire speed range. The controller settings for the translation and tilting modes of the rotor are listed in table 3.6, the controllers in two vertical planes are identical. Figure 3.20 shows the frequency response functions of the two controllers.

Table 3.6: Controller settings

Tilting mode			Translational mode		
Kp	$30 \cdot 10^3$	[-]	Kp	60	[-]
f_i	20	Hz	f_i	10	Hz
f_d	100	Hz	f_d	170	Hz
N	15	[-]	N	15	[-]

The open loop frequency response functions are shown in figure 3.21. Figure 3.22 shows a zero dB crossing of 180 Hz for the translation of the COG and a zero dB crossing of 220 Hz for the tilting of the rotor around the COG. As shown in Section 3.5 the plant dynamics depend on the rotational speed. The PID controllers have been designed at zero rotational speed, while checking the stability over the entire operating range. The influence of the rotational speed will be discussed in the next section, Section 3.6.4. The design of a controller accounting for the rotational speed dependency of the plant will be discussed in Chapter 6.

Figure 3.22 shows the closed loop response of two controlled modes in one vertical plane.

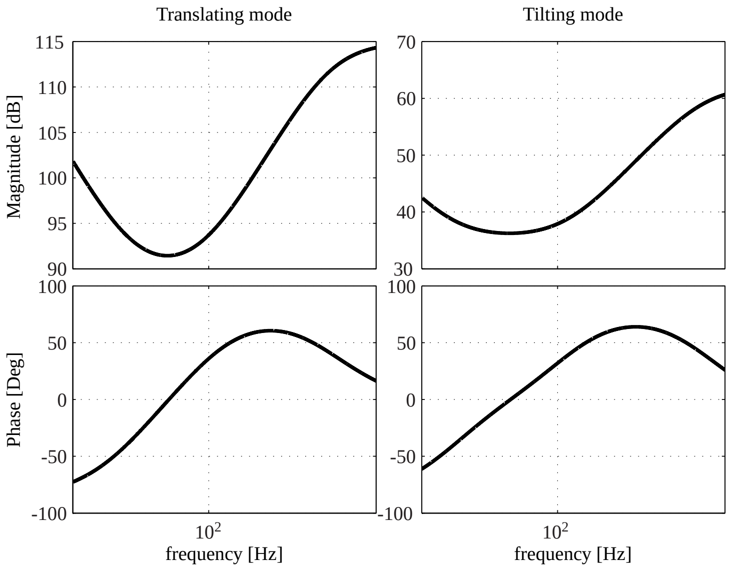

Figure 3.20: Frequency responses of the controllers of the tilting and translational modes of the rotor in the vertical plane.

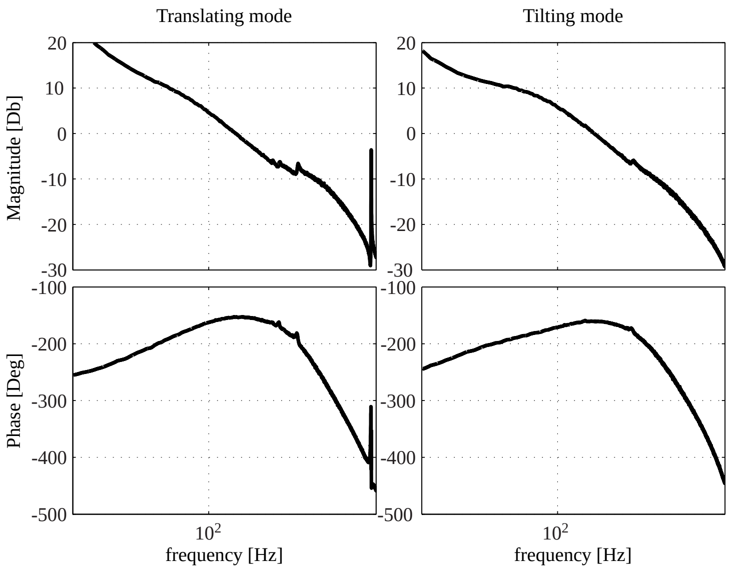

Figure 3.21: Measured open loop frequency response of the translating mode and the tilting mode of the rotor in the vertical plane.

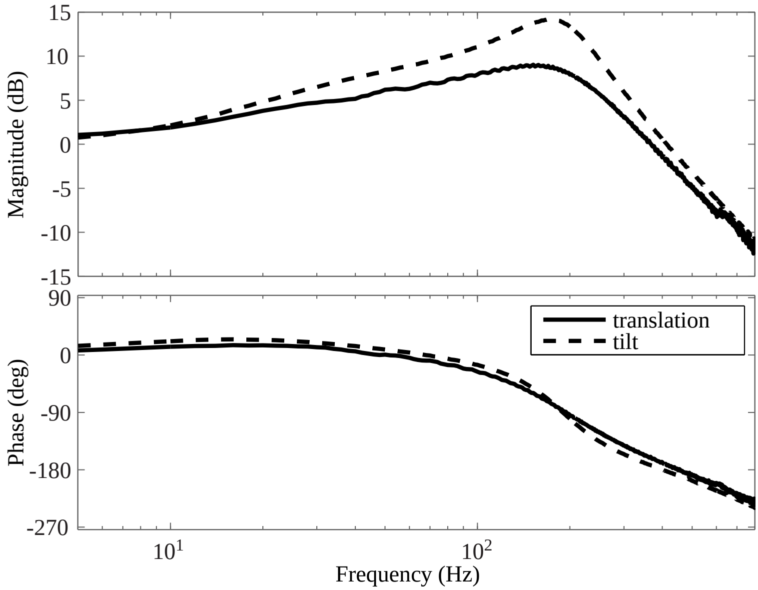

Figure 3.22: Measured closed loop frequency response of two controlled modes, translation and tilting. Reference over output in COG coordinates.

3.6.4 Mode Splitting

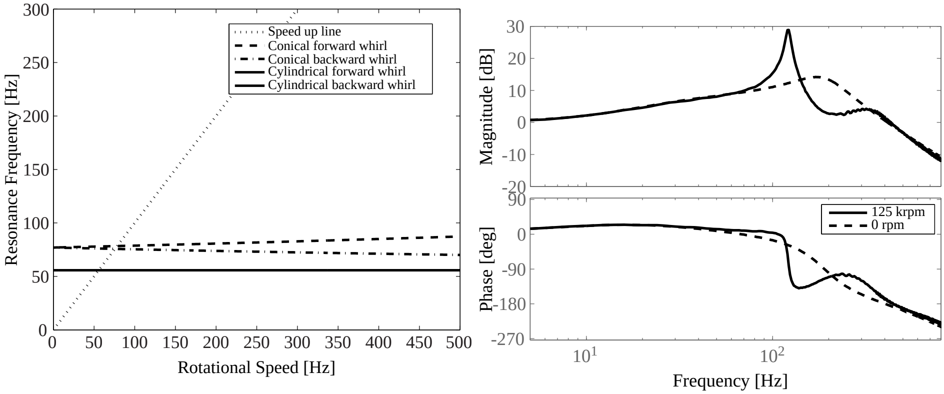

Figure 3.23: Simulated Campbell diagram, illustrating the resonances of the system, depending on the rotational speed (left) and Measured closed loop frequency response of the tilt mode at 0 rpm and at 125.000 rpm. Reference over output in COG coordinates. One recognizes the splitting of the modes at 125.000 rpm (right).

A Campbell diagram shows the dependency of the resonance frequencies of a rotor as function of the rotational speed. Figure 3.23 shows the simulated Campbell diagram of the realized spindle. The resonances corresponding to the tilting modes depend on the rotational speed. Figure 3.23 shows the splitting of the tilting mode into a forward whirl mode and a backward whirl mode with increasing rotational speed, also referred to as gyroscopic stiffening. The translational modes do not depend on the rotational speed when the COG is located exactly in the middle between the two radial bearings.

The mode splitting has been measured by taking the closed loop frequency response of the tilting mode at zero rotational speed and at 125.000 rpm. Figure 3.23 shows the measured closed loop response of the tilting mode for two rotational speeds, and the splitting of the resonance peak into two peaks at 125.000 rpm. The highly amplified peak at 100 Hz illustrates the importance of accounting for the rotational speed in the controller. The design of such a controller will be discussed in Chapter 6. The simulated Campbell plot shows resonances well below the measured resonance peaks, this is caused by a simplification of the model. The delays due to sampling and anti aliasing filtering have not been accounted for in this simulation.

3.6.5 Spindle Performance

This section describes the performance of the AMB spindle. The Cumulative Power Spectral Density (CPSD), and the Cumulative Amplitude Spectrum (CAS) measurements of the error signals are considered. The final value of the CAS graph equals the RMS value of the of the error signal (1 σ), and thus gives an indication of the system performance. The Cumulative Power Spectral Density gives more information of the contribution of the individual frequency components to the final error, as described section 3.2.1. The CAS is calculated by taking the square root of the Cumulative Power Spectrum of the error signal. Figure 3.24 shows the measurement of the CAS of the error signal at zero rotational speed. The final values of the radial bearing errors are: 0.035 μm and 0.038 μm for the top bearing and 0.029 and 0.037 μm for the bottom bearing. The final value of the axial bearing error is: 0.020 μm. The PSD shows that a large contribution to the error enters at 50 Hz and its higher orders.

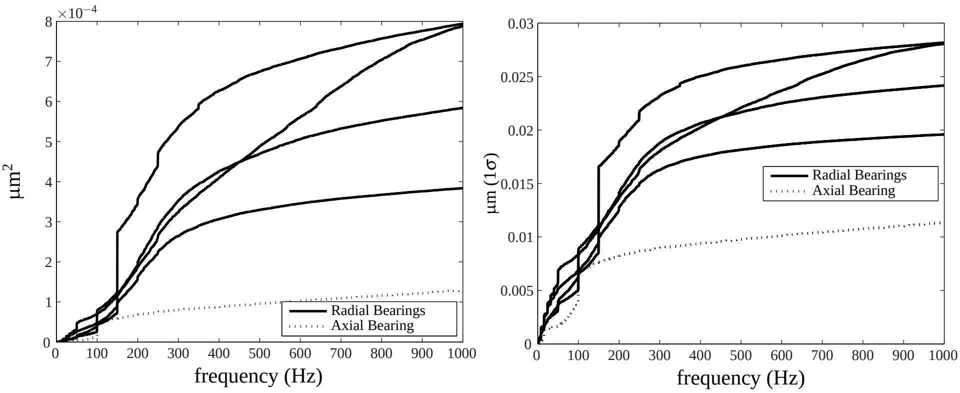

Figure 3.24: The Cumulative Power Spectral Density (CPSD) (left) and the Cumulative Amplitude Spectrum (CAS) (right) of the error signals in the miniature AMB spindle at zero rpm.

Figure 3.25 shows the measurement of the CAS of the error signal at 125.000 rpm. The final values of the radial bearing errors are: 7.2 and 7.5 μm for the top bearing, and 5.9 and 6.9 μm for the bottom bearing. The final value of the axial bearing error is: 0.48 μm. One can see that the main contribution to the error signal is the disturbance at 2.1 kHz, the rotational speed. The contribution for the radial bearings at this frequency are 6.5 and 6.8 μm for the top bearing and 4.0 and 4.6 μm for the bottom bearing. This synchronous error is larger than one would expect from the mass unbalance from the rotor, which was previously stated to be 0.15 μm.

A possible cause for the remaining error is that the sensor measures the unroundness of the spindle shaft. This is expected to be the main contributor to the error signal. Furthermore, the measurement of a ferromagnetic target using an eddy current sensor is known to introduce a runout effect in the measurement due to inhomogenities in the target material. Another contributor to the measured spindle error can be vibrations in the spindle housing in which the sensors are mounted. These vibrations can be introduced by the spindle drive. Further research is required to investigate these hypotheses.

Note that in these cases, the tool tip displacement is much smaller than the measured sensor error. The gain in the closed loop frequency response function at 125.000 rpm is -40 dB, extrapolated from figure 3.22. An error of 7 μm introduced by the sensor would thus result in a displacement of the rotor of 0.07 μm of the rotor. This sensor displacement can be further reduced by filtering at the rotational frequency. This requires a filtering at a specific frequency, like a notch filter, which is shifting with the rotational speed. This is a recommendation for future improvement of the spindle setup. The challenge of the attenuating synchronous disturbances using LPV control is picked up by Balini [49, 50] within the *μfac* project.

In Chapter 7, more detail is given about the position sensors, and the evaluation of alternative sensing principles.

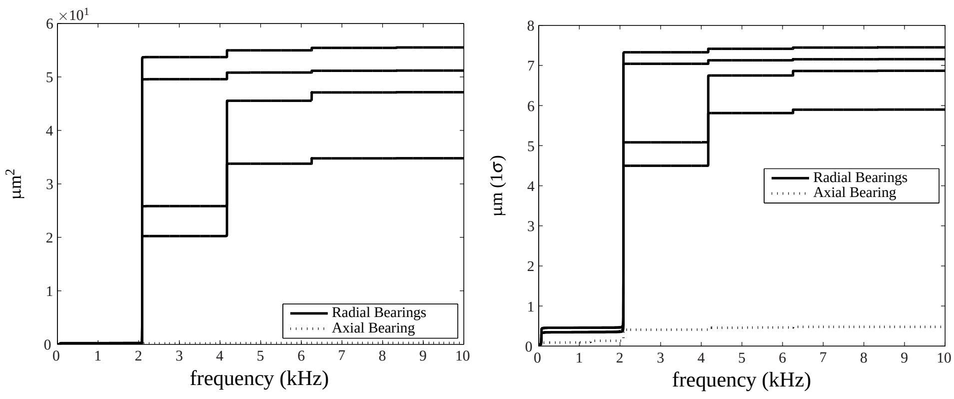

Figure 3.25: The Cumulative Power Spectral Density (CPSD) (left) and the Cumulative Amplitude Spectrum (CAS)(right) of the error signals in the miniature AMB spindle at 125.000 rpm.

3.7 Conclusions and Recommendations

We designed and built a miniature milling spindle with Active Magnetic Bearings. This chapter describes the techniques used for dimensioning the actuators, the modeling and controlling the spindle and actuators, and the realization of the system. Modal PID controllers, combined with negative stiffness compensation and cross feedback, control 5 degrees of freedom of the spindle. A permanent magnet motor drives the spindle to a maximum rotational speed of 150.000 rpm. Experiments showed that an open loop bandwidth of 220 Hz has been achieved and validate the cross feedback control scheme which will be described in Chapter 6. Cumulative Amplitude Spectrum measurements show that a static standard deviation of the error of 38 nm has been achieved. The standard deviation of the spindle error at 125.000 rpm is 7.5 μm. The unrondness of the spindle shaft is expected to be the main contributor to the remaining error, more research is required to verify this hypothesis. This chapter shows the suitability of homopolar, permanent magnet-biased, reluctance type actuators for high speed AMB spindles.

In order to increase the rotational speed to further optimize the cutting conditions, a spindle with a smaller diameter must be built. The reduction of the spindle length will allow for the increase of the rotational speed while remaining below the flexible resonances of the rotor shaft. In order to reduce the measured spindle runout, an investigation into the measurement of the spindle position is required. This investigation is described in Chapter 7.

Chapter 4

Design of a High Speed Tool Holder

4.1 Introduction

A tool holder forms the connection between the spindle shaft and the cutting tool. This chapter describes the design, modelling, realization and testing of a novel tool clamping system. In Chapter 3 the realization of a miniature AMB milling spindle is described. In order to investigate the spindle under cutting conditions, a cutting tool needs to be attached to the spindle rotor. Current state of the art tool clamping systems are not suitable for this application for two main reasons.

Firstly, the mass of commercially available tool holders is very large with respect to the miniature AMB spindle. The motivation for downsizing the miniature AMB spindle has been given in Chapters 1 and 3. The mass we can add to the spindle by attaching the tool holder is very limited.

Secondly, current state of the art tool clamping systems are not able to withstand ultra high rotational speeds. The effect of high speed rotation, and especially centrifugal stresses, on a rotating system has been addressed in Chapter 3. Tool clamping systems are even more sensitive to this because they are often composed out of several components or need to be flexible in order to mount a cutting tool. Current commercially available tool clamping systems tend to lose clamping force at very high rotational speeds due to the centrifugal forces.

In order to address these issues, a novel tool clamping system has been realized. The need for an investigation into novel tool clamping technologies has been formulated by Chae et al. [3], mainly with regard to the runout which is presently introduced by the available tool clamping systems.

4.2 Background

A toolholder generally consists of two connections, one with the spindle shaft and one with the milling tool. In conventional tool clamping systems for macro milling, relatively large tool holders are mounted on the spindle shaft using a steep taper, or a HSK (Hohl Shaft Kegel, german) connection. The clamping force in a HSK tool clamping system increases with increasing rotational speed. Small collets inside the tool holder move outwards due to the centrifugal forces, clamping the spindle from the inside.

The milling tool can be mounted in the tool holder in various ways [53]. The most common way of mounting a cutting tool is using a collet. A collet consists of a slotted sleeve of which the outside is tapered and the inside is cylindrical. The tool is inserted in the collet, and the collet is inserted into a tapered sleeve. A tightening nut presses the collet in the tapered sleeve, clamping the tool. Collet tool holders are known to introduce considerable runout in the system [54], high precision collets have an initial runout of 5 μm which increases with rotational speed. Collet type tool holders loose clamping force with increasing rotational speed. As the tightening nut expands, clamping force is lost. Small milling spindles often use a collet connection directly on the spindle shaft in stead of a separate toolholder

The traditional way of mounting a cutting tool using a side lock screw is still used in present day machining operations. These tool holders are mainly used in applications where runout tolerances are not very critical. The screw type tool holders are able to exert a very high clamping force, compared to other types of tool holders. Tool holders of this type loose clamping force as the rotational speed increases.

Shrink fit tool holders are an upcoming technology in machining industry. A shrink fit connection between shaft and tool is made by passing an electromagnetic field through the tool holder. As the tool holder heats up, it expands and a tool can be inserted. A shrink fit connection introduces very low runout in the spindle shaft combination, and is therefore preferable over collet type tool holders. Currently, shrink fit toolholders are used in applications with high rotational speeds. Furthermore, the mounting of a tool using a shrink fit connection requires the use of expensive heating and cooling machinery. Also in heat shrink toolholding, the tool holder will expand due to the centrifugal stresses, and thus the clamping force is reduced with increasing rotational speed.

In a hydraulic tool holder, the tool is mounted in a sleeve in the tool holder. Hydraulic pressure is applied in a chamber around this sleeve, pushing the sleeve inwards and clamping the milling tool. Because the pressure is applied all around the tool holder, the tool is properly centered. The oil pressure is applied by adjusting a piston in the tool holder. Advantages of hydraulic toolholders are the high accuracy and high clamping force, a disadvantage is the high complexity [54].

The Schunk Tribos tool holder is an elastic deformable structure [55]. The tool is mounted in the tool holders using a polygonal clamping technology. The working principle of the Schunk Tribos tool holder is illustrated in Figure 4.1. During mounting of the tool, the tool holder is deformed enabling the insertion of the tool. When the structure is released the tool is clamped into the tool holder. The Schunk Tribos toolholding system for small end mills, is designed for rotational speeds up to 60.000 rpm, and has even been tested up to 205.000 rpm. The claimed runout in the Schunk Tribos toolholder is below 3 μm .

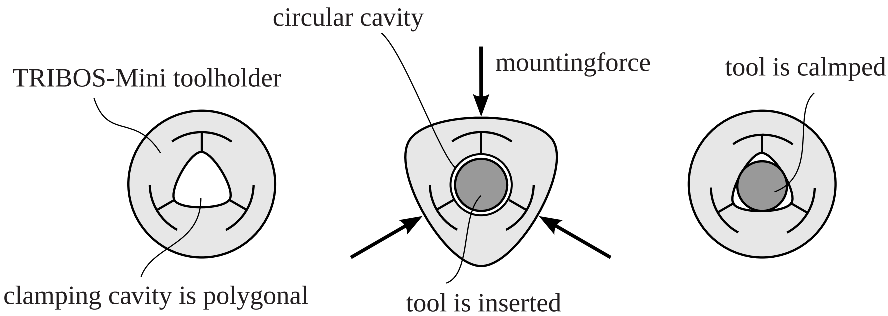

Figure 4.1: The clamping method of the Schunk Tribos tool holder.

All presented tool clamping systems have in common that they loose clamping force with increasing rotational speed. A connection where the clamping force increases due to the high speed rotation, such as the HSK connection is highly desirable. Toolholder types have been classified by Rivin [54] into solid state toolholders and toolholders which are comprised from multiple components. The latter are generally large and are more sensitive to uneven displacements, uneven force distributions, unbalance, and failure. Therefore, in our application we would like to use a monolithic structure for the tool holder.

Several patents have been filed with designs to reduce the loss of clamping force during high speed rotation in the commercially available tool clamping systems.

A novel way of clamping a cutting tool is patented by Haimer [56]. Figure 4.2 shows the cross section of the design proposed by Haimer. Haimer states that the holding torque in the Schunk Tribos tool holder is limited because the tool is clamped using line contacts. Figure 4.2 shows three separate cylindrical clamping surfaces for the tool in Haimers design, increasing the clamping surface.

The three clamping surfaces are connected by spokes to an outer rim, as illus-

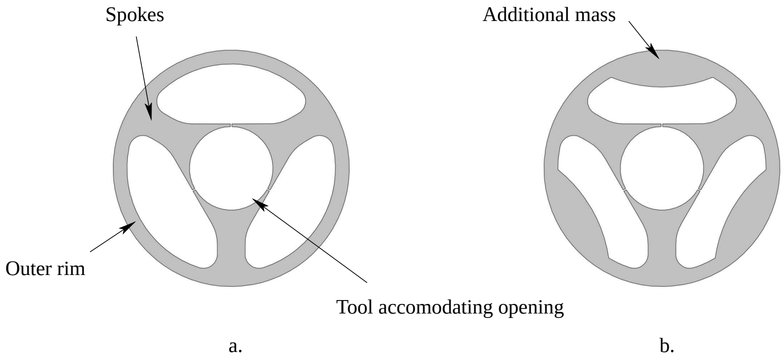

Figure 4.2: Figure a. illustrating the tool clamping system proposed by Haimer [56]. Figure b. shows the tool holder with additional mass to compensate loss of clamping due to centrifugal forces.

trated in Figure 4.2a. The three spokes are subjected to an outwards directed tensile force when the tool holder is subjected to a compressive load. The three cylindrical clamping surfaces expand radially outwards, allowing for the tool to be mounted. When the tool holder is subjected to centrifugal forces the spokes move outwards, eventually causing loss of clamping force. This effect can be reduced by adding mass to the outer rim connecting the spokes, the centrifugal force acting on these masses create a compressive force on the spokes.

An alternative method to clamp a milling or drilling tool for very high rotational speeds is presented by Tempest [57]. In the tool holder presented by Tempest, the tool is clamped by a combination of sprag forces and centrifugal forces. Figure 4.3 shows an illustration of the tool holder presented by Tempest. As illustrated in figure 4.3, the tool holder consists of an outer rim, to which three jaws are connected by hinges. The three jaws allow for mounting in the center of the sleeve, due to their cylindrical inner shape.

The three jaws move outwards as a result of the centrifugal forces, and pivot around the hinges. Due to the pivoting of the jaws, one edge of the cylindrical inner shape of the jaw, edge 1 in Figure 4.3, is pushed against the milling tool. This has two consequences, the grip on the tool is tightened due to the pushing of the jaw and it introduces a sprag effect between edge 1 and the tool. The sprag effect is comparable to the wedging effect. The jaws firmly grip the cutting tool like in a sprag clutch, creating both a clamping force and a high holding torque.

When the jaws pivot under the influence of the centrifugal forces, edge 2 in Figure 4.3 releases from the tool, and the tool is clamped on three line contacts. A spragging force can become very large, resulting in deformation of the tool holder or the tool. Due to the spragging effect, the exact position of the clamped cylinder can

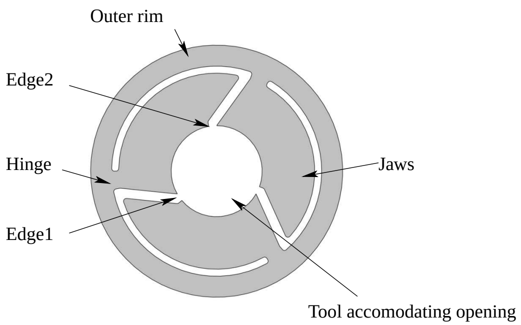

Figure 4.3: Tempest tool clamping system.

be uncertain. After spragging has occurred in this type of tool holder, special means can be necessary in order to remove the cutting tool. Often a high torque is required to release the jaws from the tool. Furthermore, the stiffness of the outer rim reduces the clamping force as the pivot points themselves move radially outward under a centrifugal load.

4.3 Specifications

In this section we formulate specifications for the tool clamping system for the miniature AMB spindle. The two main specifications regard sufficient clamping force in the entire speed range of the miniature AMB spindle, and the maximum runout introduced to the system by the tool holder.

The tool clamping system has to function at an operating speed of at least 150.000 rpm which is the maximum rotational speed of the developed miniature AMB spindle. The desired rotational speeds for micro milling are even higher, in the order of 500.000 rpm, and tool clamping should function reliable at these speeds as well in the future.

The runout introduced by the spindle-tool holder-tool connection must be kept to a minimum. This runout can be caused by a mass unbalance in the toolholder itself, or by a misalignment of tool, tool holder, and spindle axis. Several researchers have investigated tool runout, and the effects of different type of tool holders [3]. For example, set-screw type tool holders introduce more runout than collet type tool clamping devices due to their non-rotation symmetric design, and thus require dynamic balancing. The lowest runout is currently achieved with heat shrink tool holders [53], and is in the order of 2 μm. The micro tools themselves suffer from geometrical runout, that is the difference between geometrical center of the tool and the cutting edges. Currently, the achievable tolerance on the geometrical runout on micro cutting tools is in the order of 5 μm. We aim to keep the runout of the tool holder alone, due to mass unbalance and eccentricity, below 2 μm.

The tool holder must provide sufficient clamping force to hold the milling tool. During the micro milling process, the tool-tool holder combination experiences a braking torque. The braking torque is distinguished into a braking torque from the milling process, and a braking torque caused by airdrag acting on the tool-tool holder combination.

This braking torque exerted by the milling process is derived from the tangential component of the cutting forces, predicted by Dow et al. [8]. The tangential part of the cutting forces is simulated for slot milling with a 0.5 mm cutting tool in tool steel with a feed per tooth of 10 μm and a depth of cut of also 10 μm. The maximum tangential cutting force under these conditions is 1.4 N, which results in a required holding torque of $3.5 \cdot 10^{-4}$Nm.

A method to determine the air drag on a rotating spindle is described by Zwyssig [58]. This method has been used to estimate the braking torque created by the airdrag acting on the tool-tool holder combination. For this approximation, the tool holder is assumed to be a smooth cylinder, rotating at 150.000 rpm. According to the model from Zwyssig [58], this would result in a torque created by the airdrag of 1e-4 Nm. Thus a total clamping torque of $4.5 \cdot 10^{-4}$Nm, 0.45 Nmm is required at 150.000 rpm. Including a safety factor, we specify a clamping torque of 1 Nmm at 150.000 rpm. An overview of the toolholder specifications is given in Table 4.1.

Table 4.1: Toolholder specifications.

Rotational speed	150.000	rpm
Clamping force at 0 rpm	>0	Nmm
Clamping force at operating speed	1	Nmm
Added runout	2	μm

4.4 Novel Tool Holder Design

This section describes the design of the novel tool holder. The first design choice is to machine the spindle end such that is has the same diameter as common micro milling tools, namely 6 mm. The tool holder is then designed as a sleeve, connecting the tool holder and the spindle. The tool holder can thus be prismatic, i.e. have a uniform cross-section. This basic concept is illustrated in figure 4.4.

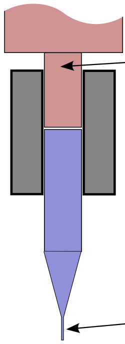

Figure 4.4: Basic tool clamping concept.

Theoretically only 6, well chosen, point contacts are required to have a statically determined support of a rigid cylinder. On the other hand, full cylindrical contact is common in milling, e.g. in a shrink fit connection. In this research we choose to support the cylinders with three line contacts as a result of the trade off between a statically determined connection and sufficient contact surface to ensure proper clamping. By designing a rotational symmetric and monolithic tool holder, runout can be kept to a minimum.

One goal in the design of the tool holder is to maintain, and preferably increase its clamping force at high rotational speeds. Therefore, tool holder design uses the fast rotating mass as an advantage. The basic concept is to transfer an outward directed centrifugal force into an inward directed clamping force.

This is done by carefully placing the mass of the tool holder, and thus the position where the gross part of the centrifugal force acts. A properly designed linkage transfers this force to an inward directed clamping force at the line contacts between the tool holder and the shaft.

Figure 4.5 shows a top view of the novel toolholder and a schematic view of one of the six linkages between the contact lines and the masses of the tool holder. Point B indicates the contact lines between the tool holder and the tool, the mass is located at point A. The centrifugal force thus acts in point A and is indicated by F_{cf}

When using a rotating coordinate system, and assuming constant rotational speed, the tool holder will reach a static equilibrium. The dashed lines in Figure 4.5 are planes of symmetry. The centrifugal force acts on A, and results in a counter clockwise rotation of point C. Point B is therefore pushed inward, resulting in a clamping force. The system is assumed to be linear elastic. Thus, a fixed and linear relation R exists between the centrifugal force and the radial clamping force (R =

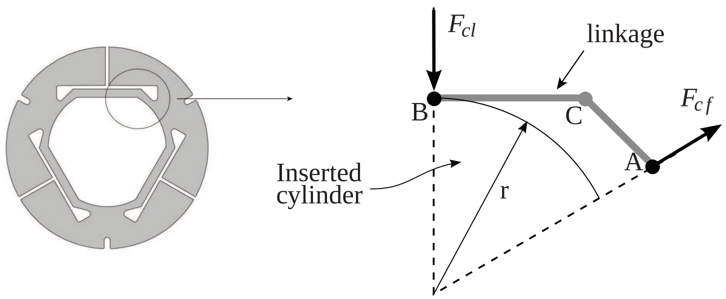

Figure 4.5: Top view of the novel toolholder including a schematic representation of one sixth of the tool holder, showing the contact line (B), the linkage (C), and the tool holder mass (A). The dashed lines indicate the symmetry axis.

F_{cf}/F_{cl}). In conclusion, the centrifugal force and the clamping force both increase quadratically with rotational speed under the mentioned assumptions.

The placement of the masses (point A) is bounded from below by the tool radius (r). The upper limit is the location of A where BCA becomes a line. The inside of the toolholder is in that case a triangle which becomes larger upon rotation. Analytical calculations proved that the clamping force is maximal if the masses are located as close to the inserted cylinder as possible.

At zero rotational speed, the clamping force is determined by the slightly larger diameter of the cylinder (tool or spindle shaft) with respect to the tool holder cavity.

The six links together define the inside geometry of the tool holder. The outside geometry of the tool holder is designed cylindrically to minimize the air drag at high rotational speed. The masses are connected to the inner ring and are shaped as circular segments on the outside. The outside diameter is chosen identical to the rotor diameter, 12 mm. This provides sufficient mass to have good clamping behavior. The height of the tool holder is 15 mm, resulting in two times 7.5 mm potential engagement length. The contact lines are interrupted by the slots visible in the left image in Figure 4.6. These slots decouple the clamping lines from the two cylinders, reducing the influence of diameter differences on the clamping forces.

The material yield stress poses a fundamental limit on the outer radius of the tool holder. In a solid ring, rotating at 300.000 rpm, a yield strength of 1000 MPa will be exceeded when the radius is larger than 18 mm, resulting in catastrophic failure. The new tool holder design has a much lower upper bound for the outer radius, because the tool holder is not a solid disc, but a flexure mechanism. Furthermore, a considerable safety factor should be applied to this maximum diameter to account for e.g. inhomogeneities in the tool holder material. The maximum stresses in the tool holder are investigated using Finite Element Method (FEM) Modeling. Figure 4.6 illustrates a cross sectional view of the final design of the tool holder and the manufactured tool holder.

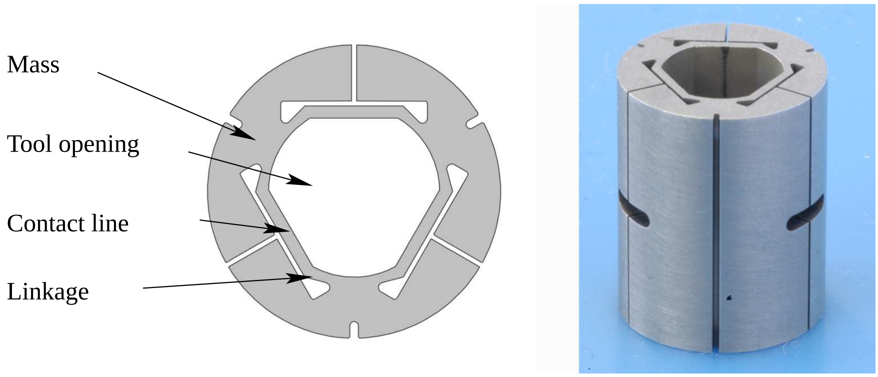

Figure 4.6: Top view of the final tool holder design, and image of the manufactured tool holder. Photos courtesy of Philip Broos / Leiden, MicroMegazine.

4.4.1 Mounting of the Micro End Mill

To mount the tool, inward forces have to be applied to relax the tool holder. To apply these forces at the right positions on the circumference of the tool holder, a mounting tool has been developed. This tool enables the forces to be applied exactly on the centrifugal masses. The tool holder fits in the mounter in only one way its rotation is prevented by the three ridges. The mounting tool is illustrated in figure 4.7. The mounting tool has a triangular inner shape. One of the three triangle edges is suspended in a flexure mechanism. When moving this edge inwards, three inwards directed forces are applied to the tool holder at exactly 120 degrees, with equal magnitudes. The flexure is moved inwards simply using a bolt.

4.5 FEM Analysis

This section describes the Finite Element Method (FEM) modeling of the proposed tool holder. The FE analysis shows the working principle of the tool holder, and allows for its dimensioning. We are mainly interested in the initial clamping force and the increase in clamping force with increasing rotational speed. The clamping force is determined by first determining the stiffness of the legs of the triangle. With the stiffness of the legs known, the influence of e.g. manufacturing tolerances on the

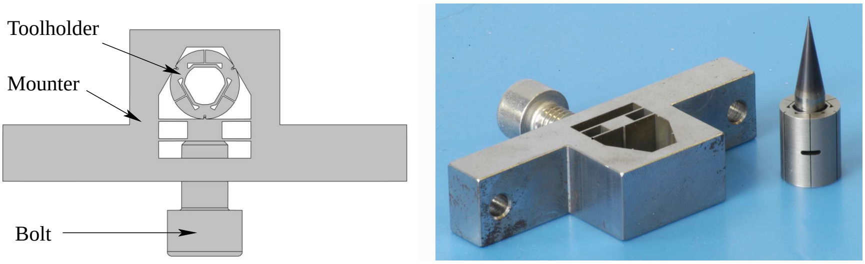

Figure 4.7: Top view of the mounting tool design, and image of the manufactured mounting tool. Photos courtesy of Philip Broos / Leiden, MicroMegazine.

clamping force is easily determined. The simulations are performed using ANSYS FEM software.

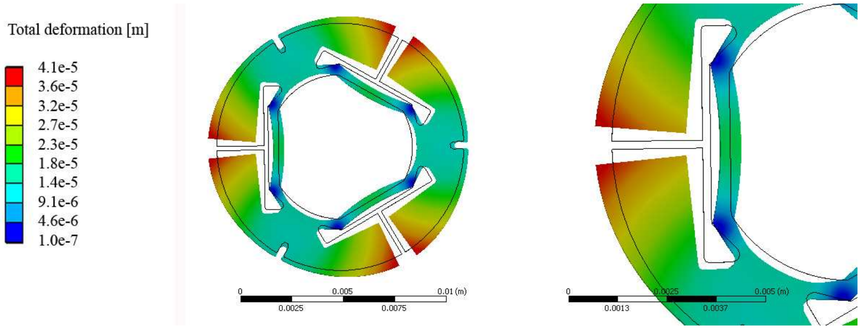

Figure 4.8: FEM analysis of the tool holder rotating at 150.000 rpm, showing its deformation.

4.5.1 Leg Stiffness

A force has been applied to the legs of the triangle to determine their stiffness. The average displacement at the clamping contact line is $6.5{\cdot}10^{-5}$m when a force of 1000 N is applied. This combination results is a leg stiffness of $1.5{\cdot}10^{7}$ N/m.

4.5.2 Clamping Force at Standstill

The clamping force at standstill is determined by size difference between the tool holder and the clamped shaft. We will refer to this overlap, or negative clearance between the shaft and the toolholder as the interference. At standstill, the clamping force is at its lowest and will only increase with rotational speed. Theoretically, the clamping force at zero rotational speed does not need to be very high and will only have to hold the weight of the tool and the tool holder. In theory the initial clamping force can be such, that the tool can be mounted by hand and still deliver sufficient clamping force at its operating speed. In practice, the clamping force is highly determined by the manufacturing tolerances. Its exact magnitude is only known after accurate measuring of the inner triangle and the clamped shafts. The interferences mentioned here are worst case interferences considering manufacturing tolerances, thus resulting in the lowest initial clamping forces.

The holding torque is determined by first determining the normal force on one line contact, from this normal force the tangential friction force is determined with the friction coefficient. The tangential force and the tool shaft radius result in a holding torque. Because we have three line contacts, the total holding torque is three times the torque of one line contact. The value for the friction coefficient is very uncertain, and highly dependent on contaminations on the surfaces. The value for the friction coefficient will be further discussed in section 4.7.

Two tool holders have been manufactured. One with an interference of 5 μm with the tool on the radius, and one with an interference of 10 μm. The 5 μm interference tool holder would theoretically result in a total holding torque of 170 Nmm. The holding torque for the 10 μm interference tool holder will obviously be 340 Nmm, assuming a friction coefficient of 0.25.

The manufacturing tolerance of a cutting tool shaft is 2 μm on the radius. Considering the tool holder manufacturing tolerances, there is an uncertainty of 4 μm in the overlap, corresponding to a holding torque of 135 Nmm. The values for the calculated holding torque are all well above the specification of 1 Nmm.

4.5.3 Clamping Force when Rotating

Figure 4.8 shows the deformation of the tool holder when rotating at 150.000 rpm, clearly illustrating the working principle of the tool holder. Figure 4.8 shows that the edges of the triangle move inwards with rotational speed, thus increasing the clamping force. The holding torque is determined in a similar way as in the previous section. The inward deformation of the triangle leg is 16.5 μm. In combination with the leg stiffness of $1.5 \cdot 10^7$ N/m, this results in a normal force of 250 N. This gives an additional holding torque due to the rotation of 560 Nmm, assuming a friction coefficient of 0.25.

4.5.4 Mounting

As mentioned in section 4.4, the tool can be mounted by applying forces on the three edges of the triangle. Figure 4.9 shows the deformation of the tool holder when 1000 N is applied to each corner of the triangle. The legs of the triangle move outwards, enabling the mounting of the tool holder on the rotor shaft, and the insertion of the cutting tool.

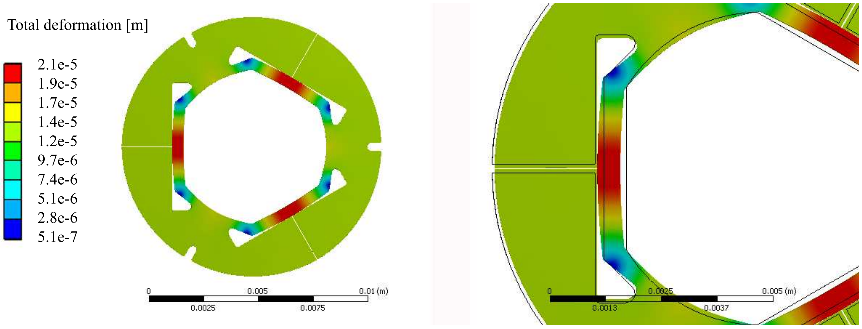

Figure 4.9: FEM analysis of the tool holder during mounting of the tool, 1000 N is applied to the three edges of the triangle.

4.5.5 Stresses

The tool holder is a monolithic flexible structure with relatively large deformations. Therefore it is of utmost importance to use high strength tool steel, and to observe that the yield strength is not exceeded. The stresses in the tool holder are studied under various conditions with a FEM analysis. The largest stresses occur at high operating speeds, and during mounting of the milling tool. The danger exists in exceeding the yield strength when mounting the tool. An improvement of the design of the tool mounting device can avoid this.

Small local plastic deformations due to high stresses at high rotational speeds result in a slightly lower initial clamping force at zero rotational speed.

4.5.6 Contact Mechanics

The interface between the inserted cylinders and the inner cavity of the tool holder can be described using a Hertzian contact model. A cylindrical body is pressed on a flat body, resulting in a rectangular contact area, assuming a contact force of 200 N. According to the Hertzian model the contact width is 40 μm and the indentation depth is 0.08 μm. This depth is not large enough to have a significant effect on the clamping behavior. The stresses predicted by the Hertzian model are well below the yield strength (500 MPa) and suggest that there will be very limited geometrical wear at the contact interfaces during normal operation.

4.5.7 Diameter Differences of the Clamped Cylinders

The line contacts in the proposed toolholder are interrupted where the two clamped cylinders meet, as mentioned in section 4.4. However, the tool holder has rigid centrifugal masses over the entire length of the tool holder. Therefore, the coupling between the clamping force on the top and bottom cylinders has been investigated. The influence of a difference in the clamped cylinder diameters on the clamping force has been investigated using FEM.

The FEM results have shown that the clamping force drops linearly with the cylinder diameter, similarly to the situation with no diameter difference. A decoupled design by separating the centrifugal masses for the upper and lower clamping half, did not significantly improve the clamping behavior.

Therefore we conclude that the top and bottom halves of the tool holder are decoupled, and that the tool holder is thus insensitive to small differences (< 4 μm) between tool and spindle diameter.

4.6 Fabrication

Two tool holders have been manufactured from AISI 630 Quenched and hardened steel. The material is subjected to a process of precipitation hardening. The resulting yield strength is well above 1000 MPa, one of the highest available. The tool holders have been machined by wire EDM (Electrical Discharge Machining). The accuracy of the EDM process is in the range of 1 to 2 μm. The inner contact surfaces are machined in several runs to achieve the highest accuracy and the lowest roughness.

4.7 Experimental Work

This section describes the experimental investigation into the clamping characteristics of the tool holder. In this section the relation between a load on the tool holder masses and the clamping force is investigated under static, non rotating conditions.

4.7.1 Methods and Materials

A static approach has been chosen in order to have controllable experimental conditions. Under non-rotating conditions the clamping force can be measured using a torque test bench and a load cell. The static conditions enable accurate investigation of the influence of wear on the tool holder, the reproducibility, and the presence of deformations.

When performing these experiments under static conditions in stead of rotating, we have to consider the following:

- We assume that the centrifugal load acts mainly on the three masses on the triangle corners. The contribution of the centrifugal forces acting on the triangle edges are neglected. This is valid because the centrifugal masses are much larger than the masses of the linkages, and are located at a larger radius.

- We do not take into account any dynamics. The behavior of the tool holder when passing critical speeds is not studied, nor is the influence of the additional tool holder-tool connection on the flexibility of the spindle.

Characterization of the clamping behavior during rotation of the tool holder is part of future work.

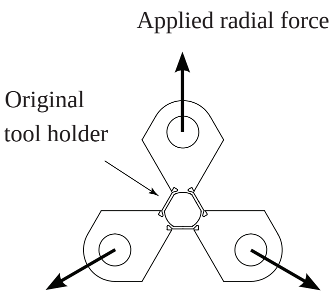

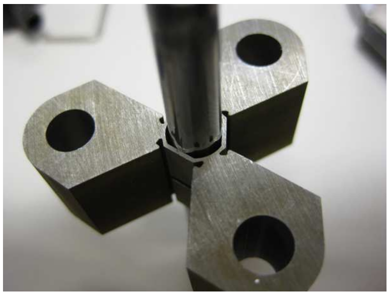

Figure 4.10: Top view of the design of the dummy tool holder for the static clamping test, and the manufactured dummy tool holder with tool shafts inserted.

To enable the application of forces on the centrifugal masses, a special version of the tool holder has been designed. Figure 4.10 shows the design of this dummy tool holder as well as the manufactured dummy tool holder with two tool shafts inserted.

The tool holder is radially loaded using the test setup illustrated in figure 4.11. This test setup is mounted in the torque test bench. The torque test bench used is a Zwick/Roell Z005, equipped with a HBM T20WN torque load cell. This load cell has a maximum load of 500 Nmm, and an accuracy of 0.2 %.

In this experiment the tool holder is radially loaded with forces ranging from 100 N to 2000 N, limited by the range of the torque load cell. The top cylinder follows a prescribed angular motion while measuring the applied torque. The torque at which the tool starts to slip is taken as a measure for the clamping force. This is allowed because the radial clamping force and the tangential friction force are linearly related by the friction coefficient.

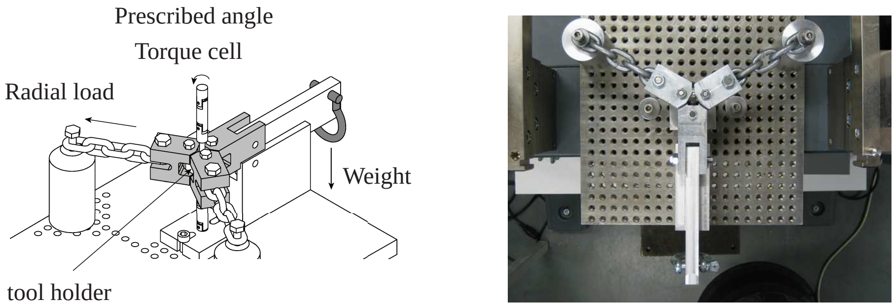

Figure 4.11: Schematic view of the test setup used to apply radial loads on the dummy tool holder and a picture of the realized setup.

The experiment has been performed with two tool holder dimensions, one with an interference on the radius of 5 μm and one with an interference of 10 μm. For each radial load on the tool holder, this measurement has been performed three times to investigate the reproducibility. The reproducibility can give an indication of the presence of wear or plastic deformations of the tool holder.

4.7.2 Experimental Results

The results of the three repetitive measurements for the 5 μm interference tool holder under a load of 1400 N is shown in Figure 4.12. In this figure we see the initial loading to overcome the flexibility of the setup until the tool tool holder connection starts to slip.

Figure 4.12 shows a clear difference between the torque characteristic in the first experiment and the following experiments. The stick slip behavior is less pronounced in the first experiment. The measurements showed similar responses for two different tool holders under different loads.

To investigate the relation between the radial load on the tool holder and the clamping force, the experiment from Figure 4.12 has been repeated for different loads. From each set of three measurements, the average maximum torque (stick torque) and the average final dynamic torque (slip torque) have been determined. These measurements have been performed for the 5 μm interference and the 10 μm interference tool holder to investigate the difference in initial clamping behavior and to see whether this difference is maintained under increasing radial load. The results of these experiments are presented in Figure 4.13.

From Figure 4.13 we can conclude that the maximum slip torque, and thus the clamping force when assuming a constant friction coefficient, increases with the applied radial load. This increase can be linearly approximated, also shown in Figure 4.13. This linear relationship is as expected, see Section 4.4. Note that the radial

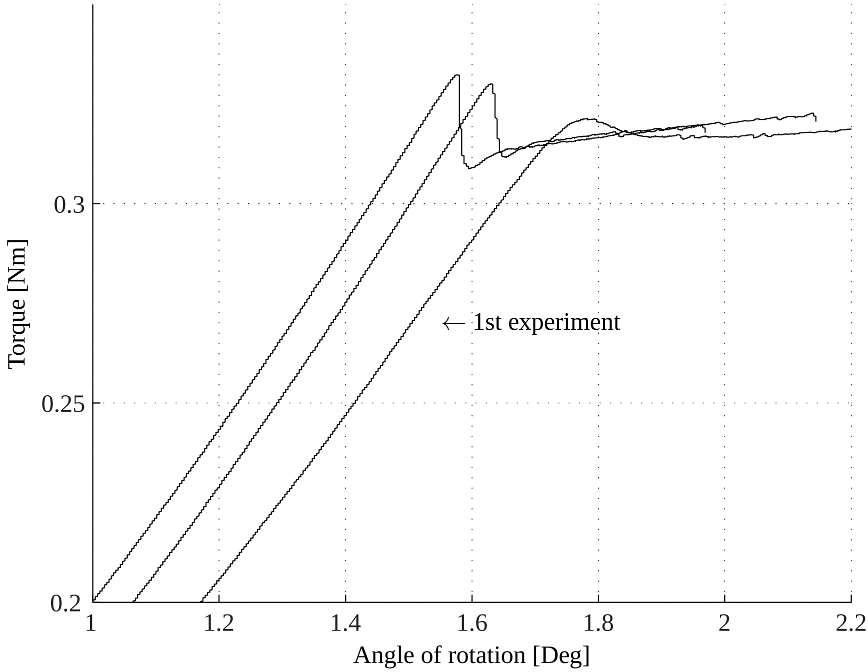

Figure 4.12: Three measurements of the torque angular displacement relation of the 5 μm interference toolholder under a radial load of 1400 N.

load, and thus the clamping force, will increase quadratically with rotational speed. A radial load of 2000 N corresponds to a rotational speed of 130.000 rpm of the original tool holder.

This linear relation and the reproducibility of the experiments indicate that no plastic deformation occurs in the tool holder. Furthermore, the clamping surfaces seem not to suffer from severe wear, which would reduce the clamping force.

In Figure 4.13 we can see that the relations between the radial force and the holding torque, for the two different tool holders, 5 μm interference and the 10 μm interference, are nearly parallel.

As mentioned in Section 4.5, the value for the friction coefficient between the two surfaces is highly uncertain. This value can differ between 0.1 and 0.8 depending on the surface quality and contaminations of the surface.

The relative interference of the two tool holders is assumed to be quite accurate, since they are manufactured on the same machine. From the difference in holding torque of the two tool holders, the friction coefficient can be determined. To do this, the leg stiffness determined by FEM from section 4.5 has been used. This results in a friction coefficient of 0.25.

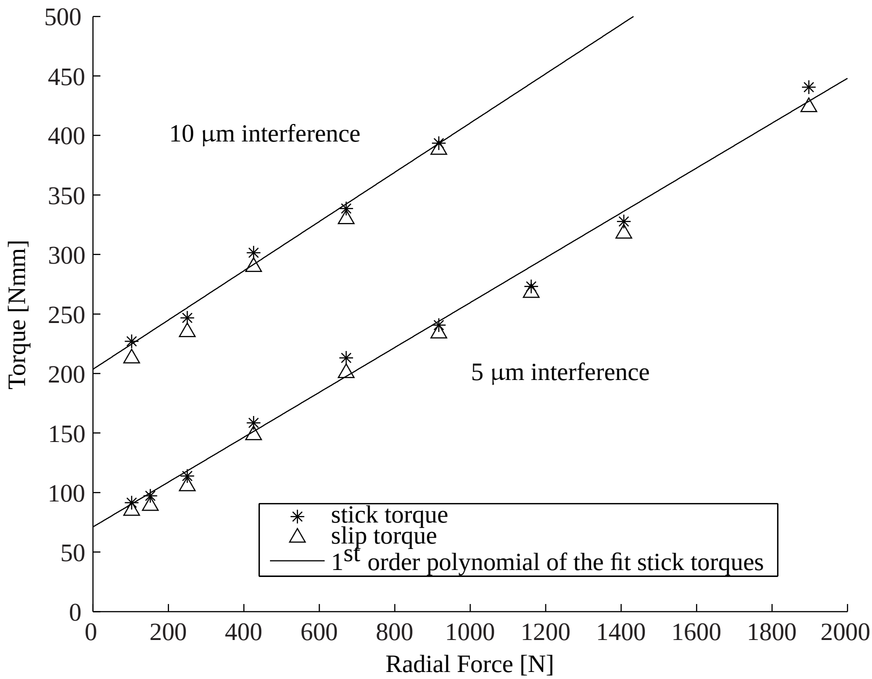

Figure 4.13: The dependency of the holding torque on the radial force applied to the toolholder.

The clamping forces at standstill are predicted in Section 4.5, and are respectively 170 Nmm and 340 Nmm for the 5 μm interference and the 10 μm interference tool holder. These differences can possibly be explained by a few causes. The EDM process has a typical surface roughness (R_a) of 2 μm. During the slip of the tool in the tool holder, the roughness peaks can be flattened. Furthermore small local plastic deformations in the flexible structure of the tool holder can reduce the initial clamping force. Finally, the lower initial clamping force can be a result of exceeded manufacturing tolerances.

From these experiments we can conclude that the clamping force is wel above the specified holding torque of 1 Nmm at 150.000 rpm.

4.8 Influence of Tool Toolholder Combination on the Spindle Dynamics

In the design of the miniature AMB spindle, until now, only the flexural resonances of the rotor without a tool and toolholder have been considered. Figure 4.14 shows

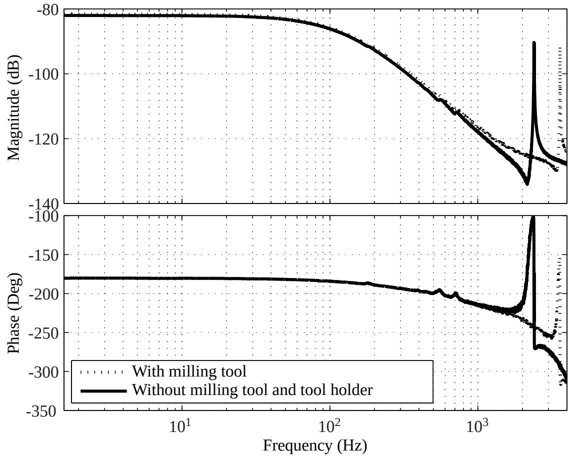

Figure 4.14: Plant frequency response of the top radial bearing, rotor displacement over input current (y/u), showing the effect of the tool toolholder combination on the first flexural resonance frequency.

the frequency response functions of the top radial bearing in x-direction with and without a micro end mill. Figure 4.14 shows that the first flexural resonance frequency is lowered from 3.6 kHz to 2.4 kHz. Although the effort has been made to keep the added mass en length of the tool toolholder combination as low as possible, its influence is considerable. A first flexural resonance of 2.4 kHz corresponds to two critical speeds around 144.000 rpm.

4.9 Milling Experiment

The tool holder has been successfully tested in a micro milling experiment. The toolholder was able to properly clamp a milling tool at 80.000 rpm, and was able to deal with the micromilling conditions. This experiment is described in Chapter 5.

4.10 Conclusions and Recommendations

A novel tool holder has been designed and built for micro milling with rotational speeds up to 150.000 rpm. This chapter described the design of the tool holder, as well as experimental verification of the working principle. The tool holder is a one piece, monolithic sleeve, which holds the spindle end as well as the micro milling tool. The tool holder is designed such that the clamping force increases with increasing rotational speed. A finite element analysis is presented to theoretically investigate the performance of the tool holder.

A static test shows the increasing clamping force with an increasing load on the tool holder. The clamping force increases linear with increasing loading force. The influence of wear on the clamping force is neglectable. The tool holder is successfully tested in a micro milling experiment, this will be described in Chaper 5.

Future work includes the dynamic testing of the tool holder. The increase of the clamping force has to be measured under dynamic conditions to fully identify the behavior of the proposed tool holder at high rotational speeds. Furthermore, more micro milling experiments with the tool holder have to be performed to investigate its performance under different cutting conditions over an elongated period.

Chapter 5

Design of a Micro Milling Setup

5.1 Introduction

This chapter describes the design and realization of a miniature micro milling setup. The goal of this setup is to investigate the miniature AMB spindle designed and realized in Chapter 3 under machining conditions. Furthermore the micro milling setup enables testing of the proposed tool holder in Chapter 4 in a milling experiment.

Machining centers typically consist of a spindle and multiple linear stages, offering three up to five axes of motion of the tooltip with respect to the work piece. The machining center has to position the work piece with respect to the tooltip during milling as well as during μEDM and μECM operations.

One of the goals formulated in the introduction of this thesis is the downsizing of micro milling machinery. Chapter 3 describes the design and realization of a miniature AMB spindle. In this Chapter, the downsizing of the rest of the machine is investigated. In micro milling, the minimum chip thickness effect requires a minimum Feed Per Tooth (FPT), as described in Chapter 1. Therefore high stage velocities and accelerations are required. The lower mass of small machinery enables the increase of velocities and acceleration. A higher control bandwidth can be achieved due to a reduction of moving mass. Furthermore, a reduced moving mass in the work piece positioning stage will enable fast open loop interventions to avoid tool breakage or short circuit in μEDM.

5.2 Specifications

A milling experiment with the miniature AMB spindle requires the machining of work pieces in at least 2.5 dimensions, which is the consecutive build up of 2 dimensional layers. Therefore we need to design and build a machining center with at least three moving axes.

The Feed Per Tooth (FPT) partly determines the quality of the cut during micro milling. The FPT determines the thickness of the chips formed during cutting. In order to form a proper chip, a minimal chip thickness is required [59, 60]. When the chip thickness is much smaller than the cutting edge radius of the tool, a chip is not formed because the work piece is elastically deformed. When the chip thickness is about equal to the cutting edge radius a chip is formed by shearing of the work piece material. In both cases, the quality of the cut is poor and the cutting forces acting on the tooltip are relatively large, causing tool wear and potentially leading to tool breakage. The minimal FPT in the micro milling operations described in this research is 5 μm, and the maximum rotational speed of the miniature AMB spindle is 150.000 rpm. When cutting with a two-flute end-mill, this results in a minimum stage velocity of 25 mm·s^{-1}. We aim to reach this velocity within three spindle rotations when cornering inside the work piece. This minimizes the path where the FPT, and thus the cutting quality, is low. This results in a stage acceleration of 21 m·s^{-2} (2.1 g). Mechanical retraction to avoid short circuits during μEDM requires even higher accelerations, where distances of 10-20 μm must be bridged within 1 ms. This results in accelerations in the order of 40 m·s^{-2},

In the *μfac* project, we aim to reach a total three dimensional work piece accuracy of 0.1 μm (1 σ) after two machining steps or more. We aim to reach micron accuracy in the first, coarse machining step with micro milling. In micro milling, the spindle will operate at high rotational speed and the stage accelerations will be high. The work piece accuracy will then mainly be determined by the spindle run out. In the successive, fine machining steps μEDM and/or μECM, where the final work piece accuracy needs to be achieved, the spindle rotational speed is low, as well as the stage accelerations. Furthermore, in the coarse machining steps, we deal with cutting forces, while in the fine machining steps, no tool-work piece forces are present.

5.3 Conceptual Design

The aim is to design and build a 3-axis machining center. The miniature AMB spindle described in Chapter 3 is designed to be used vertically. The adjustable bias flux in the axial bearing allows for straightforward gravity compensation. The bias flux in the radial bearings is fixed due to the use of permanent magnets and the bearing geometry. Gravity can also be compensated by giving the rotor an off-set position in the magnetic bearings. An off-set position or an increased bearing current will decrease the linearity of the actuator. An offset position of the rotor in the radial bearing would result in an uneven bias flux distribution in the rotor, and would thus increase the rotating losses. For this reason, and to avoid additional non linearities in the radial bearings, the spindle is used vertically. The spindle axis is defined as the z-axis of the milling setup. The spindle is mounted on a linear z-stage.

The work piece is positioned along the remaining two axis, x and y, using a stacked positioning stage. The setup is mounted on a granite base with the vertical stage mounted on a granite bridge. Granite is chosen because it has a low thermal expansion coefficient, high mass, and a high stiffness.

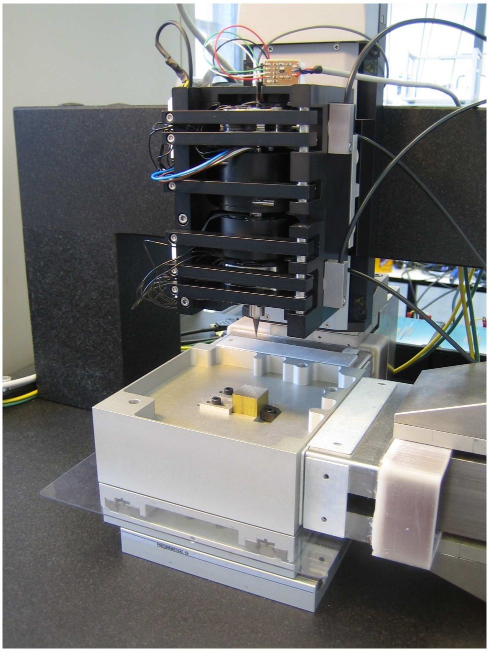

Figure 5.1: Micro milling setup with miniature AMB spindle.

5.4 Z-stage

A commercially available z-stage from Physik Instrumente (PI) positions the spindle in vertical direction, and thus determines the depth of cut. The main requirement for this stage is to maintain a high positioning stability when the cut is made. This stage does not have to meet any velocity or acceleration requirements. The work piece surface is found by making small incremental steps with the z-stage. When the work piece surface is touched, a control effort can be observed in the axial magnetic spindle bearing. Subsequently the cutting depth is set. We specify a stage position accuracy while cutting below 0.1 μm.

The z-stage is spindle driven and uses an optical encoder mounted on the spindle shaft. The encoder has a resolution of 2048 counts per revolution and a gear ratio of 29.6:1. A spindle drive is chosen over, for example, a direct drive, or a linear motor for the possibility to lock the stage when powered down.

5.5 XY positioning stage

The downscaling of the machinery for micro machining is also applied to the xy-positioning platform. By downscaling the positioning stage, we can realize higher accelerations, improving the quality of the cut when cornering inside the work piece. The fast accelerations make it possible to react to unforeseen events like a sudden increase in cutting forces or a short-circuit during μEDM.

For that purpose, a positioning platform from the semiconductor industry is used. This platform consists of two Lorentz actuators and a stacked xy-positioning stage supported by needle bearings. The positioning platform hardware has been made available by NXP/ITEC. The Industrial Technology and Engineering Center (ITEC) is a department of NXP, former Philips Semiconductors. The xy-positioning stage has been designed for the use in the Phicom wire bonding machine.

A platen is designed interfacing the voice coils, the positioning bearings and the work piece. The moving mass is kept as low as possible.

5.5.1 Actuators

Linear current source amplifiers are used to power the voice coil motors. The amplifier design is identical to that of the current source amplifiers for the miniature AMB spindle as described in Chapter 3. For application in the xy-positioning stage, the amplifiers are designed for a maximum output current of 10 A.

5.5.2 Encoder

The xy-positioning stage is equipped with a two dimensional grid encoder from Heidenhain, the PP 271R. The encoder has a grating of 8 μm. The signal period, is 0.4 μm after an interpolation of 10 times. After quadrature, this results in a resolution of 0.1 μm. From this we can conclude that the final position accuracy of 0.1 μm for μEDM and μECM, specified in section 5.2 will already not be reached due to encoder resolution limitations only, regardless of the other uncertainties in the system.

5.5.3 Controller Hardware

The controller hardware is a dSPACE ds1005 modular system. The micro milling setup requires at least 5 analog inputs for the AMB spindle sensors. A DS2004 board is used providing 16 16 bit A/D converters. Eight analog outputs are required for the spindle reluctance actuators and the xy-stage voice coils. Two DS2102 boards provide a total of 12 16 bit D/A converters. One digital input is required for the spindle velocity sensor, only a few digital outputs are needed for simple switching tasks.

Two encoder inputs are used for the xy-stage encoders. The encoder signals are interfaced using a dSPACE DS3002 interface board, providing a total of six encoder inputs. The system runs at a sampling frequency of 20 kHz.

5.5.4 Controller

The moving mass of the stage is 3.2 kg in x-direction and 2.8 kg in y-direction. The required servo stiffness has been approximated in Section 3.2.1 in Chapter 3: $1.4{\cdot}10^5$ N$\cdot$m^{-1}. From this an initial estimation of the required bandwidth can be made, resulting in a target bandwidth of at least 40 Hz.

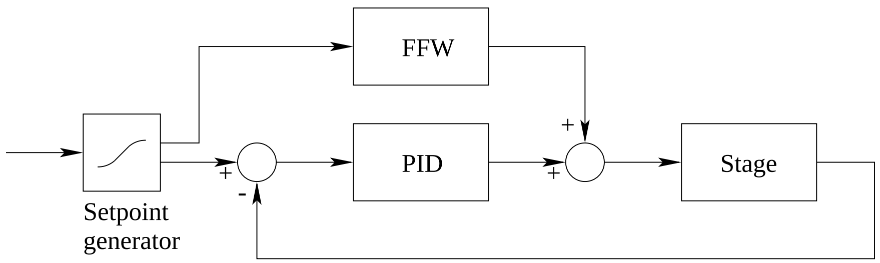

Figure 5.2: Control loop of the XY positioning stage.

The xy-stage is positioned using classical PID controllers. Figure 5.2 illustrates the control principle for one Degree of Freedom (DOF). The PID controllers have been tuned obeying the Ziegler Nichols tuning rules for PID control. The plant frequency response is illustrated on the left in Figure 5.4. In Figure 5.4 we can see that the first higher order dynamics are present at 320 Hz. The system has been tuned to a bandwidth of 130 Hz. The closed loop frequency response is illustrated in figure 5.4.

A feed forward path has been added to the controller to improve the servo performance. A third order set point generator is used to generate the motion profile. The set point generator has been developed by Wesselingh [61]. The stage velocity is given by the desired Feed Per Tooth (FPT) as described in Section 5.2, and is 25

Kp	$1 \cdot 10^6$	[-]
f_i	20	Hz
f_d	100	Hz
N	4	[-]

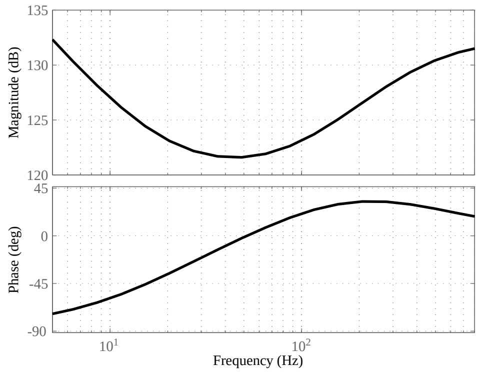

Figure 5.3: The PID controller for the xy positioning stage, the controller settings (left) and the frequency response of the controller only (right)

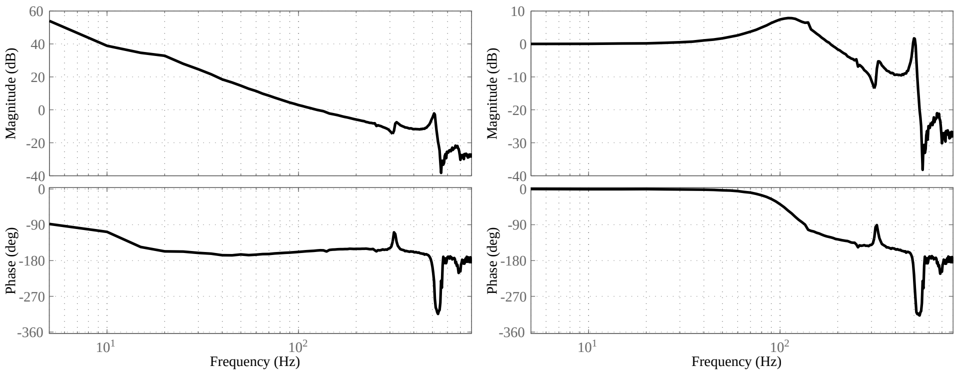

Figure 5.4: Measured open loop frequency response function from error to output, illustrating a bandwidth of 130 Hz (left) and measured closed loop transfer function, from reference to output (right) of the XY stage in X direction.

mm·s^{-1}. The desired acceleration is 21 m·s^{-2} as specified in section 5.2. From this information a suitable motion profile can be generated. The maximum jerk is set at 16000 m·s^{-3}, determined by $dI(dt)^{-1}$, and thus the electrical time constant of the coil, $L(R)^{-1}$, and the maximum amplifier voltage. The tracking error during this motion is shown on the left in Figure 5.5. The desired set point trajectory is also illustrated in Figure 5.5. The error in the orthogonal direction is illustrated in on the right in Figure 5.5.

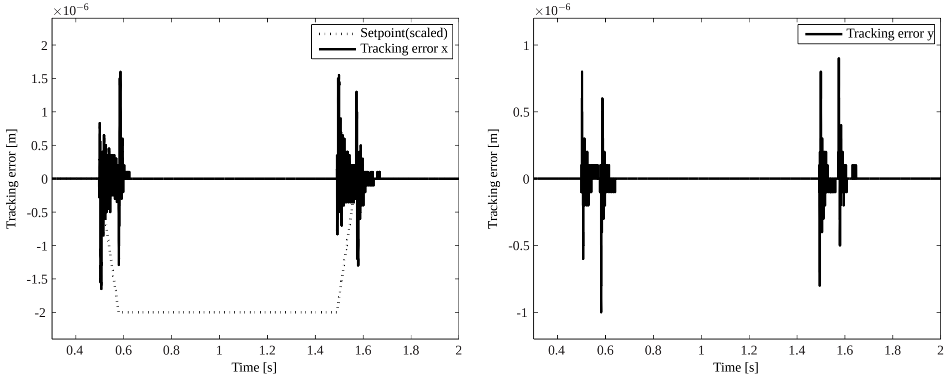

Figure 5.5: Measured stage tracking error in moving direction (left) and the orthogonal direction (right) including the scaled set point trajectory. The stage accelerates to a constant velocity of 25 mm/s, and decelerates to stand still.

The completed milling setup is shown in Figure 5.1.

5.6 Milling Experiment

This section describes the first milling experiment using the miniature milling setup. The goal of this experiment is to investigate whether the miniature AMB spindle and the micro milling setup is able to perform a proper cut. It is beyond the scope of this research, however, to find the optimal cutting conditions and to perform extensive milling experiments.

5.6.1 Cutting Conditions

The milling experiment is performed using a two flute, square end mill. The mill is made out of solid carbide, and has an TiAlN coating. The end mill has a tooltip diameter of 0.2 mm.

In this experiment, we perform slot milling in brass. Brass is chosen for the first experiments because it is a relatively soft material. The tool is connected to the miniature AMB spindle using the novel tool holder described in Chapter 4.

For this experiment, the rotational speed of the spindle is set at 80.000 rpm, which corresponds to 1.3 kHz. This speed is chosen to stay well below the first flexible spindle resonance of 2.4 kHz as described in Chapter 4. With a rotational speed of 1.3 kHz we operate safely above the rigid spindle resonances, 100-300 Hz, as described in section 3.6.4. Considering the above, the velocity of the work piece positioning stage has been set at 50 mm$\cdot$s^{-1}, resulting in a feed per tooth of 20 μm.

The depth of cut is set at 5 µm. There is a maximum depth of cut until which a stable cut is performed for each spindle speed, as illustrated by the so called stability lobe diagram. Therefore a low depth of cut is chosen. The work piece surface is found using the axial active magnetic bearing. The spindle is lowered with increments of one µm while observing the control effort for the axial AMB. When the work piece is touched, a control effort is observed in the axial bearing to maintain the rotor position. The work piece is passed 5 times until a total depth of 25 µm is reached.

5.6.2 Milling Result

Figure 5.6 shows the slot milled in the described experiment. From this experiment, several things can be observed.

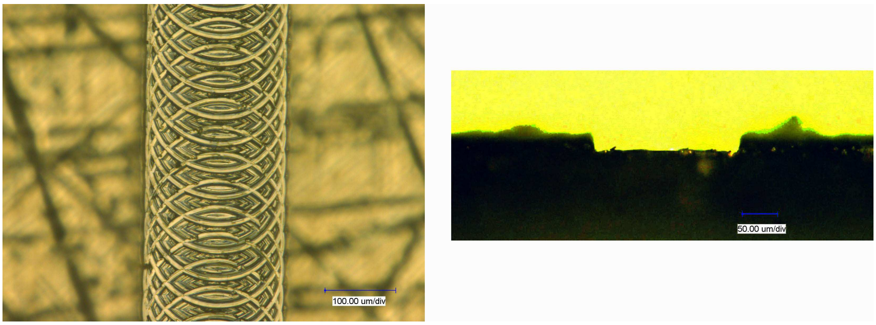

Figure 5.6: First milling result of the miniature machining center during milling in brass with a 0.2 mm end mill, at a rotational speed of 80.000 rpm

Figure 5.6 shows that a stable cut has been performed. The regular pattern indicates that no chatter occurred during this experiment. Figure 5.7 shows that no burrs have been formed in this milling experiment.

The width of the milled slot can give an indication of the run out at the tooltip position. From the cumulative amplitude spectrum in Figure 3.25 from Chapter 3 a run out in the lower radial bearings of at least 5 µm is to be expected, without taking into account the geometrical run out of the cutting tool, and the run out introduced by the tool holder.

The left image in Figure 5.7 shows the milled slot, with the top work piece surface in focus. The width of this slot is 207 µm, as illustrated in figure 5.7. When considering the width of the milled slot, we may expect a run out of cutting tool tip in the order of 7 µm. SEM (Scanning Electron Microscopy) inspection of the milling tool shows that on of the two cutting edges has been lost in the milling process. This has to be considered when observing the width of the slot. More experiments need to be performed to determine the exact run out at the tooltip.

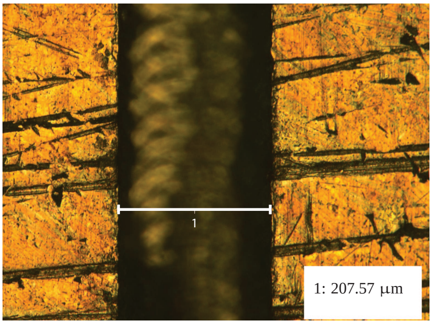

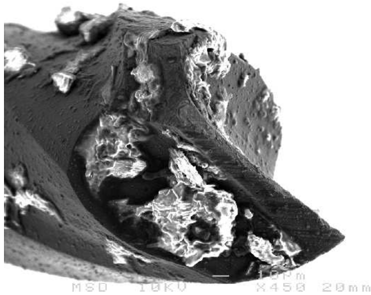

Figure 5.7: The milled slot, focus on work piece surface (Left) and SEM picture of the used micro end mill (right)

There are several possible explanations for the loss of the cutting edge. Micro milling tools have a typical geometrical run out of several microns, up to 5 µm, as described in Chapter 1. This run out is in the same order of magnitude as the Feed Per Tooth (FPT). This can cause highly fluctuating loads on the end mill, and can double the cutting force on the cutting tooth with the largest radius. Furthermore, additional run out is introduced by the spindle, as explained before, enhancing this effect. It has been known from literature, that micro milling with two flute end mills is effectively done only by one of the two cutting edges due to this effect. The other cutting edge is only balancing the tooltip. In future experiments it is important to ensure that the cutting tool is intact when mounted in the spindle. In this experiment this has not been established before the milling experiment.

The loss of one tooltip increased the feed on the remaining tooltip with 2 times to 40 µm. This corresponds to the difference between the marks in the work piece in Figure 5.6. The chosen FPT of 20 µm, and the effective FPT of 40 µm are high when using micro milling tools. This can also be the reason for the loss of one cutting edge. Generally an FPT of 4-10 µm is used in micro milling, The optimal FPT will have to be found by performing further experiments. Figure 5.7 shows that the intact cutting edge is still of a reasonable quality.

The surface quality of the performed cut can be improved. Figure 5.6 shows that plastic deformation of the work piece material has occurred. This is probably caused by the relatively low depth of cut, namely 5 µm, and the high feed per tooth in this experiment. We expect that an increase in depth of cut, and a lowering of the feed per tooth will improve the cutting quality, this has to be investigated in future milling experiments.

Furthermore we can conclude that the tool holder design, which is presented in Chapter 4 was able to provide sufficient clamping force over the used rotational speed range to hold the cutting tool. No unwanted vibrations have been introduced by the tool holder. The run out introduced by the rotor-tool holder-tool connection, needs to be investigated.

Several other milling experiments have been conducted. Different cutting conditions have been investigated, among others a lower FPT. In these experiments the tool remained intact, contrary to the first milling test. However, these experiments emphasized the importance of further research into the optimal cutting conditions. It proved hard to find stable cutting conditions, and considerable run out was present.

Thus, further milling experiments need to be conducted to find the optimal cutting conditions with this milling setup. The run out at the tooltip needs to be determined, as well as the stability lobe diagram for this micro milling setup.

5.7 Conclusions and Recommendations

This chapter described the realization of a three-axis micro milling setup. The setup comprises of the vertically mounted miniature AMB spindle described in Chapter 3, an xy- positioning stage and a vertical z-stage.

The xy-positioning platform is a voice coil driven, needle bearing stage. The xy-stage has been provided by NXP/ITEC and is originally designed for the use in a wire bonding machine. The high spindle rotational speed and the minimum chip thickness effect require a minimum stage velocity of 5 mm$\cdot$s^{-1}. We aimed to reach the optimal Feed Per Tooth (FPT) within three spindle revolutions. Therefore a work piece acceleration of 21 mm$\cdot$s^{-2} (2.1 g) is required. The xy-stage is PID controlled to a bandwidth of 130 Hz, and has met the velocity and acceleration requirements. The spindle has been mounted to a commercially available z-stage from PI.

The novel tool holder as described in Chapter 4 forms the connection between the spindle and the micro cutting tool. The miniature AMB spindle and the tool holder have been investigated under milling conditions. A stable cut has been performed in brass using a 0.2 mm mill. The spindle rotational speed was set at 80.000 rpm. Tool and work piece inspection learned that the cutting conditions need to be improved. The Feed per Tooth was too high, and one cutting edge was damaged.

Future work includes optimization of the cutting conditions. The performance of the spindle and the setup need to be investigated at higher rotational speeds to further optimize machining conditions. The spindle is capable of rotational speeds up to 150.000 rpm. The finishing machining steps with µEDM and µECM require a higher positioning accuracy of the xy-stage. Currently this is limited by the 2D grid encoder. The positioning accuracy can be improved by increasing the measurement resolution.

Chapter 6

Design of a Short Rotor Spindle

6.1 Introduction

The rotational speed of spindles is continuously increased for applications such as micro-milling, grinding and flywheels for energy storage. The application of Active Magnetic Bearings (AMBs) in a micro milling spindle for high rotational speeds is shown in Chapter 3. High speed AMB spindles are commonly supported using two radial bearings and one axial bearing. This classical setup results in a relatively long rotor. The shape of the rotor heavily influences its dynamical behavior. In this chapter, we investigate the consequences of a drastic reduction of the rotor length in a high speed milling spindle. Rotor length reduction affects the speeding up of the rotor, rotor stability in an AMB system, AMB design, and the performance in the milling process. A novel AMB concept will be presented to support a very short rotor.

6.2 Motivation

The flexibility of a rotor often creates problems in high speed rotor applications. Flexible resonances are encountered when the rotor speeds up. In high speed micro-milling, vibrations can be introduced into the milling process. Regenerative vibrations in the milling process are referred to as chatter. By reducing the spindle length, flexible spindle resonances are shifted to a higher frequency. As a consequence excitation with the milling process is avoided. Furthermore we avoid exciting them during speeding up of the rotor.

6.3 Analysis and Simulation

The modeling and control of a rigid rotor suspended by AMBs has been described in Chapter 3. In this chapter we consider the influence of the rotor shape on the performance of a rigid spindle. The parameter under investigation is the ratio between the polar moment of inertia, I_z and the transverse moments of inertia I_x, I_y. A rotor is referred to as short when $I_z > I_x, I_y$, and as long when $I_z < I_x, I_y$. From literature [62, 45], we learn that there is a difference in rotor dynamic behavior of short and long rotors.

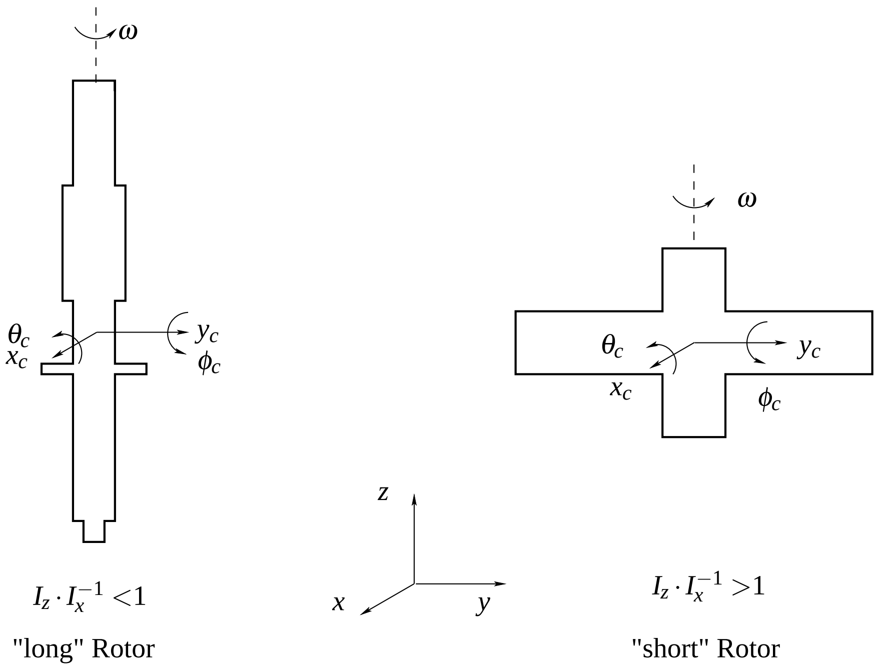

Figure 6.1: The two rotor shapes described in this section. The traditional long rotor, and the short version with increased flexural resonance frequencies.

We consider two rotor shapes, illustrated in Figure 6.1, both suspended with AMBs. In order to compare only the effect of the change in $I_z \cdot I_x^{-1}$ ratio, we take identical masses and identical transverse moments of inertia (I_x and I_y) for both rotor types. Initially the modal PID controllers are designed at zero rotational speed. Therefore the controllers for both modes, translating and tilting, are identical for the long and the short rotor.

Note that in case of the application of a short rotor spindle for very high rotational speeds, the rotor diameter has to be reduced to avoid high centrifugal stresses.

6.3.1 Critical speeds

In early literature [45], it can be found that it is less complicated to bring a short rotor up to high speed than a long rotor, partly considering critical speeds. A critical speed is that rotational frequency where it equals a spindle resonance frequency [62].

We distinguish the critical speeds into two types. The first are the rigid body critical speeds. In conventional spindles with ball bearings, hybrid bearings or air bearings, the rigid rotor resonance frequencies are generally higher than the flexible spindle resonances. The stiffness of Active Magnetic Bearings is generally one or two orders lower than the stiffness of contact bearings or air bearings. Therefore the rigid body critical speeds of AMBs are relatively low and encountered earlier than with contact or air bearings.

The rigid body modes are controlled by the modal PID controllers and can therefore be relatively well damped. Passing the rigid body critical speeds is usually not troublesome when a well-balanced rotor is applied.

The flexibility of the controlled stiffness of AMBs can be used to overcome critical speeds. The AMB controller determines the rigid body resonance frequencies. In the realized long rotor spindle described in Chapter 3, the early experiments were performed with an unbalanced rotor. The excitation of the rigid body modes during spin up by the mass unbalance made it impossible to pass the corresponding critical speeds. We have overcome the critical speeds by adjusting the controller in the vicinity of the critical speeds. As a critical speed is approached, the controller settings are changed, lowering the stiffness of the bearing. The stiffness is lowered in such an extent that the resonance frequency of the rotor is below the current rotational speed. This way, the critical speed is passed.

The critical speeds where the rotational speed equals a flexural natural frequency of the rotor are called flexural critical speeds. They are known to be particularly dangerous in conventional, contact rotor bearing systems [62]. AMBs offer the possibility to damp the flexural critical speeds as well, making it possible to overcome them. Flexural critical speeds are commonly overcome using notch filtering [63] but also with Linear Quadratic (LQ) control [64, 65], H^∞ controllers [66] and other controllers [43]. Shifting the spindle's flexible modes to higher frequencies, enables increasing the spindle speed without having to pass critical speeds corresponding to flexible spindle modes.

Reducing the spindle length, does not only influence the flexible spindle resonances, but also the rigid resonance frequencies of the spindle supported by active magnetic bearings.

Figure 6.2 shows the simulated Campbell diagram of the realized miniature AMB spindle, with a long rotor as described in Chapter 3. This long rotor has a

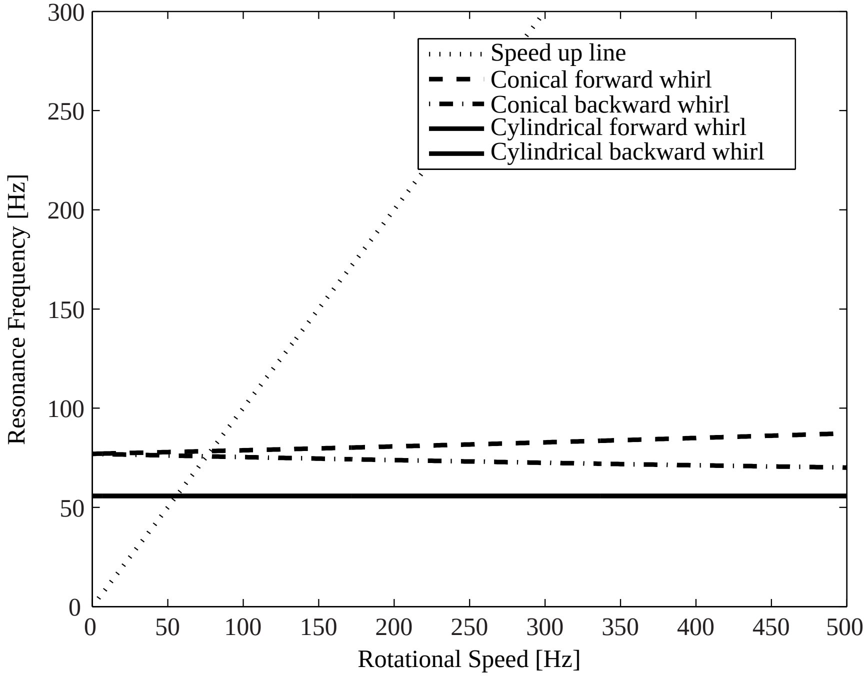

Figure 6.2: Campbell diagram of the "long rotor" with $I_z \cdot I_x^{-1}$=0.04.

$I_z \cdot I_x^{-1}$ ratio of 0.04. The Campbell diagram illustrates the four rigid rotor resonance frequencies as a function of the rotational speed. At zero rotational speed, two resonances are visible, the cylindrical mode and the conical mode. With increasing rotational speed, the two resonances split up in four resonance frequencies due to the gyroscopic coupling in the system. This is referred to as the splitting of the modes.

The cylindrical mode does not split up with increasing rotational speed in the case of symmetric rotors, rotors where the radial bearings are situated at equal distance from the COG of the rotor. In the miniature AMB spindle, described in Chapter 3, the COG is located 0.14 mm from the center of the two bearings. Therefore, the splitting of the cylindrical mode into a forward whirling mode and a backward whirling mode is not visible in Figure 6.2. The splitting of the conical mode is however clearly visible in Figure 6.2. This has been experimentally verified in Section 3.6.

Figure 6.2 shows a +1 slope line, the speed up line. At the intersections of this line with the spindle resonances, the rotational speed is equal to the spindle resonances, thus representing the critical speeds. Not all the critical speeds are equally difficult to overcome. A rotating unbalance, like a mass unbalance, excites the forward whirling resonances of the spindle. The backward whirl modes are not excited by the unbalance of the spindle, but can for example be excited in the unwanted event of the rotor touching a backup bearing.

The shape of the rotor influences the dependency of the resonance frequencies on the rotational speed. Figure 6.3 illustrates the Campbell diagram of a short rotor with $I_z \cdot I_x^{-1} = 1.3$. In this simulation, the mass and the moments of inertia in the x and y plane, I_x and I_y, and the controller are similar to the long rotor simulation. Therefore, the resonance frequencies for both rotors are identical at zero rotational speed, as can be seen by comparing Figures 6.2 and 6.3.

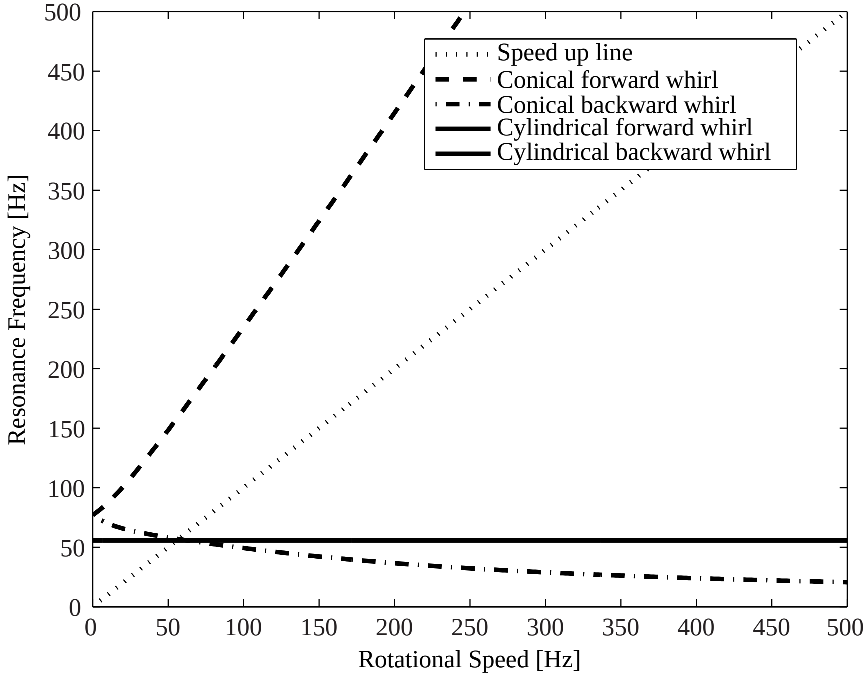

Figure 6.3: Campbell diagram of the "short rotor" with $I_z \cdot I_x^{-1}$=1.3.

In Figure 6.3 we can see that the conical modes of the short rotor with a $I_z \cdot I_x^{-1}$ ratio of 1.3 split much faster than the modes of the long rotor, as shown in Figure 6.2. This way, the conical forward whirl mode is avoided during spin up, which is otherwise most difficult to overcome. Thus, using a short rotor, not only flexible modes are avoided, but also a rigid mode critical speed is avoided. The conical forward whirling frequency has an asymptotic value of $I_z \cdot I_x^{-1}\omega$. Therefore, the ratio $I_z \cdot I_x^{-1}$ should not be chosen close to one in the design of a high speed rotor, to avoid excitation of the forward whirling frequency at its entire operating speed range. The resonance frequency corresponding to the conical backward whirl mode is considerably lower in the case of a shorter rotor, but this mode cannot be excited by a rotating unbalance and is therefore not difficult to overcome. The effect of these changing modes on stability is discussed in the next section.

6.3.2 Stability

The increase of the rotational speed of rotors with a relatively large $I_z \cdot I_x^{-1}$ ratio suspended by AMBs can lead to instability when not accounted for in the controller [67, 68, 69]. In this section the influence of the increase of the Iz·Ix^{-1} ratio on the stability of a high speed rotor is investigated. To study the stability of the rotor suspended by the AMBs we consider the closed loop poles of the system. The closed loop A-matrix of the system has been derived in Section 3.5. For the analysis in this chapter, we now consider a COG decoupled plant, which is derived in a similar way. The closed loop A-matrix of the system is again given by

$$\mathbf{A_{cl}} = \begin{bmatrix} \mathbf{A_p} - \mathbf{B_p D_c C_p} & \mathbf{B_p C_c} \\ -\mathbf{B_c C_p} & \mathbf{A_c} \end{bmatrix}, \tag{6.1}$$

where

$$\mathbf{A_p} = \begin{bmatrix} \mathbf{A_1} & \omega\mathbf{A_{12}} \\ \omega\mathbf{A_{22}} & \mathbf{A_2} \end{bmatrix}, \tag{6.2}$$

and where matrices $\mathbf{A_{12}}$ and $\mathbf{A_{21}}$ contain the polar moment of inertia I_z, and $\mathbf{A_1}$, $\mathbf{A_{12}}$, $\mathbf{A_{21}}$, and $\mathbf{A_2}$ contain the transverse moment of inertia I_x, showing the dependency of the system poles on the ratio of I_z and I_x.

In this section we consider the poles corresponding to the rigid rotor resonances, thus the conical and cylindrical whirling modes. In this simulation, the spindle is controlled with modal PID controllers that are not compensating for gyroscopic effects.

Figure 6.4 illustrates the effect of the $I_z \cdot I_x^{-1}$ ratio on the location of the poles of the rigid modes at a constant rotational speed of 50.000 rpm. The $I_z \cdot I_x^{-1}$ ratio of the long rotor described in Chapter 3 is 0.04. The cylindrical whirling poles, forward and backward, are shown in Figure 6.4 with a $\triangle$. The cylindrical whirling modes coincide at 50.000 rpm because we deal with a symmetric rotor. The bearings are located at equal distance from the COG. The conical whirling modes are illustrated in Figure 6.4 with the $\circ$ mark, and are clearly separated.

Figure 6.4 shows that the cylindrical whirling modes do not change with the changing $I_z \cdot I_x^{-1}$ ratio, as expected since the gyroscopic effect does not influence the cylindrical modes due to symmetry.

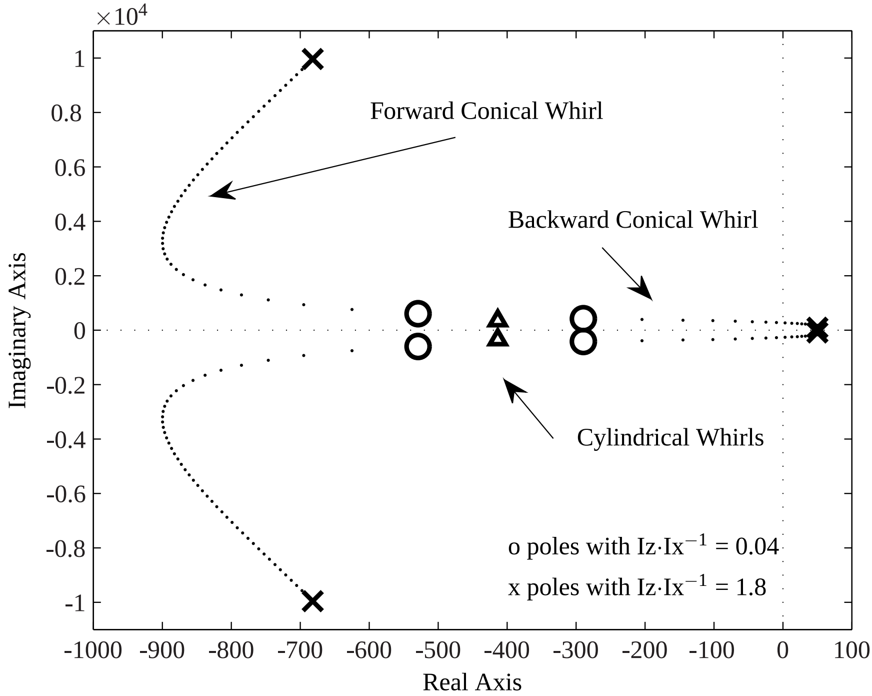

Figure 6.4: Pole map of the rigid body poles for changing $I_z \cdot I_x^{-1}$ ratios at 50.000 rpm

The conical whirling modes change with changing $I_z \cdot I_x^{-1}$ ratio. The conical modes are distinguished in a forward whirl with increasing frequency, and a backward whirling mode with decreasing frequency. Figure 6.4 shows that the forward whirling mode first moves away from the right half plane, and then approaches it. This can be explained by the limiting differentiating action of the controller, reducing the damping at high frequencies.

The pole for the backward conical whirling mode moves towards the right half plane with increasing $I_z \cdot I_x^{-1}$ ratio. From literature it is known that this mode can cause instability at high rotational speeds [67, 68, 69]. When PD control is applied, the conical backward whirl pole does not enter the right half plane, theoretically remaining stable. However time delays can in this case cause instability. When integrating control action is applied (PID), the gain of the controller at low frequencies increases, causing the conical backward whirling pole to enter the right half plane. Figure 6.4 shows the location of the backward whirling poles in the right half plane for a rotor with a $I_z \cdot I_x^{-1}$ ratio of 1.8 at 50.000 rpm controlled by modal PID controllers.

Note that there are more poles in the system, e.g. from the controller, which have to be considered but these are not shown in Figure 6.4.

This analysis shows that a modal controller without accounting for gyroscopic effect can not guarantee stability of a short rotor at high rotational speeds. More advanced control is required to stabilize a short rotor with active magnetic bearings at high rotational speeds.

6.3.3 Cross Feedback

We can account for the gyroscopic terms in the AMB controller using cross feedback. Cross feedback has briefly been addressed in Chapter 3. Cross feedback was first introduced by Okada et al. [68] and later applied by Ahrens et al. [67]. Ahrens used cross-feedback in addition to decentralized PID controllers.

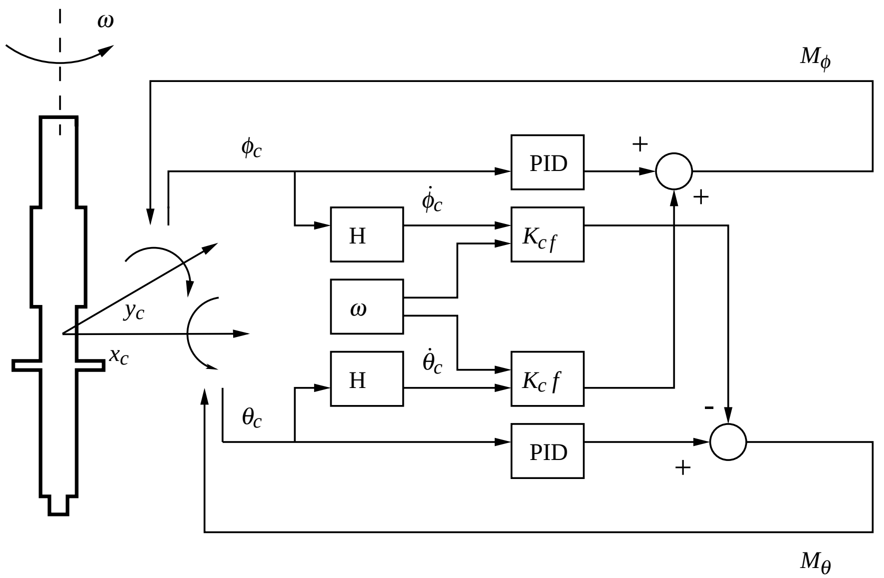

Figure 6.5: The working principle of the cross feedback controller when used in addition to modal PID controllers, where H is the observer.

In this research, cross feedback is used in combination with the modal controllers presented in Chapter 3. The cross feedback now applies to two of the four modal controllers, namely the rotor tilt controllers. In the cross feedback controller design, we extended the modal PID controllers with an additional cross feedback path. The working principle is illustrated in Figure 6.5.

The gyroscopic effect couples the rotor tilt rate around the COG in the zx-plane with the rotor tilt rate in the zy-plane, illustrated by matrix **G**, in Equation 3.24.

In the cross-feedback controller, the tilt rate of the rotor in a vertical plane is measured. This tilt rate is then multiplied with a, speed dependent, cross-feedback term, resulting in a torque. This torque is then applied in the orthogonal vertical plane, compensating for the gyroscopic coupling.

In the state space representation, this means that two speed dependent terms are placed in the $\mathbf{D_c}$ matrix of the controller, see Equation 6.3. $\mathbf{D_c}$ is structured in such a way that the dependency of the closed loop system on the rotational speed disappears. By doing so, the dependency of the terms $\mathbf{A_{12}}$ and $\mathbf{A_{21}}$ on the rotational speed in the closed loop A-matrix is compensated. However, this requires knowledge of all the states of the system, thus the gaps and the time derivatives of the gaps.

The position sensors only measure the displacement of the rotor in the AMBs, thus not all states are available. Therefore an observer is used to obtain the unknown states of the plant. In this case, the observer is a differentiation of the rotor tilt to obtain the tilt rate, as shown in Figure 6.5 where the observer is denoted as H. The system can now also be written in state space form. The closed loop A-matrix of the system including the observer is structured as:

$$\mathbf{A_{cl}} = \begin{bmatrix} \mathbf{A_p} - \mathbf{B_p D_c D_h C_p} & \mathbf{B_p C_c} & \mathbf{B_p D_c C_h} \\ -\mathbf{B_c D_h C_p} & \mathbf{A_c} & \mathbf{B_c C_h} \\ -\mathbf{B_h C_p} & \mathbf{0} & \mathbf{A_h} \end{bmatrix}, \tag{6.3}$$

where subscript h indicates the state space matrices of the observer. The additional states have been introduced by the observer. $\mathbf{D_c}$ contains the cross feedback terms, and is structured as

$$\mathbf{D_c} = \begin{bmatrix} D_t & 0 & 0 & 0 & 0 & 0 & 0 & 0 \\ 0 & D_r & 0 & 0 & 0 & 0 & 0 & \omega K_{cf} \\ 0 & 0 & 0 & 0 & D_t & 0 & 0 & 0 \\ 0 & 0 & 0 & -\omega K_{cf} & 0 & D_r & 0 & 0 \end{bmatrix}, \tag{6.4}$$

where D_t and D_r are the terms from the D matrix from the state space PID controllers for the translational and the tilting mode, respectively. The corresponding state vector $[\mathbf{x_3} \quad \mathbf{x_4}]^T$, and the cross feedback term K_{cf} are given by

$$\mathbf{x_3} = \begin{bmatrix} x_c \\ \theta_c \\ \dot{x}_c \\ \dot{\theta}_c \end{bmatrix} \quad \mathbf{x_4} = \begin{bmatrix} y_c \\ \phi_c \\ \dot{y}_c \\ \dot{\phi}_c \end{bmatrix} \quad K_{cf} = \frac{I_z}{K_i} . \tag{6.5}$$

When full cross feedback is applied, the poles of the system do not change with changing $I_z \cdot I_x^{-1}$ ratio. However, when full cross feedback is applied, delays in the system can cause instability [67]. Therefore it is advisable to partly compensate the gyroscopic effect with cross feedback, for example with 80 of 90 percent.

Figure 6.6 shows the results of the simulation of the closed loop poles, as described in section 6.3.2, but now with cross-feedback applied. Figure 6.6 shows the simulated poles for increasing $I_z \cdot I_x^{-1}$ ratio, showing that with 90 % cross feedback the system remains stable.

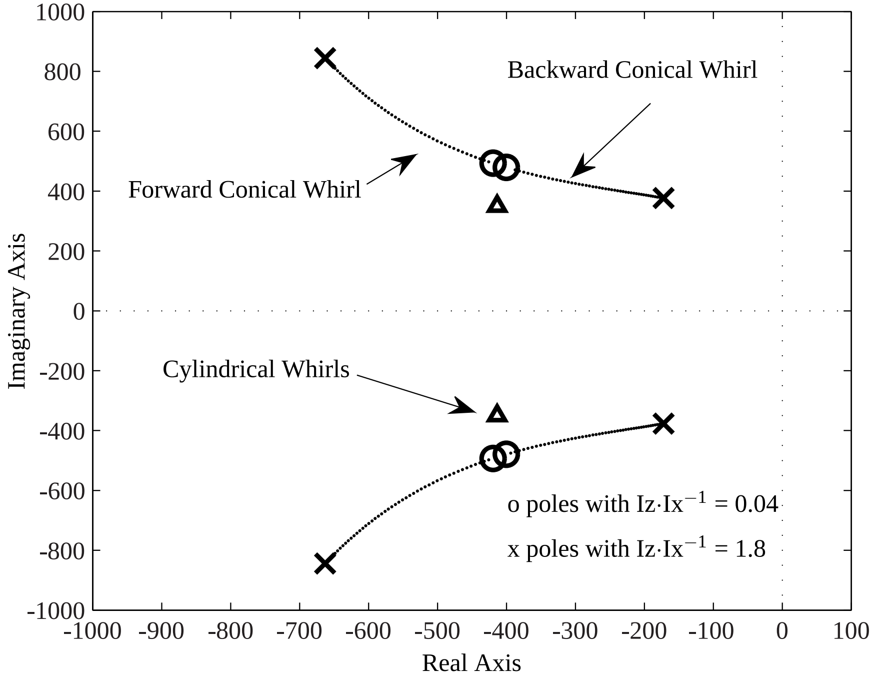

Figure 6.6: Pole map for the rigid body poles for changing $I_z \cdot I_x^{-1}$ ratios at 50.000 rpm with cross-feedback controller.

To verify the working principle of the cross-feedback controller, the cross feedback compensation scheme has been implemented and tested on the miniature AMB spindle as described in Chapter 3. In order to measure the effect of the cross feedback controller, the frequency response was measured from a torque applied in one vertical plane to rotor tilting in the orthogonal plane, as shown in Figure 6.7. The measurement was performed at zero rotational speed as well as at 125.000 rpm, with and without cross feedback. Figure 6.7 shows that considerable coupling exists without rotation between the tilt rates in the vertical planes. The coupling increases with rotational speed, as expected. The increase in coupling is larger than expected from the model. The cross feedback controller reduces the coupling by 5 dB in the

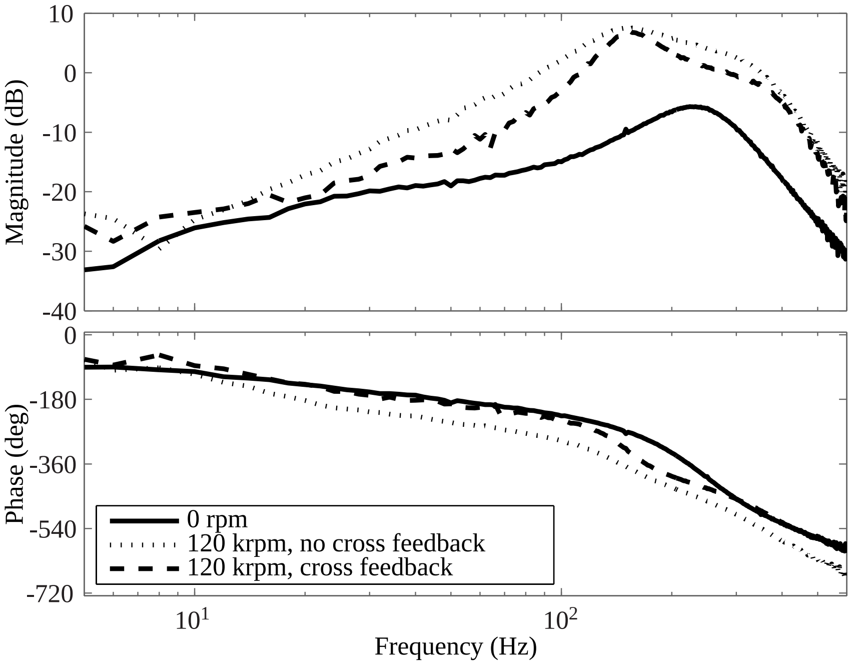

Figure 6.7: Measured closed loop frequency response of the cross coupling between the tilting in the two vertical orthogonal planes($\frac{\phi_c}{M_\theta}$). Measured at 0 rpm, at 125.000 rpm with and without cross feedback.

range between 20 and 100 Hz. Below 20 Hz, the measurement is unreliable.

6.3.4 Milling Performance

In this section, the effect of the rotor length reduction on the positioning performance of the milling spindle is investigated. A time simulation is done where the static part of the milling force is applied to the tool tip, in the x-direction only. The position of the tool tip is observed. A similar simulation is described for the long rotor setup in Section 3.5.2.

Figure 6.8 shows the response of the long rotor as presented in Chapter 3 with a $I_z \cdot I_x^{-1}$ ratio of 0.04 and a short rotor with $I_z \cdot I_x^{-1}$=1.3 to the static part of the cutting force. The rotational speed is set at 150.000 rpm, with no cross feedback applied. Figure 6.8 shows that the short rotor is unstable, as shown in Section 6.3.2 as well. The long rotor system is stable under these conditions.

Figure 6.9 shows the response of the two rotors with 95% additional cross-

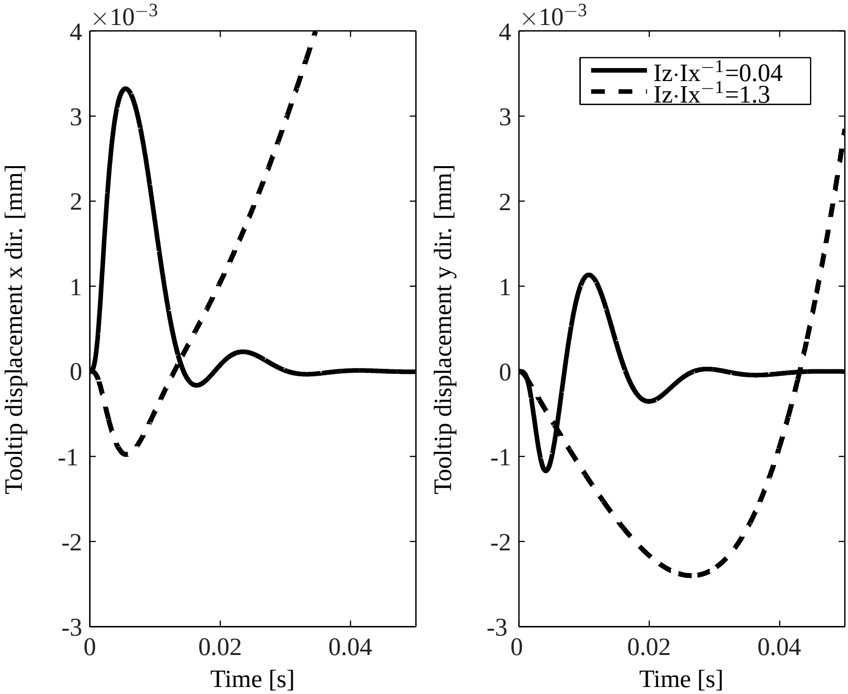

Figure 6.8: Tooltip response of the long and short rotor setup at 150.000 rpm. Under the influence of the static part of the cutting forces in x-direction without cross feedback compensation.

feedback, also at 150.000 rpm. When 100% cross-feedback is applied, there would be no response in the y-direction, and the response in the x-direction would be identical for the two rotors. However in practice, 100% cross feedback is not realizable. 100% cross feedback would require exact knowledge of the rotational speed, the rotor properties and the position derivative states. The simulation in Figure 6.9 shows that with 95% cross-feedback, the response in the orthogonal direction to the applied force is much larger for the rotor with a $I_z \cdot I_x^{-1}$ ratio of 1.3 than for a rotor with a $I_z \cdot I_x^{-1}$ ratio of 0.04. From these simulations we can conclude that when a shorter rotor is applied, cross feedback, or other advanced control is required in order to achieve good positioning performance. It is of utmost importance to consider whether full compensation for gyroscopic effects, for example using a cross feedback controller, is feasible, due to the lack of exact knowledge of the system and its states, or due to time delays in the closed loop system. Furthermore, other types of coupling can be present in the system, such as an electromagnetic cross-coupling between the actuators.

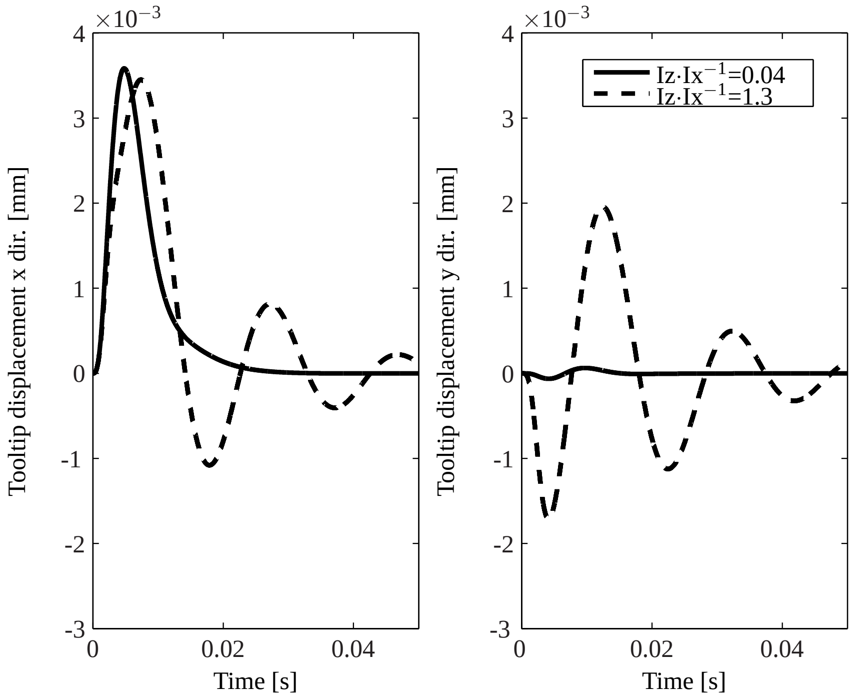

Figure 6.9: Tooltip response of the long and short rotor setup at 150.000 rpm. under the influence of the static part of the cutting forces in x-direction with 95% cross-feedback compensation.

6.3.5 Conclusions

In the previous sections the effect of decreasing rotor length on the rotor dynamics and on the milling process has been investigated. Decreasing spindle length has a positive effect on the milling process, because spindle resonances can be moved away from the operating frequencies.

Reducing the spindle length reduces the number of critical speeds that need to be passed during spin up. The passing of multiple flexural critical speeds can be avoided, as well as the passing of the forward critical rigid whirling mode. Therefore it is easier to bring a short rotor up to speed than a long rotor.

Reducing the spindle length, however, can cause instability at high rotational speed. Due to the gyroscopic effect, two poles of the system move towards the right half plane. This can be avoided by using more advanced control algorithms, such as a cross feedback controller. Due to the large gyroscopic coupling, advanced control is necessary in order to achieve the same positioning performance as with a longer type rotor.

Taking this into consideration, it would be interesting to further explore the possibility of reducing the rotor length for fast rotating spindles, such as a micro milling spindle. In the next sections, the design of a functional model to investigate the performance of a rotor with a large $I_z \cdot I_x^{-1}$ ratio is described.

6.4 Novel Spindle Concept

In the previous Sections, 6.1 to 6.3.5 it has been shown that a short, disk shaped rotor has several advantages over a traditional long rotor. It is not feasible to support a disk-shaped rotor with conventional AMB technology. This section describes the design of an AMB support for a rotor with a large $I_z \cdot I_x^{-1}$ ratio. Efforts have been made in the field of AMB design to reduce the rotor length by combining radial and axial bearings [47].

Figure 6.10 illustrates a novel AMB configuration to support a disk-shaped rotor. This concept is based on a combined radial-axial bearing concept [47]. The functionality of the proposed bearing can be extended by adding two degrees of freedom. A fully 5 DOF bearing system is obtained by controlling the currents in the two radial bearing stators independently.

In this short rotor concept, a radially polarized permanent magnet provides the bias flux for the radial as well as the axial bearing, enabling a very compact design. The bias flux serves two purposes; it increases the linearity of the actuator, and it increases its force slew rate.

The concept illustrated in Figure 6.10 is a homo polar type. The importance of the use of homo polar AMBs in high speed applications with non-laminated rotors is described in Chapter 3. This way, the magnetization of the rotor does not change in each revolution.

Another way of combining radial and axial magnetic bearings is described by Masuzawa et al. [70]. This principle is illustrated in Figure 6.11. In this bearing concept, permanent magnets also provide the bias flux for the radial as well as the axial bearing.

Disadvantages of this concept mainly regard manufacturability. The concept is not rotational symmetric, and mounting of for example a milling tool is more tedious. Furthermore the bias flux in the radial bearings is heavily influenced by the actuation in the axial direction, as illustrated in Figure 6.11. An advantage of this concept is that the diameter of the rotor can be smaller, making it more favorable for very high speed applications considering centrifugal loads. Note that an alternative rotational axis can be chosen in this concept, for example horizontal in Figure 6.11 in stead of vertical.

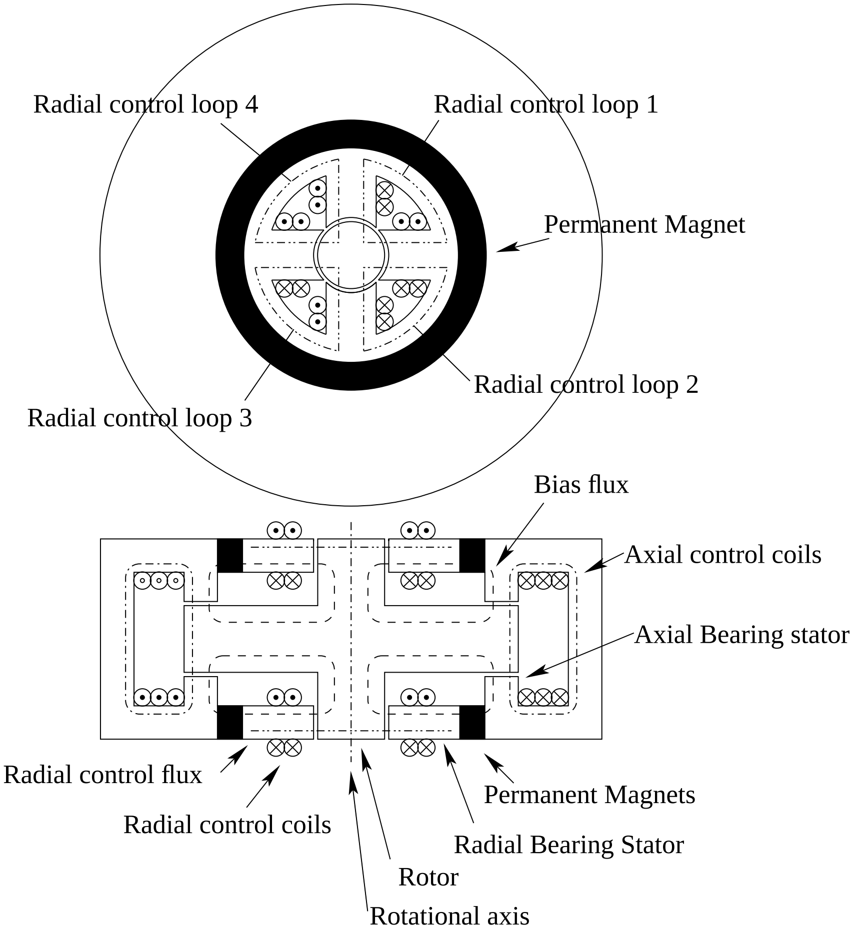

Figure 6.10: The principle of the novel AMB setup

The concept presented in Figure 6.10 has been chosen to be used to support a short rotor type spindle.

6.5 Bearing Analysis

This section describes the analysis of the bearings in the concept presented in Section 6.4. The fundamental equations as described in Chapter 2 are applied.

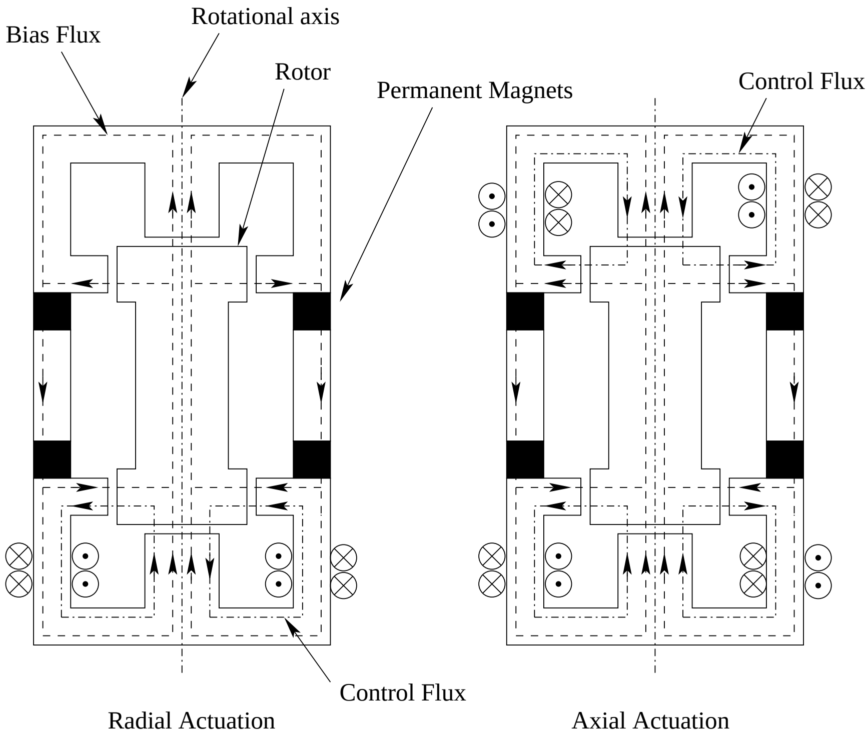

Figure 6.11: Combined radial-axial active magnetic bearing concept by Masuzawa et al., the actuation in one radial bearing is illustrated, as well as the actuation for the axial bearing [70].

6.5.1 Radial Bearing Force

The flux density in the air gaps is calculated using the Maxwell equations, the conservation of flux, and Ampère's circuital law. The same assumptions described in Chapter 2 are done. The permanent magnets create the bias flux in the radial air gap as well as the axial air gap. For the analysis in the radial bearing, a quarter of the setup is considered. This bias flux in the radial air gap, B_{mr}, is given by:

$$B_{mr} = \frac{\mu_0 B_r H_c A_m A_{ga} l_m}{B_r A_m (4 l_{ga} A_{gr} + l_{gr} A_{ga}) + 4 \mu_0 H_c l_m A_{ga} A_{gr}}. \tag{6.6}$$

In equation 6.6, B_r and H_c represent the remanence flux density and the coercive force from the permanent magnet, μ_0 is the relative permeability of air. A_{gr} is the pole shoe surface, l_{gr} and l_{ga} are respectively the lengths of the radial air gap and the axial air gap. A_m and l_m are the surface area and the thickness of the permanent magnet. In equation 6.6 one can see that the flux density in the radial air gap, and thus the radial bearing force, depends on the length of the axial air gap (l_{ga}).

The flux density in the radial air gaps, caused by the control coils, is derived by taking the circuit equations for the loops illustrated in Figure 6.10. This derivation has been performed for the miniature spindle and is described in Section 3.3.4. The flux density in the right radial air gap generated by the x-coils and the rotor in center position is given by:

$$B_{cr} = \mu_0 \frac{n_r i_x (2l_{gr} + x)}{2l_{gr}^2 - x^2}, \tag{6.7}$$

where n_r is the number of windings per leg, and i_x is the applied current. From equation 6.6 and 6.7, we have the information on the total flux density in the radial air gaps. From the total flux density in the air gaps, we can calculate the force acting on the rotor in the radial AMB. The force is calculated by taking the partial derivative of the magnetic energy stored in the air gap with respect to the air gap. The force in one reluctance actuator has been derived in Chapter 2, and is given by:

$$F_x = B_{rt}^2 \frac{A_{gr}}{2\mu_0}, \tag{6.8}$$

where B_{rt} is the total flux density in the airgap. The bearing consists of two actuators in differential driving mode. The resultant force in the right air gap is thus the difference of these two forces, and given by:

$$\begin{aligned} F_x = \; & \frac{A_{gr}}{2\mu_0}\left(\frac{\mu_0 B_r H_c A_m A_{ga} l_m}{B_r A_m (4l_{ga}A_{gr} + (l_{gr} - x)A_{ga}) + 4\mu_0 H_c l_m A_{ga} A_{gr}} + \frac{\mu_0 n_r i_x (2l_{gr} + x)}{2l_{gr}^2 - x^2}\right)^2 - \\ & \frac{A_{gr}}{2\mu_0}\left(\frac{\mu_0 B_r H_c A_m A_{ga} l_m}{B_r A_m (4l_{ga}A_{gr} + (l_{gr} + x)A_{ga}) + 4\mu_0 H_c l_m A_{ga} A_{gr}} - \frac{\mu_0 n_r i_x (2l_{gr} - x)}{2l_{gr}^2 - x^2}\right)^2 \end{aligned} \tag{6.9}$$

Equation 6.9 shows that the force from the radial bearing actuator is non-linear with respect to the bearing current and position. Equation 6.9 furthermore shows that the force in the radial bearing depends on the axial air gap. This means that inherent in the presented design there is cross-talk between the radial bearings and the axial bearing. Under the assumption of small rotor deviations, x, we can linearize the force on the rotor in its equilibrium position. The linearized bearing force as a function of position x and applied current i_x is given by:

$$F_x = K_x x + K_{ix} i_x. \tag{6.10}$$

In equation 6.10, K_x is the force-position dependency of the magnetic bearing, and also called the negative stiffness. K_{ix} is the force current dependency of the bearing. K_x and K_{ix} are given by:

$$\begin{aligned} K_x &= \frac{2\mu_0 A_{ga}^3 A_{gr} A_m^3 B_r^3 H_c^2 l_m^2}{(A_m B_r (A_{ga} l_{gr} + 4A_{gr} l_{ga}) + 4\mu_0 A_{ga} A_{gr} H_c l_m)^3} \\ K_{ix} &= \frac{2\mu_0 A_{ga} A_{gr} A_m B_r H_c l_m n_r}{l_{gr}(A_m B_r (A_{ga} l_{gr} + 4A_{gr} l_{ga}) + 4A_{ga} A_{gr} H_c l_m \mu_0)}. \end{aligned} \tag{6.11}$$

6.5.2 Axial Bearing Force

We derive the force in the axial bearing the same way as we have done for the radial bearings. The expression for the flux density in the axial air gaps generated by the permanent magnets is given by:

$$B_{ma} = \frac{4\mu_0 B_r H_c A_m A_{gr} l_m}{B_r A_m (4 l_{ga} A_{gr} + l_{gr} A_{ga}) + 4\mu_0 H_c l_m A_{ga} A_{gr}}, \tag{6.12}$$

where A_{ga} is the axial bearing pole shoe surface. The flux density in the axial air-gaps, created by the axial bearing coils is given by:

$$B_{ca} = \mu_0 \frac{n_a i_z}{l_{ga}}, \tag{6.13}$$

where n_a is the number of windings in one stator. Note that the flux density in the airgap caused by the coils does not depend on the axial displacement of the rotor. The reluctance of this circuit does not depend on the rotor position. The net force in the axial bearing actuator is given by

$$\begin{aligned} F_z = \; & \frac{A_{ga}}{2\mu_0} \left(\frac{4\mu_0 B_r H_c A_m A_{gr} l_m}{B_r A_m (4(l_{ga} - z) A_{gr} + l_{gr} A_{ga}) + 4\mu_0 H_c l_m A_{ga} A_{gr}} + \frac{\mu_0 n_a i_a}{l_{ga}} \right)^2 - \\ & \frac{A_{ga}}{2\mu_0} \left(\frac{4\mu_0 B_r H_c A_m A_{gr} l_m}{B_r A_m (4(l_{ga} + z) A_{gr} + l_{gr} A_{ga}) + 4\mu_0 H_c l_m A_{ga} A_{gr}} - \frac{\mu_0 n_a i_a}{l_{ga}} \right)^2 \end{aligned} \tag{6.14}$$

Equation 6.14 also shows the cross-talk between the radial and axial bearings. We can again linearize the bearing force around the working point z_0, i_0. The linearized force acting on the rotor from the axial bearing is given by:

$$F_z = K_z z + K_{iz} i_z, \tag{6.15}$$

where the negative bearing stiffness and force current dependency are given by:

$$\begin{aligned} K_z &= \frac{128\mu_0 A_{ga} A_{gr}^3 A_m^3 B_r^3 H_c^2 l_m^2}{(A_m B_r (A_{ga} l_{gr} + 4A_{gr} l_{ga}) + 4\mu_0 A_{ga} A_{gr} H_c l_m)^3} \\ K_{iz} &= \frac{8\mu_0 A_{ga} A_{gr} A_m B_r H_c l_m n_a}{l_{ga}(A_m B_r (A_{ga} l_{gr} + 4A_{gr} l_{ga}) + 4\mu_0 A_{ga} A_{gr} H_c l_m)}. \end{aligned} \tag{6.16}$$

In this section, an analytical expression for the flux densities and the forces in the proposed short rotor setup has been derived. These analytical expressions are used to dimension the initial design of the novel spindle prototype. Furthermore this section presents the linearized expressions for the forces for the radial and the axial bearings. These linearized forces are used for the design of the controllers, in combination with the rotor dynamic model presented in Chapter 3

6.6 Design of the Short Rotor AMB

This section describes the design of a functional model using the compact AMB principle as shown in Figure 6.10. The bearings are dimensioned using the analytical derivation from previous Section 6.5. By choosing for a short rotor concept, the rotor inherently has a relatively large diameter. The structural integrity of the rotor has to be ensured under the influence of centrifugal loads, and thus determines its diameter. The design of the bearings of the short rotor spindle is illustrated in Figure 6.12 and 6.13. The bearings are dimensioned in such a way that the rotor diameter is kept to a minimum, without affecting manufacturability.

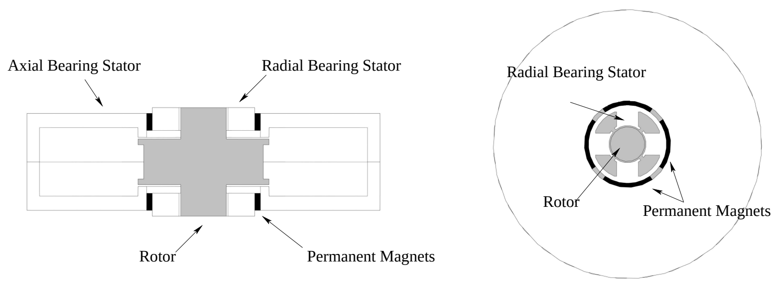

Figure 6.12: Section view and top view of the short rotor setup.

This section will focus on the design of the active magnetic bearings. A permanent magnet synchronous drive will be situated around the outer circumference of the disk, with minimal increase in rotor length. The axial bearing stator is large to accommodate for the stator of the spindle drive. The integration of the spindle drive will be further addressed in Section 6.8. The considerations for dimensioning permanent magnet biased permanent active magnetic bearings are described in Section 3.3.5. The bearings are designed in such a way that the bias flux density in the air gaps is around 0.6 T, and that the negative stiffness of the magnetic bearings is about one order lower than the positive, controlled stiffness that we would like to achieve. The desired closed loop stiffness is aimed at $1.4 \cdot 10^5$ N/m, a bandwidth of

350 Hz assuming a rotor mass of 30 gr, see Section 3.2.1, Chapter 3. Therefore the actuators are designed to have a negative stiffness in the order of $1 \cdot 10^4$-$1 \cdot 10^5$ N/m. The dimensions and properties of the short rotor setup design are listed in table 6.1

The radially magnetized ring illustrated in Figure 6.10 is replaced by four magnet ring segments. The magnet ring segments can be radially magnetized, and are therefore better manufacturable than a full ring. Furthermore, the space between the ring segments can be used to house the position sensors, in order to achieve sensor actuator co-location.

Table 6.1: Dimensions and bearing properties of the short rotor setup.

Rotor Length	$19 \cdot 10^{-3}$	m
Rotor Disk Diameter (w/o magnet)	$23 \cdot 10^{-3}$	m
Rotor Disk Diameter (w magnet)	$33 \cdot 10^{-3}$	m
Rotor Shaft Diameter	$8 \cdot 10^{-3}$	m
Rotor Mass (w/o magnet)	$26.7 \cdot 10^{-3}$	kg
Rotor Mass (w magnet)	$32.4 \cdot 10^{-3}$	kg
Magnet surface area	$1.32 \cdot 10^{-4}$	m^2
Magnet length	$1 \cdot 10^{-3}$	m
Bearing Magnet coercive force	$880 \cdot 10^3$	A/m
Bearing Magnet remanence	1.1	T
Radial Pole shoe area	$2.3 \cdot 10^{-5}$	m^2
Radial Airgap length	$3 \cdot 10^{-4}$	m
Number of windings, Radial	30	$-$
Negative stiffness, Radial	$1.5 \cdot 10^4$	N/m
Force current dependency, Radial	3.6	N/A
Pole shoe area, Axial	$1 \cdot 10^{-4}$	m^2
Airgap length, Axial	$3 \cdot 10^{-4}$	m
Number of windings, Axial	30	$-$
Negative stiffness, Axial	$1.2 \cdot 10^5$	N/m
Force current dependency, Axial	14	N/A

The short rotor setup is dimensioned using the analytical expressions for the flux densities and expressions derived in Sections 6.5.1 and 6.5.2. These expressions were derived under several assumptions, listed in Chapter 2. In the next section, the analytical derivation will be verified using Finite Element Method (FEM) Modeling.

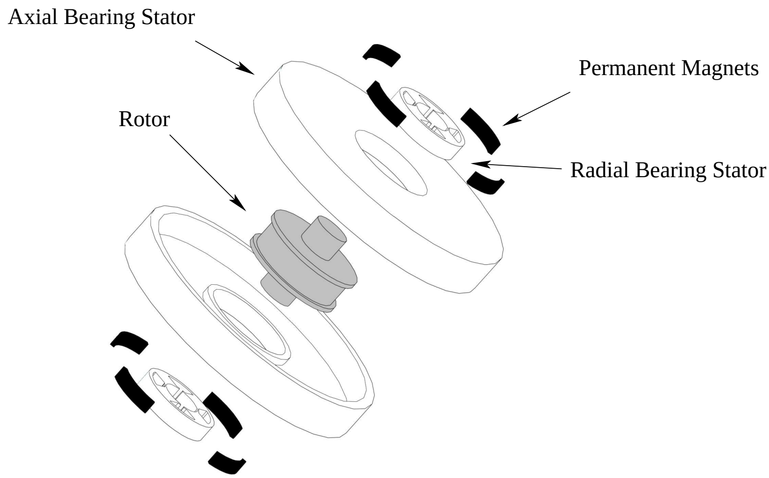

Figure 6.13: Exploded view of the short rotor setup.

6.7 FEM Analysis

In this section the analytical derivation of the flux densities in Sections 6.5.1 and 6.5.2 is verified. Especially due the small dimensions of the design, it is important to observe the leakage flux in the system, since the assumption of no leakage flux has been made. The flux densities in the air gaps, and the other iron parts in the magnetic loop are calculated with Finite Element Method (FEM) Modeling. ANSYS FEM software has been used for the simulations.

The flux densities in the air gaps created by the coils and the permanent magnets are calculated separately, as well as combined, in order to examine where the differences occur. The results of the analytical calculation and the FEM Modeling are illustrated in Table 6.2.

Table 6.2 shows that the analysis of the axial, as well as the radial bearings, using an analytical model, results in an overestimation of the bias flux density. Thus we can conclude that the simplification described Chapter 2 is not allowed. The bias flux created by the permanent magnets is illustrated in Figure 6.14. Table 6.2 shows that the approximation of the control flux in both bearings is much better.

Figure 6.14 shows that considerable stray flux is present on the inner side of the radial air gaps, and that leakage flux is present from the radial bearing stators to the

Table 6.2: Comparison of flux densities derived from analytical and FEM simulations.

Parameter	Analytical	Finite Element
Radial air gaps, magnets only	0.7 T	0.48 T
Axial air gaps, magnets only	1 T	0.63 T
Radial air gap, 2 A radial , no PM	0.25 T	0.25 T
Axial air gap, 2 A axial , no PM	0.25 T	0.16 T
Radial air gap high, 2 A radial, with PM	0.95 T	0.72 T
Radial air gap low , 2 A radial, with PM	0.45 T	0.24 T
Axial air gap, 2 A high axial, with PM	1.25 T	0.77 T
Axial air gap, 2 A low axial, with PM	0.75 T	0.47 T

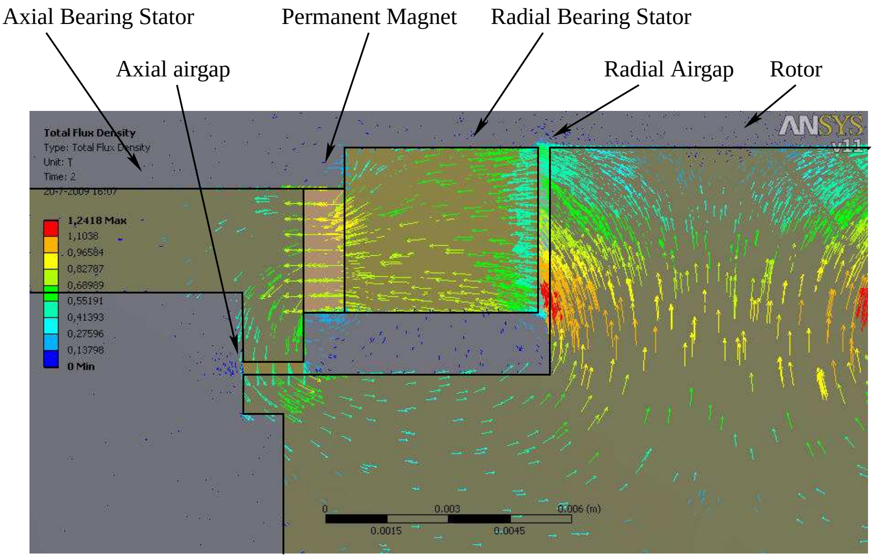

Figure 6.14: Flux density levels in the design generated by the permanent magnets.

rotor. This could explain the lower flux density obtained using the FEM modeling.

Furthermore, the results in table 6.2 show a difference in the results for the actuation in the axial direction. This difference can be explained considering the calculation of the axial actuation flux density without permanent magnets. The results from this FEM analysis are shown graphically in Figure 6.15.

Figure 6.15 shows that part of the flux created by the axial actuation coils enters the rotor through the radial air gaps. This is due to the small thickness of the permanent magnets (1 mm). This is not a problem when accounting for it in the

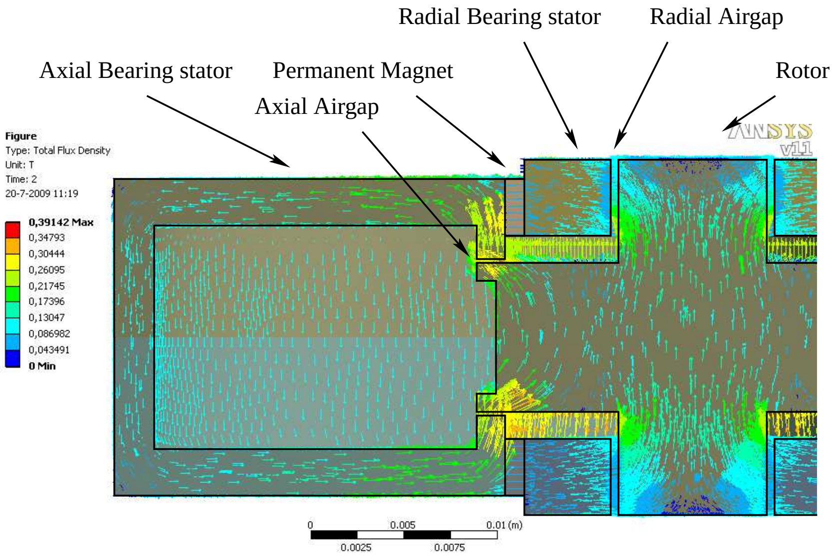

Figure 6.15: Flux density levels in the design with only actuation of the axial bearing coils, the permanent magnets are replaced by air elements in this simulation

dimensioning of the axial bearing coils, and the realization of the fact that the negative stiffness of the radial bearings slightly increases when the axial bearing coils are actuated. This is, however, a symmetrical phenomenon, and can be accounted for by the controller. Concluding, a FEM analysis is required in the design of an Active Magnetic Bearing with reduced dimensions.

6.7.1 Time Simulation

By using a shorter, smaller rotor, a higher control bandwidth can be achieved due to the lower moving mass. However, in micro-milling we deal with force disturbances on the tool tip. Reducing rotor weight increases the sensitivity to cutting force disturbances, especially as they occur well above the bandwidth of the controller where the response is mainly determined by the rotor mass. This section describes a time simulation of the performance of the short rotor setup under influence of the cutting forces. The rigid rotor model as described in Section 3.5 is used for these simulations. The cutting forces, as predicted in Section 3.2.1, are applied to the tooltip of the short rotor spindle. We again consider two responses of the system, the response to the dynamic part of the cutting forces, and the response to the static part of the cutting forces. The bandwidth of the short rotor system in this simulation is tuned to be 750 Hz. Cross feedback is added to the controller of the short rotor system as it is required for stability, as explained in Section 6.3.3. The cross-feedback percentage is 95%, mainly because 100% will not be realizable in practice.

In order to compare the performance of the long and the short rotor with respect to cutting force disturbance rejection, consider Figures 3.14 and 3.15 in Chapter 3. Figures 6.16 and 6.17 show the simulated responses of the tool tip in the short rotor system.

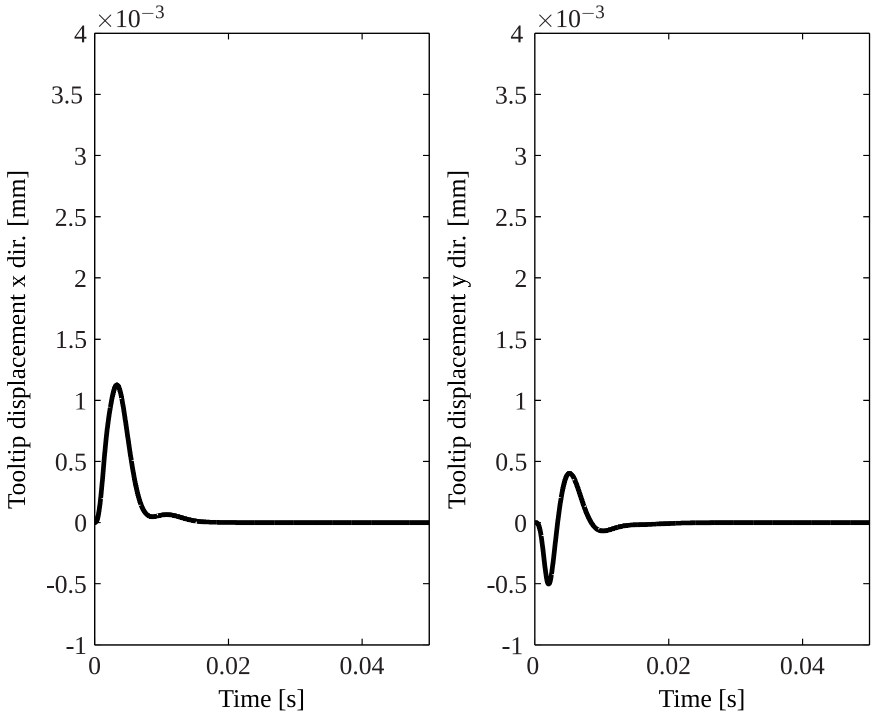

Figure 6.16: Tooltip response of the short rotor in x and y direction when the static part of the cutting force(0.1 N) is applied in x-direction. Simulated during full slot milling in tool steel with a tool diameter of 0.2 mm at a rotational speed of 150.000 rpm. 95% cross-feedback is applied.

Figure 6.16 shows that the short rotor system reacts better to a step disturbance force than the long rotor setup, as could be expected due to the higher control bandwidth. However the response orthogonal to the applied force is bigger in case of the short rotor system, even with 95% cross feedback. This illustrates the large effect of the gyroscopic coupling. The response to the dynamic part of the cutting force of

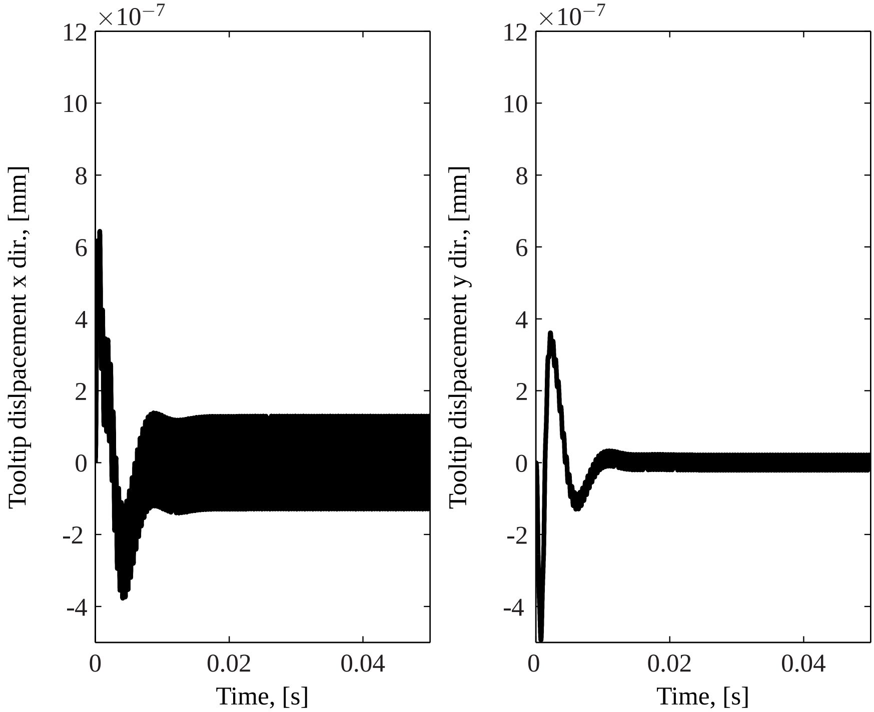

Figure 6.17: Tooltip response of the short rotor in x and y direction when the dynamic part of the cutting force (0.1 N) is applied in x-direction. Simulated during full slot milling in tool steel with a tool diameter of 0.2 mm at a rotational speed of 150.000 rpm. 95% cross-feedback is applied

the short rotor is larger than that of the long rotor, as shown in Figure 6.17. This is expected and still acceptable for our application.

6.8 Motor Drive Integration

The study on the miniature AMB spindle presented in Chapter 3, has revealed that the main factor limiting the performance was the negative stiffness from the spindle drive. The negative stiffness in combination with eccentric mounting of the rotor magnets results in a synchronous disturbance. Therefore we need a motor drive with lower radial negative stiffness. Research on the drive of the short rotor spindle is carried out in collaboration with Borisavljevic [71] in the same research program. The aim of this research is the integration of a spindle drive in the setup as presented in the previous section. Furthermore, the challenge of elevated rotational speed is investigated. The current state of the art, commercially available synchronous drives have a maximum rotational speed of 250.000 rpm. In this research, the desired rotational speeds are well above this rotational speed, in the range of 300.000-500.000 rpm.

The motor magnets are mounted on the circumference of the rotor disk. This has the advantage of increased motor torque due to the larger diameter. In addition, the increase in rotor length can be minimal. Disadvantage is that extra measures have to be taken to ensure rotor integrity at high rotational speeds.

The proposed design of the spindle drive [71], integrated into the design described in Section 6.6, is shown in Figure 6.18. The motor stator is a slotless type, with toroidally wound coils. By using a slotless design, the radial negative stiffness in the motor is reduced. The stator for the spindle drive is mounted inside the stator for the axial bearing.

A two-pole rotor magnet is fitted around the circumference of the rotor disk. The rotor magnet is a plastic bonded permanent magnet. In order to make the rotor able to withstand high rotational speeds, a fiber sleeve will be mounted around the rotor magnet. The fiber sleeve will be pre-tensioned. This pre-tension will be partly canceled by the centrifugal stresses, and the remaining pre-tension will retain the magnets at high rotational speeds.

6.8.1 Motor-Bearing Interaction

The principle of superposition of magnetic fields states that the fields of the bearings and the motor can be added and subtracted, and that there is no interaction between the two. This is valid under the condition of constant μ_r of the stators and the rotor. This will not be the case, especially at high flux densities. Therefore, interaction between the magnetic fields of the motor and the bearings is likely to occur, due to the small dimensions of the system, and the fact that the motor stator is mounted inside the axial bearing stator. Finite Element analysis will have to be done in order to investigate this magnetic coupling.

In order to investigate the bearing and motor functions independently, two prototypes will be built. One setup, supporting the rotor without permanent magnet by the combined AMBs will be manufactured to investigate the feasibility and performance of the bearings. A second setup has been manufactured in order to develop the permanent magnet drive presented in this Section [72]. This setup is equipped with air bearings in order to minimize friction and enable a high rotational speed. The use of air bearings makes sure that there are no effects of the active magnetic bearings on the performance of the spindle drive.

6.9 Setup

Figure 6.18 shows the designed short rotor setup, including the novel bearing concept and the PM synchronous motor. Optical fiber sensors are implemented for the rotor position measurement. The small diameter of the sensor tips (0.8 mm) allows for co-location of the sensors and actuators.

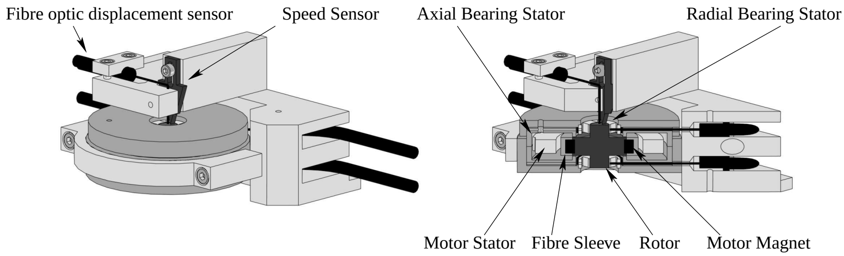

Figure 6.18: Proposed setup design of the short rotor AMB system, including PM synchronous motor.

6.10 Conclusions and Recommendations

In this chapter, the further downscaling of a miniature AMB spindle is investigated. Shifting spindle resonance frequencies to a higher frequency has a positive effect on the quality of the milling process. The implication of drastically shortening the rotor length to increase these resonance frequencies on the rotor dynamic behavior has been studied. A rotor dynamic analysis shows that reducing the rotor length to such an extent that $I_z > I_x, I_y$ drastically increases the gyroscopic coupling, and therefore influences the critical speeds and the stability of the system in combination with active magnetic bearings.

By reducing the spindle length to a case where $I_z > I_x, I_y$, one self exciting critical speed can be avoided, making it easier to bring the rotor up to its operating speed. Obviously, flexural critical speeds are avoided as well. Unfortunately, the closed loop poles of the system with active magnetic bearings move towards the right half plane, eventually causing instability when not accounted for in the controller. A cross-feedback controller is presented, in addition to modal PID controllers to stabilize a short rotor system with active magnetic bearings. This controller is experimentally verified on the miniature AMB spindle presented in Chapter 3 The benefits of the increased resonances and the avoiding of one critical speed make it worthwhile to further investigate a short rotor system for high speed rotation.

A novel AMB system is presented to support a short, disk-shaped rotor in 5 DOF. In this concept a permanent magnet is used to provide the bias flux for the radial, as well as the axial actuation, enabling a very compact design. The forces in the AMB concept are derived analytically, and the flux densities are verified using FEM.

Future work consists of the realization of the short rotor setup. Firstly, the working principle of the novel bearing concept needs to be verified. Secondly, a spindle drive has to be integrated, and the motor bearing interference needs to be studied. Thirdly, the short rotor needs to be tested during rotation. Due to the large gyroscopic coupling, the quality of the cross-feedback is of utmost performance. It has to be studied whether the coupling can be predicted, and thus compensated for sufficiently in order to maintain stability of the entire operating range, and to achieve sufficient positioning accuracy.

Chapter 7

Sensor Choice in High Speed AMB Systems

In this chapter, several position sensing principles for Active Magnetic Bearing (AMB) systems are compared, theoretically as well as experimentally. The goal of this investigation is to find a suitable position sensing system for the short rotor functional model as described in Chapter 6. This chapter describes an investigation into the performance of the eddy current sensors used in the miniature AMB spindle, as well as the selection for a position measurement sensor for the short rotor functional model described in Chapter 6.

7.1 Introduction

A high quality position displacement signal is essential when high positioning accuracy needs to be achieved in a mechatronic system, such as the miniature AMB spindle.

A magnetic bearing system requires a stabilizing feedback loop, as described in Chapter 2. This feedback can be provided in various ways, for example by a flux measurement or a position measurement. It is possible to stabilize a magnetic bearing without a separate sensor, a so called sensorless AMB, however this is beyond the scope of this research.

In the design of a miniature spindle for micro milling, we focus on the positioning performance of the rotor in the bearings. Therefore it is most straightforward to use a position sensor in the miniature AMB spindle system. Various position sensors for the application in AMB systems have been described by Boehm et al. [73]. He concluded that eddy current sensing principles are most suitable for AMB systems, mainly because of their high resolution, temperature stability, small phase delay and high dc-stability.

This Chapter describes the evaluation of different sensor types for miniature AMB spindles, mainly for the selection of the position sensors for the short rotor spindle described in Chapter 6. Different sensor types are experimentally tested on the miniature AMB spindle described in Chapter 3.

7.2 Specifications

The resolution of the position sensor puts an upper limit to the final achievable position accuracy of the system. For the miniature AMB spindle we have an error budget of 1.5 μm (1 σ) for the spindle position for micro milling. For micro EDM we have an error budget of 0.1 μm.

The bandwidth of the sensor determines up to which frequency an accurate position measurement can be done. One of the goals in the *μfac* project, is the estimation of cutting forces using the bearing signals. The cutting forces have typical frequencies of twice the rotational speed, in case of a two flute end mill. With a rotational speed of 150.000 rpm, the cutting force frequency is 5 KHz. To enable proper estimation of the cutting forces, a high quality sensor signal is required.

The phase delay, introduced by the sensor or the sensor electronics, contributes to the total phase delay in the plant. The phase delay in the sensor thus strongly influences the achievable bandwidth of the system. From commercially available sensors, the phase delay information is often not available, nor is information about the sensor electronics and the internal filtering in the sensor.

During spin up, the rotor will have two different rotational axis, the geometrical axis at zero rpm and the inertial rotational axis at supercritical speeds. During the transition between these two rotational axis, the rotor amplitude is heavily excited. The sensor has to allow for, and accurately measure these rotor displacements.

In a high speed rotor application, a minimal stand off between rotor and sensor tip is required to protect it in case of an emergency rotor touch down. A large amount of kinetic energy is stored in the AMB spindle at high rotational speeds. In case of an instability or other failure, the collision with the retainer bearings is very violent. To ensure the safety of the sensor tip, its stand off from the rotor has to larger than the gap between the rotor and the retainer bearing. This gap is 0.2 mm for the miniature spindle described in Chapter 3.

Due to the limited size of the short rotor setup as described in Chapter 6, the restrictions on size of the sensor tip are very severe. Chapter 6 elaborates on the importance of a reduced rotor length. Preferably, the sensor and the actuator are co-located, as described in Chapter 3.

The position sensors will have to observe a moving, in this case rotating, target. An overview of the sensor specifications is given in Table 7.1

Table 7.1: sensor Specifications.

Bandwidth	> 5	kHz
Resolution	< 0.1	μm
Target velocity	> 250	ms^{-1}
Stand off	> 0.1	mm
Range	> 0.2	mm

7.3 Sensor Types

This Section describes four measurement techniques commonly used for position sensing in AMBs. The goal of this section is to make a theoretical comparison between these sensor principles, and investigate their suitability in high speed AMB systems, and especially the short rotor design. Two of the sensor types have been selected for an experimental investigation.

7.3.1 Inductive Sensors

An inductive sensor generally consists of a coil with a ferrite core, carrying an AC current, working against a ferromagnetic target. The self-inductance, and thus the impedance of the coil depends on the distance between the sensor and the target. The oscillating frequency is chosen such, that eddy current effects in the target material can be neglected, which is usually below 100 kHz. To avoid eddy currents, an inductive measurement is preferably done on a non-conducting, or laminated target. Due to their low bandwidth, inductive sensors will not be suitable for application in the short rotor design.

7.3.2 Eddy Current Sensors

An eddy current sensor exists of two coils, usually air coils, of which one is excited by an AC current and the other is a reference. In the case of eddy current sensors, the oscillating frequency is high, up to 2 MHz. Eddy currents are induced in the electrically conductive target material. These eddy currents reduce the flux, and hence the self inductance of the coil, which is thus a measure for the target displacement. Ideally, eddy current sensors operate on a non-magnetic target, however versions are available that operate on ferro magnetic targets. The bandwidth of eddy current sensors is generally higher than that of inductive position sensors due to the much higher oscillating frequency. Eddy current sensors are used in many AMB spindles for example by Larsonneur [43] and Betschon [44].

Eddy current sensors are sensitive to target material inhomogeneities. When an eddy current sensor is used on a moving, or rotating ferromagnetic target, the sensor output is affected by slight changes in the material properties, introducing an error as function of the rotation.

The best sensor performance with eddy current sensors is achieved when measuring a non-ferromagnetic target. In case of a miniature spindle for speeds over 150.000 rpm, adding a non magnetic, for example aluminum, section to the shaft is however not feasible due to the high centrifugal stresses.

Due to the high oscillator frequency, and the low flux density levels, no interference with the magnetic flux from the active magnetic bearings is expected.

The eddy current sensors have been applied in the miniature AMB spindle for their small sensor tip, large stand off, relatively high resolution, and high bandwidth. The performance of the eddy current sensors on a fast moving target will be discussed in Section 7.4.

7.3.3 Optical Sensors

The rotor displacement can be measured in several ways using an optical sensing principle. In this section we consider two optical sensing principles, namely sensors where the amount of blocked light is a measure for the rotor displacement and optical reflective sensors.

In the spindle manufactured by EAAT, described in Chapter 2, the spindle position is measured by the amount of light that is blocked by the spindle. This measurement principle is known as the obscuration method, and is illustrated in Figure 7.1. The obscuration method is often used in laboratory demonstrators. This type of sensors is however not a commercially available building block for AMB systems, and has to be designed for each specific application.

An alternative optical sensor is the optical reflective sensor, where the intensity of the reflected light is a measure for the rotor position. The working principle of optical reflective sensors is illustrated in Figure 7.2. Optical reflective sensors are known to be sensitive to changes in target reflectivity. When a moving target is used, changes in reflectivity are visible in the sensor output. Furthermore, optical reflective sensors are sensitive to the influence of surrounding light.

Alternatively, reflectance compensated optical reflective sensors can be used. In the reflectance compensated sensors, two optical fiber bundles are used. A ratio metric calculation between the two responses is performed in order to calculate the

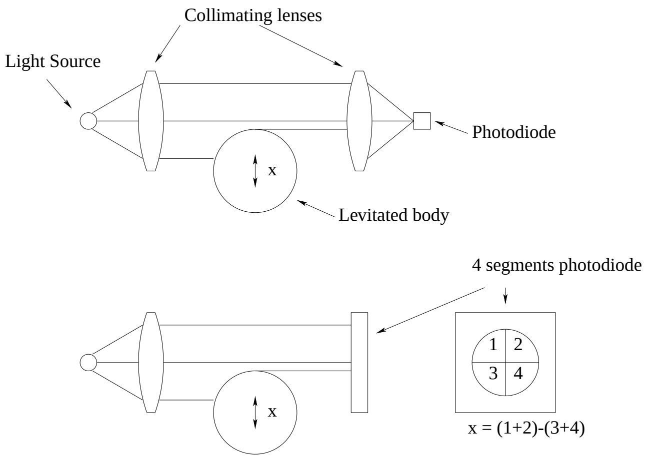

Figure 7.1: Obscuration Method, 4 segment diodes are used to measure multiple DOFs as well as velocities.

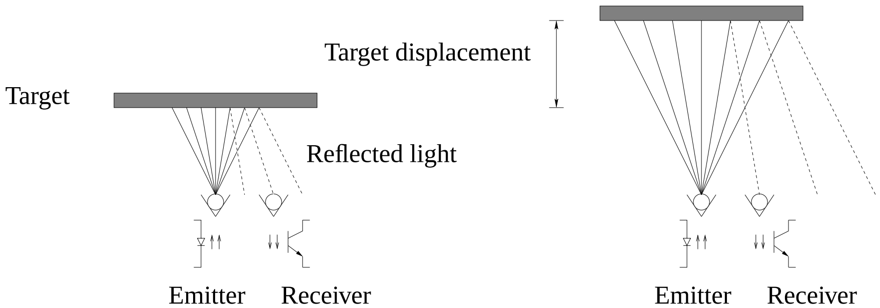

Figure 7.2: Measurement principle of the optical reflective sensor, where the intensity of the reflected light is a measure for the distance to the target.

target displacement. Figure 7.3 shows the typical responses of optical reflective sensors. Figure 7.3 shows how the non-compensated sensor can be used at the near side and at the far side. The highest sensitivity is obtained when using a reflectance non-compensated sensor on the near side. It also shows that this high sensitivity cannot be achieved with a reflectance compensated sensor.

Optical reflective sensors, reflectance compensated as well as reflectance dependent, are available with sensor tip sizes down to 0.8 mm. The small tip diameter is very well suited for the short rotor spindle setup described in Chapter 6.

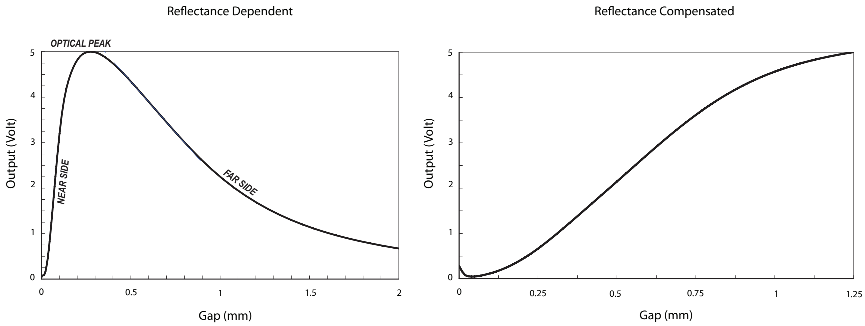

Figure 7.3: Typical response of an optical reflective sensor (left), showing the near side and far side of the response. The right illustration shows the response of a reflectance compensated optical reflective sensor. Illustration taken from Philtec [74].

7.3.4 Capacitive Sensors

A capacitor in its simplest form consists of two opposing conductive plates, separated by a dielectricum. The capacitance between these plates depends among others on the distance between the two plates and the surface area of the plates. In a capacitive sensor, the sensor head contains one plate of the capacitor, and the measured target is the other. The change in capacitance, and thus in distance, is measured by applying an AC voltage or current to the sensor and measuring the impedance.

Generally, a capacitive measurement requires grounding of the measured target. For this reason, not many applications for capacitive measurements in rotating magnetic bearing systems in literature are found. However, several technologies are currently developed to enable capacitive measurements on non-grounded targets. The application of capacitive sensing on a rotating AMB is described in [75]. One way to avoid target grounding is capacitive grounding, or the use of multiple capacitive probes on one target, operating 90 degrees out of phase.

The achievable resolution in capacitive sensors is very high compared to the alternative sensing principles discussed in this section. Sub nanometer resolutions are possible with capacitive sensing. The achievable resolution depends on the sensor tip size and the stand off to the rotor. For application in the short rotor design, the tip size is limited to a few millimeter. In order to still achieve sub micrometer resolution, the sensor stand off has to be in the order of several micrometers as well.

In the short rotor design, we aim to integrate the position sensors in the radial bearing stators. As mentioned, the capacitance depends on the surface area of the capacitor plates. The combination of the two requirements a small sensor tip size, and a stand off of 100-200 μm are contradicting. It is only possible to increase the sensor stand off with increasing plate size, maintaining resolution.

Capacitive sensors are however very well suited for moving targets, they are unaffected by the surface quality or material inhomogeneities of the target. Capacitive sensors are however considered not suitable for application in the short rotor setup due to the small sensor stand off when using a small sensor tip, and the requirement for grounding of the target.

Taking into account the considerations above, eddy current sensors have been used in the miniature AMB spindle, as described in Chapter 3. For the short rotor setup as described in Chapter 6, the size of the sensor tips has to be reduced even further. Optical reflective sensors are available with sensor tip sizes down to 0.8 mm. In the next section, the performance of eddy current sensors and optical reflective sensors is experimentally verified.

7.4 Experimental Results

The performance of optical reflective sensors and eddy current sensors in the high speed AMB spindle has experimentally been investigated. Firstly, the influence of the target surface quality has been investigated, as well as the improvement of the sensor performance by applying a target coating. Secondly, the orientation of the optical reflective sensor around its measurement axis has been investigated. Finally, the dynamic performance of the eddy current sensors and the optical reflective sensors are compared on a rotating target as well as on a non rotating target.

7.4.1 Rotor Surface Sensitivity

Optical reflective sensors are very sensitive for the reflectivity of the measured target. In this experiment, the sensor response to two different target surfaces is investigated. A polished target is observed, as well as a polished target equipped with a Diamond Like Carbon (DLC) coating. This coating has an optical finish and is applied to the rotor using vapour deposition. The DLC coating is applied to the spindle where the backup bearings are located to reduce the friction coefficient and for its high hardness.

The spindle has been polished for optimal reflective properties, the DLC coating has been applied on this polished surface. The experiment has been conducted on a commercially available drilling spindle, rotating at 400 Hz. The measurement has been performed with optical reflective sensors, with reflectance compensation.

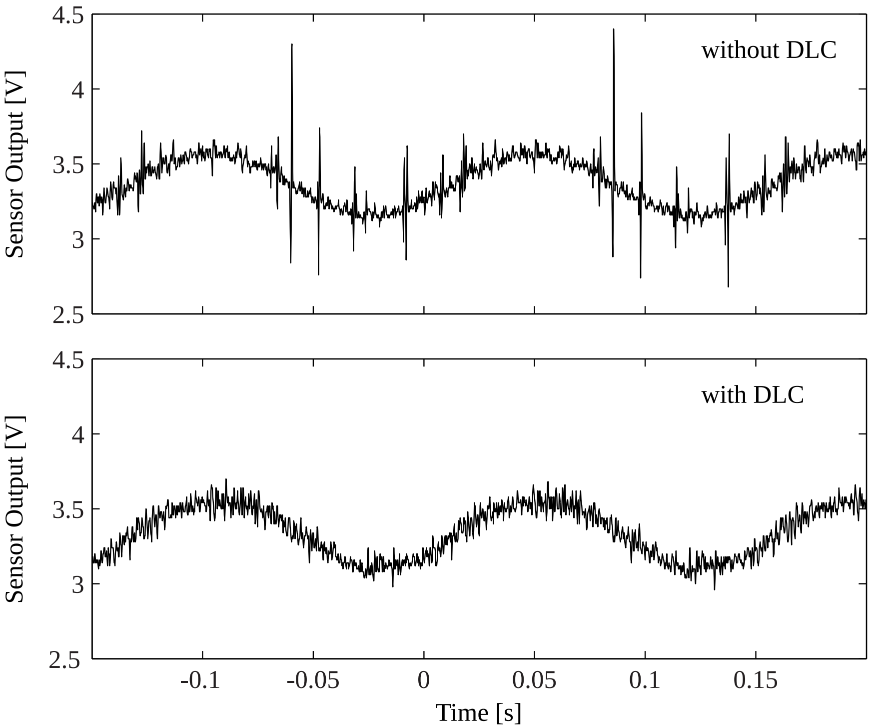

Figure 7.4: Runout measurement with an optical reflective sensor on a polished surface without Diamond Like Carbon coating, and on a polished surface with Diamond Like Carbon coating.

Figure 7.4 shows the measured runout for the polished surface as well as for the polished surface with DLC coating. The top graph in Figure 7.4 shows spikes on the measured runout in the measurement on a surface without DLC coating. The graph shows that the spikes are synchronous with the rotational angle. This leads to the conclusion that these spikes are caused by small imperfections on the rotor surface. The bottom graph in Figure 7.4 shows the runout measurement of the same rotor, with a DLC coating. By using a DLC coating on the rotor, the high spikes in the runout measurement are eliminated. Tiny scratches in the rotor surface have been filled by the vapor deposition of the DLC coating, and a regular surface is created. A noise band of about 0.2 V still remains, with some synchronous elements.

7.4.2 Optical Reflective Sensor Tip Orientation

This section describes the influence of the target surface quality as well as the influence of the fibre bundle alignment on the output of optical reflective sensors. The output of the sensor has been observed while measuring the distance to a target moving perpendicular to the measurement direction. The target moves in one direction, stops, and then moves back to its starting position. This experiment has been performed with a reflectance dependent optical reflective sensor, as well was with a reflectance compensated sensor. As described in the Section 7.3.3, the reflectance compensated optical reflective sensor tip contains two fiber bundles. These bundles are rectangular and oriented side by side.

Three measurements have been done. The first with a reflectance uncompensated optical reflective sensor. The second and third measurements have been done with reflectance compensated sensors. In the second experiment the two fiber bundles have been oriented perpendicular to the target moving direction, as prescribed by the sensor manufacturer. In the third measurement, the fiber bundles have been aligned with the target movement direction.

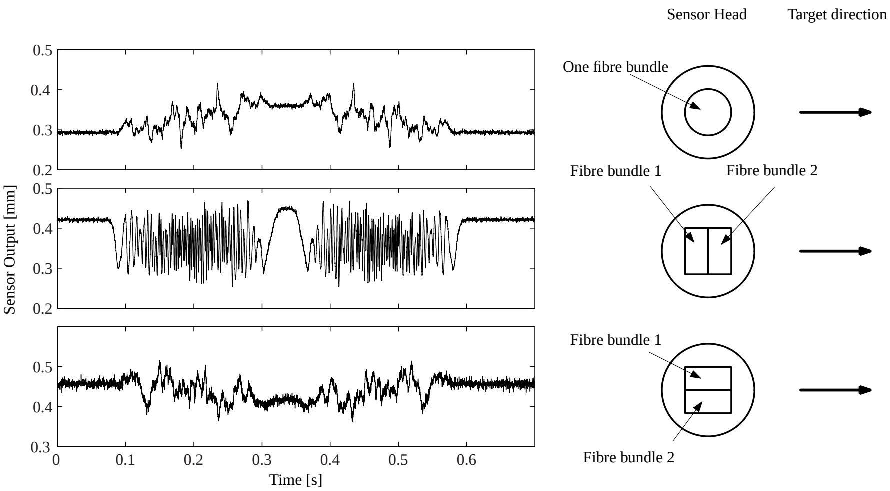

Figure 7.5: Optical reflective sensor responses of a target moving orthogonal to the measurement direction. From top to bottom, reflectance uncompensated sesor, reflectance compensated sensor with fiber alignment orthogonal to moving direction, reflectance compensated sensor with fiber alignment orthogonal to moving direction.

Figure 7.5 shows three responses of the optical reflective sensors. From top to bottom, the reflectance uncompensated sensor, the reflectance compensated sensor with the bundles aligned perpendicular to the target moving direction, and the reflectance compensated sensor with the bundles aligned parallel to the target moving direction.

The second plot in Figure 7.5 shows many peaks in the sensor response. This is caused by the fact that an irregularity on the target surface, for example a scratch is first only observed by one fiber bundle, deteriorating the ratio metric calculation for the reflectance compensation. We can however see that the reflectance compensation works well when the target is at standstill, the signal has the same level as at the starting position, contrary to the sensor without reflectance compensation in the first plot.

The third plot shows the response of the reflectance compensated sensor with the bundles aligned parallel to the target moving direction. This response shows less spikes, but the signal has a wider noise band than the second plot. The reflectance compensation is not efficient in this configuration, this can be concluded when comparing the signal level during the stop with the initial and final signal levels.

7.5 Sensor Dynamics

This section describes the comparison of the dynamics of the eddy current position sensors with optical reflective position sensors. The long rotor AMB system as described in Chapter 3 has been equipped both sensor types. The optical reflective sensors are of the reflectance compensated type.

The plant frequency response function has been measured with the eddy current sensors, as well as with the optical reflective sensors. The plant in this case consists of DA-converter, amplifier, actuator, position sensor, anti aliasing filter, and AD-converter. Only the position sensor is changed in this experiment. The frequency response is shown in the Bode plot in Figure 7.6. Figure 7.6 shows that there is a small gain difference between the two sensors, which is compensated for in the controller. As could be expected from the sensor specifications, the resolution of the optical reflective sensor is lower. This explains the higher noise level at the high frequencies in the bode plot.

Figure 7.6 shows that the optical reflective sensors introduce more phase lag into the system than the eddy current position sensors. An additional phase lag of 2 degrees is measured at 400 Hz. Since there is no delay to be expected in the optical path, this phase lag is presumably caused by the analog sensor electronics. This information is however not available from the manufacturer.

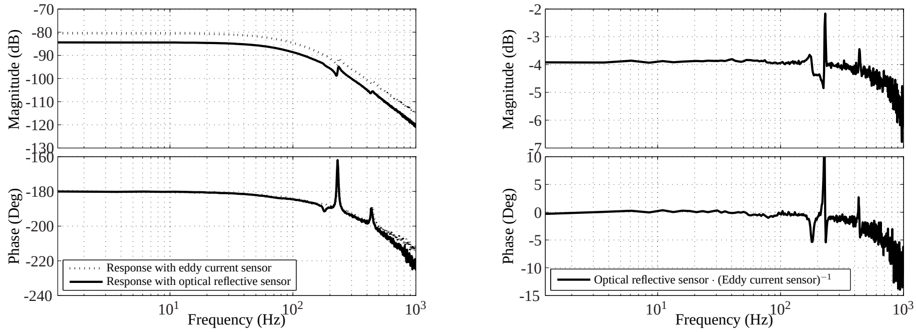

Figure 7.6: Plant freqency responses with eddy current sensor and with optical reflective sensor (left), and the frequency response of the Optical reflective sensor over the eddy current sensor (right).

7.5.1 Rotating Target

In this section, the eddy current sensors have been compared with the optical reflective sensors when measuring a rotating target. For this measurement an additional optical sensor has been added to the eddy current sensors in the long rotor setup as described in Chapter 3. The stabilizing, position control loop is closed with the eddy current sensors. The measurement principle is illustrated in Figure 7.7

The optical reflective sensor is oriented such, that the bundles are aligned perpendicular to the target moving direction, as shown in the middle plot in Figure 7.5. This introduces more noise into the signal, but improves the reflectance compensation.

In this experiment the spindle is excited at the rotational frequency by the mass unbalance and the magnetic unbalance in the motor. This excitation occurs in the measuring direction as well as in the orthogonal direction. Theoretically, the response to this excitation will increase until the rotational frequency equals the rigid modes where it is heavily excited, see Figure 3.22. Above this frequency, the spindle starts to rotate around its inertial axis and the response due to mass unbalance decreases and becomes constant.

This measurement has been performed at nine rotational speeds between 0 and 1700 Hz. The results of four measurements are shown in Figure 7.8.

The first plot in Figure 7.8 shows the output of the two sensors at a rotational speed of 98 Hz. The two sensor outputs are equal at zero rotational speed. There is a small phase difference between the two sensor signals, caused by a slight misalignment between the sensor axes. In this experiment we are interested in influence of the rotational speed on the sensor responses.

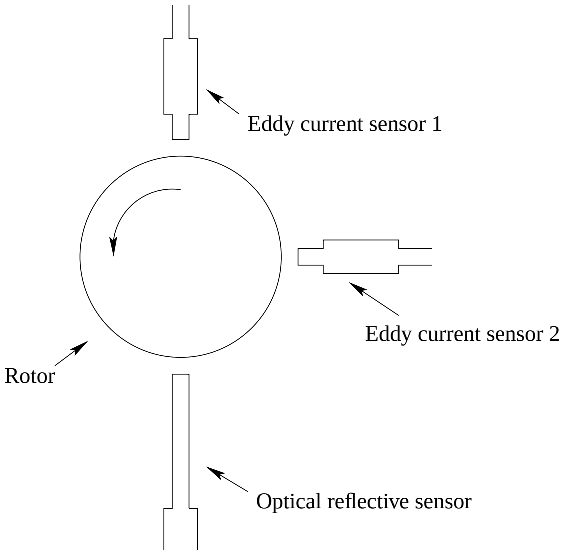

Figure 7.7: Illustration of the measurement setup for comparing the eddy current sensors with the optical reflective sensors. The control loop is closed with the eddy current sensors.

Figure 7.8 shows that with increasing rotational speed, the optical reflective sensor signal starts to lag the eddy current signal. Furthermore a gain difference is clearly visible. This is contrary to what can be expected from the frequency response function in Figure 7.6, as it shows a small difference in amplitude around 500 Hz and a phase lag between the two sensors of 2 degrees.

At 500 Hz, the spindle rotates around its inertial axis, Figure 7.8 shows little change in the signal magnitudes above this frequency, as expected.

For all rotational speeds, the FFT of each of the sensor signals is taken to compare of the amplitude and the phase information of both sensor signals. The amplitude difference between the two sensors increases up to 500 Hz, and then reaches a constant value. This is also visible in the time plots in Figure 7.8. The phase difference shows a similar behavior, it increases up to 500 Hz an then becomes constant. Thus the differences between the sensor responses arise when the spindle rotational axis changes from geometrical to inertial, and then remain constant.

From these observations it is assumed that the optical sensor is not only measuring the spindle displacement along the sensor axis, but also in the orthogonal direction. The light is reflected away from the sensor tip due to the roundness of the shaft, increasing the sensor output. Due to the unbalance excitation, the spindle describes a cylindrical motion in the bearings. The displacement in y direction thus

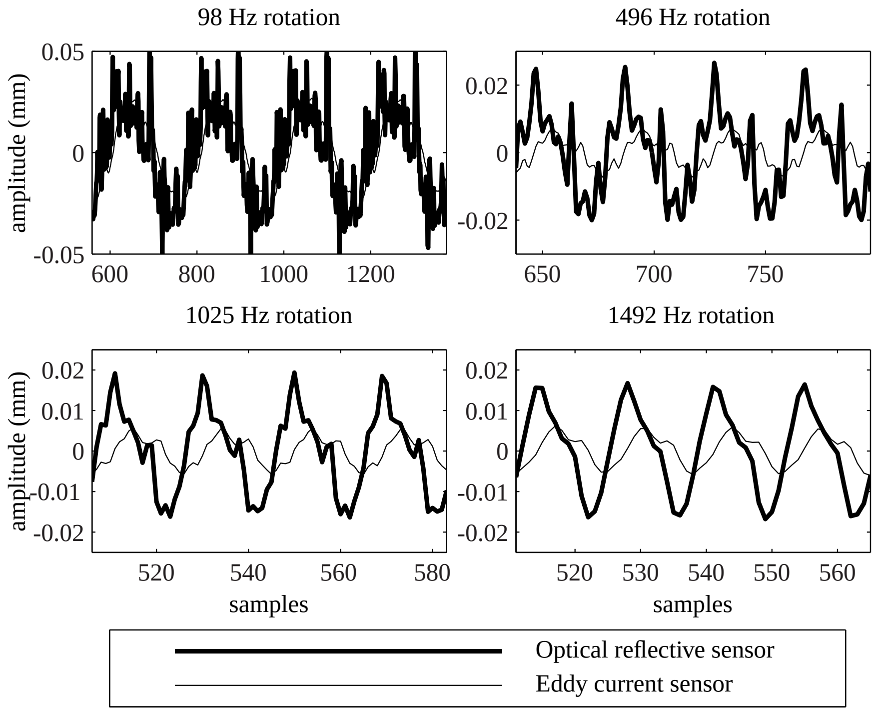

Figure 7.8: Runout measurements at 4 different rotational speeds, with eddy current position sensor as well as with optical reflective sensor.

lags the displacement in x direction with 90 degrees. This explains the phase lag in the optical sensor. This hypothesis has been verified by applying a sine in the y direction while observing the x direction with the optical reflective sensor. The result indeed showed a strong coupling between the two directions.

The diameter of the measured rotor is 12 mm. In the short rotor setup described in Chapter 6, the rotor diameter is reduced to 8 mm. The negative influence of the rotor roundness on the sensor performance will be larger.

7.6 Conclusions and Recommendations

This chapter aids in the position sensor choice for application in rotating AMB systems. Four contactless position sensor principles have theoretically been compared for the use in the short rotor functional model presented in Chapter 6. The compared sensors include inductive sensors, eddy-current sensors, optical reflective sensors, and capacitive sensors.

Two sensors have been selected for an experimental comparison in a rotating AMB application, the optical reflective sensors and the eddy current sensors. The optical reflective sensors are very sensitive to reflectivity changes on the rotor surface. This sensitivity can be reduced by the application of a Diamond Like Carbon (DLC) coating. Optical reflective sensors are available with reflectance compensation. However with the use of reflectance compensated sensors, resolution is lost. The orientation of the reflectance compensated sensors is influencing the sensor output, mounted in either orientation, they prove not to be suitable for moving targets.

A frequency response measurement shows that the optical reflective sensors introduce more phase lag into the system than the eddy current position sensors. The optical reflective position sensors are heavily influenced by the roundness of the target. The sensor output is strongly affected by a rotor displacement orthogonal to the measuring direction. The eddy current sensors perform well in the miniature spindle described in Chapter 3, however due to space limitations it cannot be used in the short rotor setup described in Chapter 6. Furthermore optical sensing principles can potentially achieve a higher sensing bandwidth.

Research into the use of an optical sensor, using the obscuration method which measures the amount of blocked light by the rotor is recommended. This measurement principle is not sensitive to the quality of the target surface, does not interfere with the magnetic bearings, allows for a large stand-off, and can be very fast. More research is required into the achievable sensor resolution. This type of sensors requires a specific design for the use in each application.

Chapter 8

Conclusions and Recommendations

The problem statement for this thesis was formulated as: Design, build and investigate Active Magnetic Bearings in a high speed micro milling center. The main achievement of this thesis work is the design and realization of a fully functional micro milling setup. This setup features a miniaturized Active Magnetic Bearing spindle, with a maximum rotational speed of 150.000 rpm.

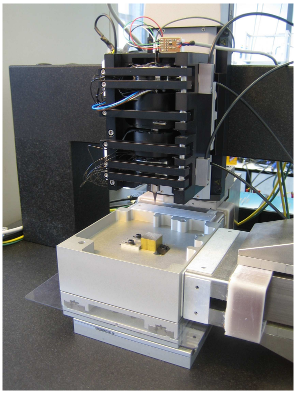

Figure 8.1: Micro milling setup with miniature AMB spindle.

A novel, patented, tool holder has been developed to connect the micro milling tool to the AMB spindle. The workpiece is positioned using a fast, Lorentz actuator driven xy-positioning stage. A fully functional model of a second, very compact AMB spindle is presented. The choice of position sensors for a magnetically levitated, compact, fast rotating spindle is not straightforward. Several position sensing principles have been compared, theoretically as well experimentally.

8.1 Conclusions

This section summarizes the conclusions from this research. First, we discuss the results from the design of the miniature AMB spindle. Next, the conclusions that can be drawn from the design of the novel toolholder and the integration of the spindle into the design of the micro milling setup are described. Finally, the conclusions from the investigation into the design of the functional model of a short rotor spindle and the sensor selection for fast rotating AMB spindles are summarized.

8.1.1 Miniature AMB Spindle

A miniature Active Magnetic Bearing (AMB) spindle has been designed and realized. A homo polar design of the reluctance actuators minimizes the rotating losses in the bearings. Permanent magnets provide the bias flux in the radial bearings. The analytical derivation of the bearing forces has been described, and used for the dimensioning of the actuators. The flux densities in the bearings have been verified using Finite Element Modeling (FEM). The analytical model proves to be an adequate tool in the design of the hybrid reluctance actuators.

The rotor dynamic modeling of the spindle has been described. This model, in combination with the analytical derivation of the bearing forces, has enabled the design of a stabilizing controller of the AMBs. The miniature AMB spindle has been realized.

An open loop bandwidth in the order of 200 Hz has been realized. The static error, without rotation, is below 30 nm (1 σ). The runout in the lower bearings, at 125.000 rpm has a maximum of 7.5 μm. This remaining runout is most likely caused by the unroundness of the spindle shaft. This would mean that it is not an actual rotor displacement, further research is needed to verify this assumption.

The frequency response functions from the model have been compared to the measured transfer functions. The model has proven to be adequate for the controller design for the AMB spindle. The design of a (Center of Gravity) COG decoupled control scheme has been described. The miniature AMB spindle is able to rotate with speeds up to 150.000 rpm. This is the maximum design speed of the spindle, and limited by the maximum outer diameter of the spindle.

Homo polar, hybrid reluctance actuators prove to be a suitable way of suspending a fast rotating spindle.

8.1.2 Novel Toolholder

We have designed and realized a novel tool holder to connect a micro milling tool to the spindle shaft. Commercially available tool holders are not suitable for miniature milling spindles due to their size, mass, introduced runout, and the loss of clamping force at high rotational speeds. A tool holder design has been presented in which the clamping force increases with increasing rotational speed. A FEM model has simulated the working principle of the toolholder.

Figure 8.2: Novel tool holder with micro mill. Photo courtesy of Philip Broos / Leiden, MicroMegazine.

The increase of clamping force has experimentally been verified by applying a static force simulating the centrifugal force. The clamping force increases with the applied forces as expected. The experiments have been reproducible, and the tool holder showed no signs of wear or plastic deformation. The toolholder has been tested at rotational speeds up to 80.000 rpm, and has been able to deal with the cutting conditions in a preliminary micro milling experiment.

8.1.3 Micro Milling Setup

A functional micro milling setup has been realized. The micro milling setup has enabled the testing of the miniature AMB spindle and the novel toolholder, under micro milling conditions. A fast xy-positioning stage for the workpiece has been build based on a wire bonding stage. The stage is controlled using PID controllers, realizing an open loop 0-dB crossing of 200 Hz. The xy-stage is able to achieve the acceleration and velocity required for micro milling at high rotational speeds.

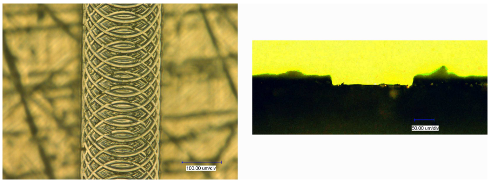

Figure 8.3: First milling result of the miniature machining center during milling in brass with a 0.2 mm end mill, at a rotational speed of 80.000 rpm.

A micro-milling experiment has been performed with the micro milling setup. Full slot milling has been done at 80.000 rpm with a 0.2 mm end mill in brass. This experiment has shown that the miniature AMB spindle is able to make a stable cut.

8.1.4 Functional Model of a Short Rotor Spindle

To perform micro milling with the macro milling equivalent cutting speed of 200 m·min^{-1} the rotational speed of micro milling spindles has to be increased even further. A higher rotational speed also requires an increase of flexural resonance frequencies to not excite them with the milling process. The increase of rotational speed requires a reduction of spindle diameter due to the increasing centrifugal stresses. To increase the flexural resonance frequencies, while maintaining a small spindle diameter, the spindle length has to be reduced. This results in a small, disk shaped rotor. The rotor dynamic behavior of a short rotor suspended with active magnetic bearings has been investigated.

Decentralized PID controllers, or COG decoupled PID controllers are not able to stabilize a disk shaped rotor at high rotational speeds. This is caused by the strong gyroscopic coupling in short rotors due to their large ratio between the polar moment of inertia (I_z) and the transverse moments of inertia (I_x and I_y).

A controller is required that compensates for the gyroscopic effects in a short rotor. The design of a cross feedback path for a COG decoupled PID controller is described. This cross feedback controller is successfully implemented in miniature AMB spindle. The cross-coupling between the two vertical planes has been reduced with 5 dB in the low frequency range. Limited by the low bandwidth of the tilt rate measurement, and by the already low gyroscopic coupling in the miniature AMB spindle.

A homopolar hybrid magnetic bearing concept to support a short disk shaped rotor in 5 DOF is presented, as well as the design of a fully functional model.

8.1.5 Sensor Selection for AMB spindles

Several position sensing principles for fast rotating spindles are compared, theoretically as well as experimentally. Capacitive, inductive, eddy current, and optical sensing principles are theoretically compared. Capacitive sensors are not suitable because of their need for target grounding and small stand off. Inductive sensors have a low bandwidth an require a non-magnetic target. Eddy currents sensors and optical reflective sensors are chosen for an experimental comparison. Frequency response function measurements of the plant have shown no difference in gain when the eddy current sensors are compared to the optical reflective sensors, and an additional phase lag of 2 degrees for the optical reflective sensors. However, optical reflective sensors are heavily influenced by the rotation of the shaft. A comparison of the time signals when measuring a rotating shaft have shown a strong influence of movement in the direction orthogonal to the measurement direction. This is caused by the roundness of the spindle shaft. The optical reflective sensors, reflectance compensated and without reflectance compensation, are both highly sensitive to reflectivity changes on the spindle shaft. A DLC coating reduces this sensitivity to scratches on the rotor surface.

8.2 Recommendations

This section describes the recommendations that can be done to improve the different aspects of the micro milling setup.

8.2.1 Miniature AMB Spindle

One of the main improvements that need to be made to the miniature AMB spindle is the remaining runout on the sensor signal. The source of this runout is most likely the unroundness of the spindle shaft. This hypothesis needs to be investigated. More research needs to be done into the position sensing of a fast rotating shaft. The currently used eddy current sensors are highly influenced by the rotation of the spindle shaft. The custom design of optical position sensors utilizing the obscuration method is recommended.

8.2.2 Novel Tool Holder

A measurement setup needs to be designed and built to measure the increase in clamping force in the proposed tool holder when rotating. This setup will have to be able run at high rotational speeds, and allow for mounting of the tool holder. Subsequently the holding torque needs to be measured at different rotational speeds to check whether the clamping force indeed increases with increasing rotational speed.

8.2.3 Micro Milling Setup

To use the miniature milling setup described in Chapter 5 for multi process machining, the encoder resolution needs to be increased. The finishing processes, μEDM and μECM require a higher positioning stability. With the current encoder, the aimed 0.1 μm workpiece accuracy can not be achieved. The μEDM and μECM processes are performed at low rotational speed, and require a very low spindle runout. It has to be evaluated whether a spindle drive which is able to drive the spindle up to 150.000 rpm is also suitable for very accurate rotation at low rotational speeds. High speed spindle drives have high flux densities in the airgaps for maximum power. This results in a high radial stiffness and are therefore sensitive to magnetic unbalance. Alternatively a similar miniature AMB spindle can be built using a spindle drive with a lower power density. The low runout improves the machining conditions for μEDM and μECM at low rotational speeds. Furthermore, for on the machine toolmaking, the setup needs to be equipped with a WEDG (Wire Electro Discharge Grinding) device.

8.2.4 Functional Model of a Short Rotor Spindle

To further increase the rotational speed, as well as the flexible spindle resonance frequencies, the short rotor functional model described in Chapter 6 has to be built. Further research is required to investigate whether the proposed gyroscopic compensation suffices with increased gyroscopic coupling in the short rotor system. An appropriate position sensor needs to be developed specifically for this spindle.

8.2.5 Sensor Selection for AMB spindles

The most promising technology for the position measurement of fast rotating shafts is the obscuration method. This type of sensors is potentially very fast, is not affected by rotation, is not influenced by the magnetic field of the AMB system, allows for a large stand off, and is fully contact less. This sensor needs however to be designed for each specific application. The use of a sensor which is able to measure the high frequency components is essential for the proper monitoring of the cutting process.

Bibliography

[1] G. Byrne, D. Dornfeld, B. Denkena, Advancing cutting technology, CIRP Annals - Manufacturing Technology 52 (2) (2003) 483 – 507.

[2] D. Dornfeld, S. Min, Y. Takeuchi, Recent advances in mechanical micromachining, CIRP Annals - Manufacturing Technology 55 (2) (2006) 745 – 768.

[3] J. Chae, S. S. Park, T. Freiheit, Investigation of micro-cutting operations, International Journal of Machine Tools & Manufature 46 (3,4) (2006) 313–332.

[4] X. Liu, R. E. DeVor, S. G. Kapoor, K. Ehmann, The mechanics of machining at the microscale: Assessment of the current state of the science, Journal of Manufacturing Science and Engineering 126 (2004) 666–678.

[5] P. Li, Micromilling of hardened tool steels, Ph.D. thesis, Delft University of Technology, Delft, The Netherlands (2009), ISBN 978-90-9024640-6.

[6] A. E. Honegger., G. Q. Langstaff, A. G. Phillip, T. D. VanRavenswaay, S. G. Kapoor, R. DeVor, Development of an automated microfactory: Part 1 - microfactory architecture and sub-systems development, Transactions of NAMRI/SME 34 (2006) 333–340.

[7] H. Weule, V. Hüntrup, H. Tritschler, Micro-cutting of steel to meet new requirements in miniaturization, CIRP Annals - Manufacturing Technology 50 (1) (2001) 61–64.

[8] T. Dow, E. Miller, K. Garrard, Tool force and deflection compensation for small milling tools, Precision Engineering 28 (2004) 31–45.

[9] M. Vogler, X. Liu, S. Kapoor, R. Devor, K. Ehmann, Development of meso-scale machine tool (mmt) systems, Transactions of NAMRI/SME (2002) 1–9.

[10] E. Kussul, T. Baidyk, L. Ruiz-Huerta, A. Caballero-Ruiz, G. Velasco and L. Kasatkina, Development of micromachine tool prototypes for microfactories, Journal of Micromechanics and Microengineering 12 (6) (2002) 795.

[11] H. Ishihara, F. Arai, T. Fukuda, Micro mechatronics and micro actuators, Mechatronics, IEEE/ASME Transactions on 1 (1) (1996) 68–79.

[12] R. Blom, M. Kimman, H. Langen, P. van den Hof, R. Munnig Schmidt, Effect of reduced dimensions of magnetic bearing spindles for micro-milling on actuation and sensing bandwidths, in: Proceedings of the euspen International Conference, Zurich, May 2008, Vol. 49, 2008, pp. 473 – 488.

[13] Y. Okazaki, N. Mishima, K. Ashida, Microfactory—concept, history, and developments, Journal of Manufacturing Science and Engineering 126 (4) (2004) 837–844.

[14] D. Axinte, S. A. Shukor, A. Bozdana, An analysis of the functional capability of an in-house developed miniature 4-axis machine tool, International Journal of Machine Tools and Manufacture In Press, Corrected Proof (2009) –.

[15] M. T. Okazaki, Y., N. Morita, Desk-top nc milling machine with 200 krpm spindle, in: Proc. 2001 ASPE Annual Meeting, 2001, pp. 192–195.

[16] A. E. Honegger., G. Q. Langstaff, A. G. Phillip, T. D. VanRavenswaay, S. G. Kapoor, R. DeVor, Development of an automated microfactory: Part 2 - experimentation and analysis, Transactions of NAMRI/SME 34 (2006) 341–348.

[17] I. Verettas, R. Clavel, A. Codourey, Microfactory: desktop cleanrooms for the production of microsystems, in: Assembly and Task Planning, 2003. Proceedings of the IEEE International Symposium on, 2003, pp. 18–23.

[18] Y. Okazaki, N. Mishima, K. Ashida, Microfactory—concept, history, and developments, Journal of Manufacturing Science and Engineering 126 (4) (2004) 837–844.

[19] Y. Takeuchi, Y. Sakaida, K. Sawada, T. Sata, Development of a 5-axis control ultraprecision milling machine for micromachining based on non-friction servomechanisms, CIRP Annals - Manufacturing Technology 49 (1) (2000) 295 – 298.

[20] P. Sriyotha, K. Nakamoto, M. Sugai, K. Yamazaki, Development of 5-axis linear motor driven super-precision machine, CIRP Annals - Manufacturing Technology 55 (1) (2006) 381 – 384.

[21] T. Masuzawa, State of the art of micromachining, CIRP Annals - Manufacturing Technology 49 (2) (2000) 473 – 488.

[22] J. Fleischer, J. Kotschenreuther, The manufacturing of micro molds by conventional and energy-assisted processes, The International Journal of Advanced Manufacturing Technology 33 (1) (2007) 75 – 85.

[23] A. Asad, T. Masaki, M. Rahman, H. Lim, Y. Wong, Tool-based micromachining, Journal of Materials Processing Technology 192-193 (2007) 204 – 211, the Seventh Asia Pacific Conference on Materials Processing (7th APCMP 2006).

[24] MIKROTOOLS PTE LTD, Integrated multi-process machine tool dt-110, `http://www.mikrotools.com`.

[25] T. Kurita, S. Watanabe, M. Hattori, Development of hybrid micro machine tool, Environmentally Conscious Design and Inverse Manufacturing, International Symposium on 0 (2001) 797.

[26] T. Moriwaki, E. Shamoto, Y. Song, S. Kohda, Development of a elliptical vibration milling machine, CIRP Annals - Manufacturing Technology 53 (1) (2004) 341 – 344.

[27] S. Y. Liang, R. L. Hecker, R. G. Landers, Machining process monitoring and control: The state-of-the-art, Journal of Manufacturing Science and Engineering 126 (2) (2004) 297–310.

[28] R. Blom, to be published, Ph.D. thesis, Delft University of Technology.

[29] MAKINO, Makino hyper2j, `http://www.makino.com`.

[30] KERN micro- und Feinwerktechnik GmbH & Co. KG, Kern micro, `http://www.kern-microtechnic.com`.

[31] Kugler GmbH, Kugler microgantry nano3/5x, `http://www.kugler-precision.com`.

[32] Atometric, Atometric g4-ultra, `http://www.atometric.com`.

[33] Microlution Inc., 363-s 3-axis cnc horizontal micro milling machine, `http://microlution-inc.com`.

[34] D. Huo, K. Cheng, F. Wardle, Design of a five-axis ultra-precision micro-milling machineŮultramill. part 1: holistic design approach, design considerations and specifications, The International Journal of Advanced Manufacturing Technology.

[35] L. Jabben, Mechatronic design of a magnetically suspended rotating platform, Ph.D. thesis, Delft University of Technology, Delft, The Netherlands (2007), ISBN 978-90-9022523-4.

[36] D. Laro, Mechatronic design of an electromagnetically levitated linear positioning system, Ph.D. thesis, Delft University of Technology, Delft, The Netherlands (2009), ISBN 978-90-9024255-2.

[37] G. Schweitzer, A. Traxler, H. Bleuler, Active Magnetic Bearings: Basics, Properties and Applications of Magnetic Bearings, Verlag der Fachvereine Hochschulverlag AG an der ETH Zurich, 1994.

[38] L. Molenaar, A novel planar magnetic bearing and motor configuration applied in a positioning stage, Ph.D. thesis, Delft University of Technology, Delft, The Netherlands (2000).

[39] A. Lee, F. Hsiao, D. Ko, Analysis and testing of magnetic bearing with permanent magnets for bias, JSME International Journal. 37 (4) (1997) 774–782.

[40] C. Zwyssig, S. Round, J. Kolar, Design and performance of a high speed milling spindle in digitally controller active magnetic bearings, in: Proceedings of the Second International Symposium on Magnetic Bearings, 1990, pp. 197–204.

[41] S. Auchet, P. Chevrier, M. Lacour, P. Lipinski, A new method of cutting force measurement based on command voltages of active electro-magnetic bearings, International Journal of Machine Tools and Manufacture 44 (14) (2004) 1441 – 1449.

[42] EAAT, 120.000 rpm Magnetic Bearing Spindle (2005).

[43] R. Larsonneur, Design and control of active magnetic bearing systems for high speed rotation, Ph.D. thesis, Swiss Federal Institute of Technology, Zürich, Switzerland (1990).

[44] F. Betschon, Design principles of integrated magnetic bearings, Ph.D. thesis, Swiss Federal Institute of Technology, Zürich, Switzerland (2000).

[45] S. Whitley, Review of the gas centrifuge until 1962. part II: Principles of high-speed rotation, Reviews of Modern Physics, Vol 56, No 1. (1984) 67–97.

[46] P. Campbell, Magnetic circuit design, definition of the load line, `www.magnetweb.com`.

[47] W.-L. Lee, Aufbau un regelung homopolarer magnetlagersysteme, Ph.D. thesis, Technical University of Braunschweig, Baunschweig, Germany (2002), ISBN 3-18-395108-8.

[48] F. Matsumura, T. Yoshimoto, System modeling and control design of a horizontal-shaft magnetic-bearing system, IEEE Transactions on Magnetics. MAG-22 (3) (1986) 196–203.

[49] H. Balini, H. Köroğlu, C. Scherer, Lpv control for synchronous disturbance attenuation in active magnetic bearings, in: Proc. Dynamic Systems and Control Conference (DSCC),Ann Arbor, Michigan, 2008.

[50] S. Dietz, H. Balini, C. Scherer, Robust control against disturbance model uncertainty in active magnetic bearings, in: Proc. 11th International Symposium on Magnetic Bearings, Nara, Japan, 2008.

[51] E. Wernholt, S. Gunnarsson, Analysis of methods for multivariable frequency response function estimation in closed loop, in: Proc. 46th IEEE Conference on Decision and Control, New Orleans, Louisiana, 2007.

[52] T. Dever, G. Brown, K. Duffy, R. Jansen, Modeling and development of a magnetic bearing controller for a high speed flywheel system, Tech. rep., NASA, Cleveland, Ohio 44135-3191 (2005).

[53] DORMER, General hints on tool holders, www.dormer.com.

[54] E. I. Rivin, J. Agapiou, C. Brecher, M. Clewett, R. Erickson, F. Huston, Y. Kadowaki, E. Lenz, T. Moriwaki, A. Pitsker, S. Shimizu, T. Schulte, M. Schulz, K. Smith, M. Tsutsumi, A. Ulsoy, M. Weck, K. Yokoyama, Tooling structure: Interface between cutting edge and machine tool, CIRP Annals - Manufacturing Technology 49 (2) (2000) 591 – 634.

[55] Schunk, Tribos polygonal clamping, www.schunk.com.

[56] F. Haimer, Tool holder for a tool, especially a boring, milling or rubbing tool which can be rotated about a rotational axis, US Patent 7217072 (2007).

[57] M. C. Tempest, High speed drill holders, US Patent 2001/0050466 (2001).

[58] C. Zwyssig, S. Round, J. Kolar, Analytical and experimental investigation of a low torque, ultra-high speed drive system, in: Industry Applications Conference, 2006. 41st IAS Annual Meeting. Conference Record of the 2006 IEEE, Vol. 3, 2006, pp. 1507–1513.

[59] A. Aramcharoen, P. Mativenga, Size effect and tool geometry in micromilling of tool steel, Precision Engineering 33 (4) (2009) 402 – 407.

[60] M. B. G. Jun, X. Liu, R. E. DeVor, S. G. Kapoor, Investigation of the dynamics of microend milling—part i: Model development, Journal of Manufacturing Science and Engineering 128 (4) (2006) 893–900.

[61] J. Wesselingh, to be published, Ph.D. thesis, Delft University of Technology.

[62] G. Genta, Dynamics of Rotating Systems (Mechanical Engineering Series), Springer, 2005.

[63] H. Fujiwara, O. M. H. Okubo, Stability evaluation of high frequency eigenmodes for active magnetic bearing rotors, Proc. of the Seventh International Symposium on Magnetic Bearings (2000) 83–88.

[64] H. Shida, M. Ichihara, K. Seto, Motion and vibration control of flexible rotor using magnetic bearings, Proc. of the Eighth International Symposium on Magnetic Bearings (2002) 381–386.

[65] Y. Nakajima, T. Sagane, M. Saigou, M. Ichihara, H. Tajima, K. Seto, A new modeling technique and control system design of flexible rotor using magnetic bearings for motion and vibration control, Proc. of the Ninth International Symposium on Magnetic Bearings (2004) 52.

[66] T. Takami, M. Kawanishi, H. Kanki, Advanced control for active magnetic bearing - robust control for flexible rotor magnetic bearing considering spillover and gyroscopic effects, Proc. of the Eighth International Symposium on Magnetic Bearings (2002) 439–444.

[67] M. Ahrens, L. Kucera, R. Larsonneur, Performance of a magnetically suspended flywheel energy storage device, IEEE Transactions on Control Systems Technology. 4 (5) (1996) 494–502.

[68] Y. Okada, B. Nagai, T. Shimane, Cross-feedback stabilization of the digitally controlled magnetic bearing, Journal of Vibration and Acoustics 114 (1) (1992) 54–59.

[69] J. Park, A. Palazzolo, R. Beach, Mimo active vibration control of magnetically suspended flywheels for satellite ipac service, Journal of Dynamic Systems, Measurement, and Control 130 (4) (2008) 041005.

[70] T. Masuzawa, J. Kojima, H. Onuma, Y. Okada, Micro magnetic bearing for an artificial heart, Proc. of the Ninth International Symposium on Magnetic Bearings.

[71] A. Borisavljevic, to be published, Ph.D. thesis, Delft University of Technology.

[72] P. Tsigkourakos, Design of a miniature high speed spindle test setup including power electronic converter (2008).

[73] J. Boehm, R. Gerber, N. Kiley, Sensors for magnetic bearings, Magnetics, IEEE Transactions on 29 (6) (1993) 2962–2964.

[74] PHILTEC, Inc. Annapolis, Maryland U.S.A. , Product data sheet, `http://www.philtec.com`.

[75] P. Overschie, to be published, Ph.D. thesis, Delft University of Technology.

Abstract

Design of a Micro Milling Setup with an Active Magnetic Bearing Spindle

Maarten Kimman

Micro milling is the mechanical removal of material using cutting tools with a sub-millimeter diameter. Present day, these tools are widely used in milling spindles designed for machining with conventional tools. The fabrication technology industry demands improvements in accuracy and throughput of the micro milling process. These improvements are expected to be made by designing tools especially for micro machining processes. The use of active magnetic bearing (AMB) technology in these milling tools aids in the increase of accuracy and throughput. In an AMB, a spindle shaft is actively suspended using electromagnetic forces and a feedback loop. Due to the active nature, position and current information from the bearings can be used to monitor the process conditions. The spindle shaft is suspended entirely contactless. Therefore, the rotational speed in an AMB is not limited by mechanical friction, and the accuracy is no longer determined by the manufacturing tolerances of the spindle parts.

To achieve a very high shape accuracy in combination with a high surface quality, the micro milling process needs to be combined with other machining processes such as micro electronic discharge machining, and micro electrochemical machining. The AMBs can in these processes be used for arbitrary movements of the rotational axis and vibration-assisted machining. A micro machining setup is envisioned which combines these processes, and which allows for on-machine toolmaking to eliminate run-out effects in the final machining steps.

The goal of this research was to investigate the use of AMBs in a micro milling

setup. A miniature milling spindle has been designed and realized. The mechatronic design approach aimed at active reduction of the low frequent disturbances due to the work piece accelerations. The high frequent cutting force disturbances do not result in tooltip position errors due to the rotor inertia. The rotor has been designed so, that its flexible resonance frequencies lie well above the target operating speed of the spindle, which is 150.000 rpm (2.5 kHz). When small diameter tools are used, high rotational speeds are required to maintain productivity.

The spindle shaft is supported by two radial bearings and one axial bearing. The radial bearings are permanent magnet-biased electromagnetic actuators. A homopolar bearing configuration should be applied in high speed AMB systems to minimize the rotating losses. Only stator legs with equal polarity are facing the rotor along the circumference, reducing changing magnetic fields in the rotor. A position feedback loop is used in which the displacement of the rotor in the bearings is measured using eddy-current sensors. The position sensors have been integrated in the radial actuators, resulting in a co-located sensor actuator configuration. The rotor is equipped with a disk, reluctance actuators on each side of this disk position the rotor in axial direction. The miniature AMB spindle has achieved a maximum rotational speed of 150.000 rpm, limited by the strength of the rotor material.

The limited size of the miniature AMB spindle, and its high rotational speed required the design of a novel tool holder. The tool holder forms the connection between the fast rotating spindle shaft and the micro cutting tool. In conventional toolholders, the clamping force is reduced by the centrifugal forces at high rotational speeds. A small monolithic structure has been designed and manufactured which utilizes the high centrifugal loads to increase the clamping force on the tool and the spindle.

A micro milling setup has been designed and build including the AMB spindle and an xy-stage used in a wire bonding machine (NXP ITEC). A series of stable cuts using the miniature AMB spindle has been performed in brass using a 0.2 mm micro milling tool at a rotational speed of 80.000 rpm. Therewith, the possibility of using small sized tools in combination with magnetic bearings for micro milling has been shown. However, more research is needed to find the optimal machining conditions.

A novel spindle setup design has been presented in order to increase the spindle rotational speeds as well as the flexible spindle resonance frequencies. Because the outside diameter is limited by the high rotational speed, this results in a very short, disk-shaped rotor. By decreasing the spindle length, the ratio between the spindle's inertia around the z-axis and the inertia around the xy-axes strongly increases. This increase results in a large gyroscopic coupling in the spindle at high rotational speeds. By designing a very short rotor, not only the flexible modes are shifted to higher frequencies, but also one rigid mode is avoided during spin up. The large gyroscopic coupling, however, causes instability when the spindle position is controlled using SISO (Single Input Single Output) controllers, either decentralized, or statically decoupled. An additional feedback loop has been designed to compensate for this increased gyroscopic coupling. In this feedback loop, the tilt rate in one vertical plane is compensated by applying a torque in the other vertical plane using a rotational speed dependent gain. This controller is referred to as a cross-feedback controller, and has been implemented in the realized milling setup to investigate its performance. The results show a reduction of the coupling between the two controller planes.

The performance of the realized miniature AMB spindle is limited by the quality of the position measurement. The eddy-current sensors are sensitive to the unroundness of the spindle shaft. The functional model requires an unconventional position measurement due to its limited dimensions. Several techniques for the position measurement of a fast rotating shaft have been compared. The small size of the spindle requires a sensor with a small sensing surface. Therefore, the averaging over the probe area is very limited, resulting in a high sensitivity for irregularities on the rotor surface. Several sensing techniques have theoretically been compared. Eddy-current and optical reflective sensors have been investigated experimentally. Optical reflective sensors seem very applicable due to their small probe diameter (0.8 mm). The optical reflective sensors appear to be very sensitive for displacement orthogonal to the measurement direction, and for irregularities on the rotor surface. From this investigation, it is concluded that the best method for measuring the displacement of a fast rotating shaft is by the determination of the amount of light blocked by the rotor. This contactless measurement method is insensitive to: the quality of the rotor surface, displacements orthogonal to the measurement direction, target speed, magnetic targets, and rotor material. However, the geometry of such a sensor is application specific, and therefore needs to be designed and built for our application.

The realized micro milling setup with the miniature AMB milling spindle has shown that AMBs can be used in combination with a relatively small rotor to perform micro milling in a stable manner. Furture work needs to be done on finding the optimal process parameters, and improving of the position measurement of the rotor.

Samenvatting

Ontwerp van een Opstelling voor Microfrezen met een Magnetisch Gelagerd Spindel.

Maarten Kimman

Frezen is het verspanend bewerken van materialen. Microfrezen is het frezen met een freesdiameter kleiner dan 1 mm. Momenteel worden de microfrezen gebruikt in machines die ontworpen zijn voor conventioneel frezen. De fabricageindustrie heeft behoefte aan een verbetering van het micro-freesproces met het oog op productiviteit en nauwkeurigheid. De verwachting is dat deze verbeteringen kunnen worden gemaakt door het ontwerp van machines speciaal gericht op het micro-freesproces. Het gebruik van actieve magneetlagering kan bijdragen aan het verhogen van de nauwkeurigheid en de productiviteit. In een actief magneetlager wordt de as actief gepositioneerd door middel van elektromagnetische krachten en een regellus. Door gebruik te maken van de informatie over de prositie van de as en de benodigde stromen, kunnen de condities van het frees proces geobserveerd worden. De as wordt volledig contactloos gepositioneerd, hierdoor is de omwentelingssnelheid niet langer gelimiteerd door mechanische wrijving in de lagers, en is de nauwkeurigheid niet langer afhankelijk van de fabricagetoleranties in de lagers.

Om uiteindelijk zeer hoge nauwkeurigheden de bereiken met een hoge kwaliteit van het oppervlak, zal het microfreesproces gecombineerd moeten worden met andere processen zoals micro-vonkverspanen en micro-elektrochemische bewerkingen. Bij laatstgenoemde processen kan de magnetische lagering gebruikt worden om het roterende gereedschap een willekeurige baan te laten beschrijven, of om vibraties te introduceren in het proces. Uiteindelijk is het doel een opstelling te realiseren waarin deze processen worden gecombineerd en waarin gereedschappen voor

de nabewerkingsstappen worden gemaakt in de machine zelf om run-out effecten de minimaliseren.

Het doel van dit onderzoek was het onderzoeken van de toepasbaarheid van magnetische lagering in een micro-freesopstelling. Hiertoe is een miniatuurspindel ontworpen en gerealiseerd met een actieve magnetische lagering. Bij het mechatronisch ontwerp is gestreefd naar een actieve onderdrukking van stoorkrachten door de beweging van het werkstuk. De hoogfrequente stoorkrachten uit het freesproces resulteren niet in positiefouten door de massatraagheid van de rotor. De rotor is zodanig ontworpen dat de structurele resonantiefrequenties ruim boven de maximum omloop snelheid van 150.000 toeren per minuut, ofwel 2.5 kHz, liggen. Deze hoge snelheden zijn noodzakelijk om productief te blijven wanneer gereedschappen met zeer kleine diameter worden gebruikt.

De rotor wordt gepositioneerd door twee radiaallagers en een axiaallager. De radiaallagers zijn reluctantie actuatoren, voorgespannen met behulp van permanente magneten. Om de verliezen in hoogtoerige magnetische lagers te beperken, dient een homopolaire configuratie gebruikt te worden. Bij een dergelijke configuratie zijn alleen polen met dezelfde polariteit naar de rotor gericht om wisselende magnetische velden in de rotor te vermijden. De regellus maakt gebruik van positieterugkoppeling, de verplaatsing van de rotor in de lagers wordt gemeten met behulp van eddy-current sensoren. Deze sensoren zijn geïntegreerd in de radiaallagers, waardoor een geco-loceerde sensor-actuatorconfiguratie ontstaat. De rotor is voorzien van een schijf, reluctantie-actuatoren aan weerszijden van deze schijf positioneren de rotor in axiale richting. Het spindel heeft een maximale omloopsnelheid van 150.000 toeren per minuut behaald. Deze snelheid is beperkt door de sterkte van het rotormateriaal.

De beperkte afmetingen van het spindel, en de hoge omloopsnelheden, vereisten het ontwerp van een nieuw type gereedschapshouder. De gereedschapshouder vormt de verbinding tussen de sneldraaiende rotor en de microfrees. In conventionele gereedschapshouders wordt de klemkracht gereduceerd door de centrifugale krachten die optreden bij hoge toerentallen. Een kleine, monolithische structuur is ontworpen en gerealiseerd waarbij de klemkracht op de frees en de rotor juist toenemen ten gevolge van de centrifugale belasting.

Het spindel is geïntegreerd in een daarvoor ontworpen micro-freesopstelling. Het werkstuk wordt in deze opstelling gepositioneerd met een xy-tafel aangedreven door Lorentz-actuatoren. De xy-lagering en de Lorentz-actuatoren zijn afkomstig uit wire bonding machine van NXP ITEC. Met deze opstelling zijn de eerste banen gefreesd met een frees met een diameter van 0.2 mm en een omwentelingssnelheid van 80.000 toeren per minuut. Hiermee is aangetoond dat het mogelijk is om stabiel te microfrezen met een klein actief magnetisch gelagerd spindel. Meer onderzoek is echter nodig om de optimale bewerkingscondities te vinden.

Het ontwerp van een nieuw spindelconcept is gepresenteerd om zowel de omwentelingssnelheden verder te verhogen als de structurele resonantiefrequenties. Omdat de buitendiameter beperkt wordt door de hoge omwentelingssnelheid, resulteert dit in een korte schijfvormige rotor. Door deze rotorvorm, is de verhouding tussen het traagheidsmoment om de z-as en de traagheidsmomenten om de xy assen sterk verhoogd. Deze hoge verhouding van de traagheidsmomenten resulteert in een sterke gyroscopische koppeling op hoge toerentallen. Door het gebruik van een korte schijfvormige rotor worden niet alleen de structurele resonantiefrequenties verhoogd, een rigide mode wordt ook vermeden tijdens het opvoeren van de omwentelingssnelheid. Echter, de sterke gyroscopische koppeling kan ook voor instabiliteit zorgen wanneer hiermee geen rekening wordt gehouden in de regelaar, zoals bij het gebruik van SISO (Single Input Single Output) controllers, al dan niet ontkoppeld naar het zwaartepunt. Een extra regellus is geïntroduceerd die de gyroscopische koppeling compenseert. In deze regellus wordt een kanteling in het verticale vlak van de rotor gecompenseerd met een koppel in het vlak daar loodrecht op, afhankelijk van een snelheidsafhankelijke versterking. Deze regellus wordt wel een kruisterugkoppeling genoemd, en is geïmplementeerd en getest in de gerealiseerde freesopstelling. De reductie van de gyroscopische koppeling is hierbij gemeten.

De prestaties van het gerealiseerde freesspindel worden gelimiteerd door de kwaliteit van de positiemeting van de sneldraaiende rotor, de eddy-current sensoren blijken erg gevoelig voor de onrondheid van de rotor. Het gepresenteerde ontwerp van een spindel met een schijfvormige rotor vereist een onconventionele positiemeting vanwege de geringe afmetingen. Verschillende meetmethoden zijn onderzocht voor het meten van de verplaatsing van een sneldraaiende as. Vanwege geringe spindeldimensies zijn sensoren met een klein sensoroppervlak noodzakelijk. Hierdoor vindt echter weinig middeling plaats over het sensoroppervlak, resulterend in een hoge gevoeligheid voor onregelmatigheden in het oppervlak. Verscheidende meetmethoden zijn theoretisch onderzocht. Eddy-current sensoren zijn experimenteel vergeleken met optisch-reflectieve sensoren, die vanwege hun geringe sensorafmetingen (0.8 mm) zeer geschikt lijken. Echter, de optisch-reflectieve sensoren blijken erg gevoelig voor verplaatsingen van de rotor loodrecht op de meetrichting en voor onregelmatigheden in het rotoroppervlak. De meest geschikte methode voor het meten van de verplaatsing van een sneldraaiende as is een bepaling van de hoeveelheid geblokkeerd licht. Deze contactloze meetmethode is ongevoelig voor: de kwaliteit van het rotoroppervlak, verplaatsingen loodrecht op de meetrichting, de snelheid van het oppervlak, magnetische invloeden, en materiaaleigenschappen. De geometrie van een dergelijke sensor is afhankelijk van de toepassing, en zal daarom specifiek voor deze toepassing ontwikkeld moeten worden.

Met de gerealiseerde microfreesopstelling is aangetoond dat het mogelijk is te frezen met een klein magnetisch gelagerd spindel. Echter er dient verder onderzoek gedaan te worden naar het vinden van de optimale procesparameters en naar het verbeteren van de positiemeting van de sneldraaiende rotor.

Acknowledgments

First of all, I would like to thank my promotor, prof. Munnig Schmidt. Rob, thank you for our interesting discussions, and for giving them a personal touch. I also would like to thank my co-promotor, dr. Langen. Hans, thank you for initiating a project of this impressive size and involving me in it. I really thank you for the support, and I appreciate the freedom you have given me in this project. I would like to thank prof. van Eijk, prof. Steinbuch, prof. Rixen, and prof. Schitter for their help to improve the quality of the thesis.

I have enjoyed working in the Mechatronic System Design group, Chris, Dipali, Hussein, Ki-Nam, Leon, Mark, Michiel, Peter, Rudolf, Warner, it has been a pleasure to work with you. I especially would like to thank Jasper, Jeroen, and Sander for time they took to help with specific technical issues. Dick, thank you for sharing your knowledge on magnetic bearings, and for proof reading the thesis. Jon, thank you for proof reading the journal paper and parts of the thesis. Thank you Jo for the ever interesting discussions. Jan-Willem, thank you for your work on the cross-feedback controller as part of your MSc introduction project. I thank my colleagues in the Micro Factory project, Navin, Eric, Peiyuan, and Frans. Guido, it was nice to be your room mate, I really enjoyed our discussions, whether work related or not. Rogier, I have enjoyed working with you on the frf measurements. Aleksandar, Henk, and Petros, it has been a pleasure to work with you on the short rotor setup.

I would like to thank NXP ITEC, and especially Thomas Porck, for the donation of the xy-table and the voice coil actuators. Robin, thank you for your work on the xy-stage. Jan Los, thank you for your experimental work on the toolholder. I would like to thank the PME support staff, Jos, Harry, and Patrick for all their help. I owe my gratitude to the people from the mechanical workshop, John, Ad, Hans, and Jan van Frankenhuyzen. Mark and Ferdinand, thank you for your help on shipping the entire setup to Spain for the Euspen conference.

Finally I would like to thank my family for their unconditional support. EEv, thank you for your love, help, and understanding, the great things to come have been the best motivation I can think of.

Curriculum Vitae

Maarten Kimman was born on the 28th of April 1980, in Leeuwarden, The Netherlands. He received his MSc degree in 2005 in Mechanical Engineering at the Delft University of Technology with a specialization in Advanced Mechatronics. The topic of his graduation work was a study into high speed rotation using Active Magnetic Bearings (AMBs). In August 2005 he started his PhD on the design of a micro milling setup with AMB technology. This research has resulted in a patent application, a journal publication, and publications in several conference proceedings. From November 2009 to April 2010 he has been working on a joint research project of the Delft University of Technology and ASML in Veldhoven on high efficiency reluctance actuators. Since march 2010 he is working at ASML in Veldhoven as a mechatronic design engineer in the field of electromagnetic drives.

Publications

M.H. Kimman, H.H. Langen, and R.H. Munnig Schmidt, "A Miniature Milling Spindle With Active Magnetic Bearings", Mechatronics, Volume 20, Issue 2, March 2010, Pages 224-235.

M.H. Kimman, J.P. van Schieveen, Micro Turbine Technology B.V., "Rotary Connector for a Rotating Shank or Axle", International Patent Application, Publication number: WO/2010/047594.

M.H. Kimman, H.H. Langen, R.H. Munnig Schmidt, The Design of a High Speed Milling Spindle Using Active Magnetic Bearings; Rotor Shape Optimization, in Proc. of the Euspen conference, 2009, San Sebastian, Spain.

A. Borisavljevic, M.H. Kimman, P. Tsigkourakos, H.H. Langen, H. Polinder and J.A. Ferreira, Integration of a Motor Drive within Active Magnetic Bearings for High-Speed Micro-Milling, in Proc. of the Euspen conference, 2009, San Sebastian, Spain.

Hans Langen, Maarten Kimman, Rogier Blom, Peiyuan Li, Eric Buice and Rob Munnig Schmidt ,"Towards Micro (hard)milling using Miniature Active Magnetic

Bearings", in Proc. of the sixth International Workshop on Microfactories, 2008, Evanston, USA.
M.H. Kimman, H.H. Langen, A. Borisavljevic, H. Polinder, R.H. Munnig Schmidt, "Design and Realization of a Miniature Milling Spindle with Active Magnetic Bearings", in Proc. of the eleventh International Symposium on Magnetic Bearings, 2008, Nara, Japan.
A. Borisavljevic, H. Polinder, M. Kimman, H. Langen, J.A. Ferreira, "Very high speed motor design for magnetically levitated spindles", in Proc. of the Power Conversion Intelligent Motion conference, 2008, Nuremberg, Germany.
R.S. Blom, M.H. Kimman, H.H. Langen, P.M.J. van den Hof, R.H. Munnig Schmidt, "Effect of miniaturization of Magnetic Bearing Spindles for micro-milling on actuation and sensing bandwidths", in Proc. of the Euspen conference, 2008, Zürich, Switzerland.
M.H. Kimman, H.H. Langen, J. van Eijk and R.H. Munnig Schmidt, "Design and Realization of a Miniature Spindle Test Setup with Active Magnetic Bearings", in Proc. of the IEEE/ASME conf. on Advanced Intelligent Mechatronics, 2007, Zürich, Switzerland.
M. Kimman, H. Langen, and J. van Eijk, "Design of a novel miniature spindle concept with active magnetic bearings using the gyroscopic stiffening effect", in Proc. of the tenth International Symposium on Magnetic Bearings, 2006, Martigny, Switzerland.